A review of experiments on stationary bluff body wakes

Forouzi Feshalami, Behzad; He, Shuisheng; Scarano, Fulvio; Gan, Lian; Morton, Chris

DOI
10.1063/5.0077323

Publication date
2022

Document Version
Final published version

Published in
Physics of Fluids

Physics of Fluids

A review of experiments on stationary bluff body wakes

Cite as: Phys. Fluids **34**, 011301 (2022); https://doi.org/10.1063/5.0077323
Submitted: 01 November 2021 • Accepted: 22 December 2021 • Published Online: 12 January 2022

Behzad Forouzi Feshalami, Shuisheng He, Fulvio Scarano, et al.

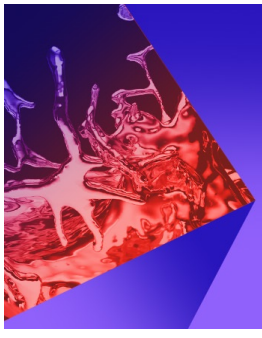

Physics of Fluids REVIEW scitation.org/journal/phf

A review of experiments on stationary bluff body wakes

Cite as: Phys. Fluids **34**, 011301 (2022); doi: 10.1063/5.0077323
Submitted: 1 November 2021 · Accepted: 22 December 2021 ·
Published Online: 12 January 2022

Behzad Forouzi Feshalami,[1,a)] Shuisheng He,[2] Fulvio Scarano,[3] Lian Gan,[4] and Chris Morton[5]

AFFILIATIONS

[1]Department of Civil and Environmental Engineering, Norwegian University of Science and Technology (NTNU), Trondheim NO-7491, Norway
[2]Department of Mechanical Engineering, University of Sheffield, Sheffield S1 3JD, United Kingdom
[3]Aerospace Engineering Department, TU Delft, Delft 2629 HS, The Netherlands
[4]Department of Engineering, Durham University, Durham DH1 3LE, United Kingdom
[5]Department of Mechanical and Manufacturing Engineering, University of Calgary, Calgary, Alberta T2N 1N4, Canada

[a)]**Author to whom correspondence should be addressed:** forouzibehzad@gmail.com. **Tel.**: +989303790254

ABSTRACT

Experimental studies dealing with the wake of isolated stationary bluff bodies are reviewed. After briefly recalling the pioneering works in this domain, the paper focuses on recent research conducted with the latest experimental methods and techniques. The review encompasses a range of topics, including the effects of bluff body geometry (non-circular cross sections and non-uniformity in spanwise direction), steady and unsteady (periodic and non-periodic) inflow conditions, surface proximity (rigid wall, confinement, and water free surface) and non-Newtonian fluids. Focus is brought to the flow physics of the wakes, especially the complex three-dimensional and oscillatory behaviors induced by the periodic vortex shedding phenomenon. The paper aims to offer a critical and systematic review of new knowledge and findings on the subject area, as well as the most frequently adopted experimental techniques. The review also helps identifying knowledge gaps in the literature that need to be addressed in future investigations.

I. INTRODUCTION

The wake that develops behind a bluff body is of fundamental scientific interest to the fluid mechanics community and a topic of relevance for many engineering applications. The knowledge on the fluid dynamic behavior around bluff objects is, for instance, of importance to the design and optimization of civil structures, aircraft systems, and mechanical engineering devices to mention but a few. Particular examples include wind turbine masts, aircraft landing gears, powerlines, pipelines, risers, and heat exchangers. Therefore, a large number of investigations have been carried out toward understanding the flow characteristics around bluff bodies along with the development of vortical flow structures in the last decades, leading to substantial progress in the physical understanding of the fluid and structure interactions, which often result in a more efficient or safer design of such systems.

Williamson published three influential review articles on wakes, and each covered a specific aspect of the topic.[1–3] It is indeed useful to categorize the vast compendium of knowledge around bluff body wakes into suitable groups to better understand the subject. Categorizations are most often based upon the geometrical configuration (e.g., 2D vs 3D and cylindrical vs non-cylindrical), object kinematics (stationary, vibrating, or flapping objects), or flow regimes (e.g., laminar vs turbulent). Furthermore, the interactions of bluff bodies in the close proximity of each other, as widely encountered in tube bundles, mooring lines, and subsea pipelines, form another category,[4] given that the flow exhibits different characteristics compared to that of the isolated bluff body case.[5] Flow-induced vibrations, including vortex-induced vibrations, wake-induced vibrations, galloping, and energy harvesting, can be considered another topical group, which focuses on fluid–structure interactions resulting from large-scale periodic aerodynamic loads and the elastically restrained bluff body. This research area has received much attention in recent decades.[6–11] Furthermore, studies dedicated to the flow around 3D geometries arising from spanwise inhomogeneity, truncated cylinders, and presence of wall have formed another realm of research. Finally, the analysis of special flow conditions like the multiphase and non-Newtonian regimes around bluff bodies is also a research domain that has raised considerable interest for applications in biochemical problems.

Categorizing the investigations by the specific methodology, namely, experiments or numerical simulations, may also be instructive to those approaching the field with a need of identifying an appropriate technique for the study of choice. Other classifications regarding the fluid flow around bluff bodies have been described in Ref. 12.

Since accurate numerical methods like the direct numerical simulation had not been well developed until 1990s, most of the studies regarding the classical perspective have been conducted experimentally. Therefore, experimental techniques with qualitative and quantitative approaches have played an important role to bring this field of study to maturity. Arguably, the first document describing the flow developing around stationary bluff bodies immersed in a water stream is attributed to Da Vinci (ca. 1513), an example of which is shown in Fig. 1 (left). However, modern scientific studies have largely stemmed from the seminal, independent works of Bénard[13] in 1908 as illustrated in Fig. 1 (right) and Von Kármán[14] in 1911 where a single two-dimensional circular cylinder was subjected to an unbounded uniform cross-flow. Studies on this classical problem have been well documented in the literature particularly from 1980 and have been comprehensively reviewed by Matsumoto.[15] Also, investigations of vortex dynamics with a focus on the three-dimensional behavior of the wake flow have been reviewed by Williamson.[1,3] Analysis of the fluctuating nature of the flow around bluff bodies exhibited in the pressure, velocity, and aerodynamic forces was the subject of the survey conducted by Hunt *et al.*[16] and Norberg.[17] Most recently, Derakhshandeh and Alam[18] carried out a survey of the flow structures and features in the wake of circular and sharp-edged cylinders at different flow regimes. Bluff bodies and wake–wall interactions were addressed by Thompson *et al.*[19] It is worth mentioning that many studies in the field of bluff body wakes have been dedicated to flow control, which is beyond the scope of the present review.[20–25]

The present review covers the latest advancements of experimental investigations focusing on the physical behavior of the wakes behind bluff bodies. The work is organized as follows: a short summary is given of the most commonly adopted experimental methods and techniques, which is followed by a discussion on the available studies in the literature regarding the classical perspective of the problem that focuses on the effect of the Reynolds number on the wake behavior (2D, isolated and stationary circular cylinders), as originating from the work of von Kármán.[14] Studies covering the effects of bluff body geometry, unsteady inflow, surface proximity, and non-Newtonian fluids are then discussed in dedicated sections. The effects of finite length cylinders are also considered. To limit the scope of this review article, other topics, including highly three-dimensional bodies (sphere-like), interacting cylinders, and cylinder in motion (rotational or oscillatory), are not covered.

FIG. 1. (Left) Leonardo da Vinci, sketches of the flow around bluff bodies partially immersed in a water stream (1513). (Image mirrored for text reading) (Right) Henri Bénard first cinematography of alternating vortices (Kármán–Bénard wake) past a cylinder towed in water.[13]

II. EXPERIMENTAL METHODS FOR BLUFF BODY WAKE INVESTIGATION

The most fundamental and commonly utilized experimental techniques to study bluff body wakes are commonly divided into qualitative visualizations and quantitative measurements. While the qualitative approach enables the researcher to rapidly capture the complex flow pattern around the bluff body, the quantitative approach provides experimental repeatability, by means of numerical values for a selected flow property, most often the fluid flow velocity or surface pressure.

A. Flow visualization techniques

These methods have been very instrumental to give hints on main flow phenomena and separate for instance laminar from turbulent or 2D from 3D regimes. However, in recent days, they have been superseded by the emergence and development of more sophisticated measurement methods like PIV that simultaneously visualizes the flow and also provides a quantitative evaluation of the velocity and vorticity field.

1. Smoke and dye injection

Flow visualizations in wind tunnels and water channels by means of smoke and dye are considered among the oldest techniques in fluid mechanics. The popularity of these techniques stems from the low cost and ease of implementation. It is of importance to employ a tracer material with the ability to scatter light and possibly neutrally buoyant, to minimize the discrepancy between the motion of fluid and tracer. The pattern produced by the visualization strongly depends upon the position of the emitter and the method how tracers are added. As a result, the revealed insight is somewhat dependent on the experimental conditions, which limits the repeatability of results. Dye probes are the most common instrument in water channels for the injection of the tracer into the fluid flow because they can be easily moved within the flow and dye can be released anywhere required. However, disturbance to the fluid flow is the main disadvantage of this method. In wind tunnels, smoke injection into the fluid flow is typically performed in the test section free-stream or best in the settling chamber via a pipe that is oriented parallel to the fluid flow.[26,27]

2. Surface-oil flow

By this technique, the object is coated with a thin layer of viscous liquid before the experiment. The flow shearing action produces traces

or lines of striations to be identified with skin friction lines. Therefore, the coating should be on the one hand sufficiently runny (thin) not to affect the near-wall flow region and, on the other hand, it has to be sufficiently viscous (thick) to prevent flushing out. Viscosity of the coating liquid, velocity, pressure, and temperature of the flow and image recording techniques are factors affecting the quality of the flow visualization. This technique has proven useful to detect flow separation. For the investigation of two- or three-dimensional, planar- or axisymmetric problems, the method has been employed to reveal the near-surface flow topology with separation lines and critical points.[28]

3. Hydrogen bubbles

The use of the hydrogen bubble technique has been widely reported in the literature for the study of boundary layers, turbulence, separated flows, and wakes. Hydrogen bubbles are generated by electrolysis, from a thin conductive wire, used as the cathode of a DC circuit, placed upstream of the region of interest. The electric circuit closes downstream at the anode. Simplicity and cost-effectiveness are two advantages of this technique. Furthermore, hydrogen bubble probes can be used anywhere in the flow field regardless of the orientation. However, effectiveness of this method is limited to water flows at relatively low Reynolds numbers. The latter is due to the orderly pattern of bubbles being rapidly lost due to turbulent mixing. The high rate of trial and error is considered as a drawback of this technique. Moreover, due to the delicate nature of the small diameter wires, they need to be treated carefully.[27] This technique has been developed by Morton and Yarusevych[29] for the simultaneous visualization of three-dimensional flow and surface over bluff bodies.

4. Smoke-wire

Smoke-wire technique acts somehow similar to the hydrogen bubble method. However, the former is used as a flow visualization method in wind tunnels. In this technique, a thin layer of oil that covers the wire tends to agglomerate into small droplets and evaporates once the wire is heated. In order to produce a uniform concentration through the entire length of the wire, droplets have to be evenly spaced and of the same size. The main benefit of this method is the measurement of the velocity profile in the air, which is a challenging task owing to a higher degree of tracers (smoke) diffusion in the flow. This method is also used for a visualization of complex three-dimensional flows such as separation bubbles and the Kármán vortex street behind a circular cylinder. In comparison with the smoke generator method, the smoke-wire technique is considered as a relatively inexpensive method.[26,27]

B. Quantitative approaches

Pressure and velocity are two important parameters in fluid mechanics that have enabled researchers to quantitatively study the behavior of the fluid flow around bluff bodies. This section is started with experimental methods for the measurement of the surface pressure and aerodynamic forces. After that, experimental techniques for velocity measurements that can be divided into intrusive and non-intrusive methods are briefly discussed.

1. Surface pressure and aerodynamic force measurement methods

Pressure can be measured at the free stream or over a model's surface.[30–33] Small orifices or tappings are conventional instruments for the pressure measurement over a model's surface or a wall.[26] These tappings or orifices are connected to a transducer, which converts the sensing pressure to an electrical signal, via a mechanical or electric scanner. In comparison with a mechanical scanner, an electric scanner has a scanning rate that is significantly higher while also reducing the response time. Transducers are further divided into passive and active types. While active transducers, such as piezoresistive element and piezoelectric element, are based on the direct measurement of the pressure, passive ones, including stain gauges and variable reluctance, rely on indirect measurement of the pressure through detecting deformation of a membrane under pressure force.[28] The measurement domain of common types of active and passive transducers is compared in Fig. 2.

Forces and moments acting on a test piece in the wind tunnel are important parameters, which are typically measured by multi-component (one to six) balances. A six-component balance is capable

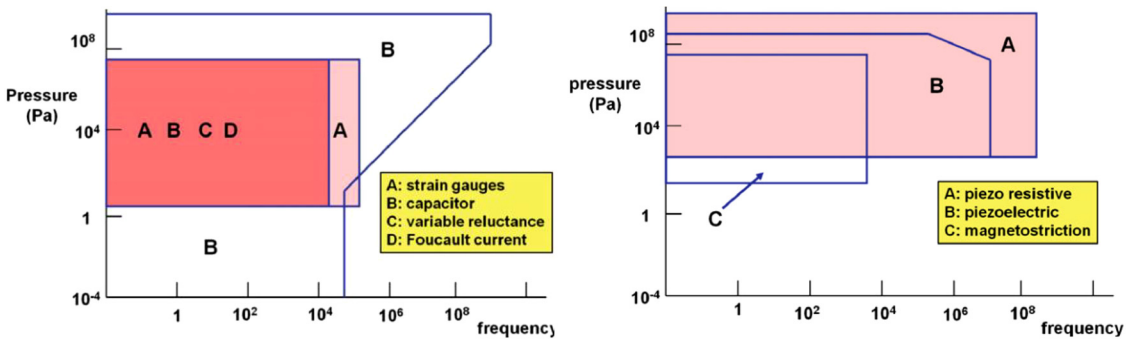

(a) passive transducer (b) active transducer

FIG. 2. Measurement domain of (a) passive and (b) active transducers. From Chanetz *et al.*, *Experimental Aerodynamics.* Copyright 2020 Springer Nature. Reproduced with permission from Springer Nature.[28]

of measuring three force components of lift, drag, and side, and three moment components of yaw, roll, and pitch simultaneously. The forces and moments can be steady or fluctuating in a flow concerned, and correspondingly, strain gauge and piezoelectric balances can be used, respectively. In contrast to the stain gauge type, piezoelectric balances offer a high rigidity and consequently much higher natural frequencies, which are appropriate for unsteady applications. Based on the installation location, balances are divided into internal and external types. While internal balances are located inside the model, external balances are positioned outside the body or the wind tunnel.[26] In comparison with external balances, internal ones benefit from a better dynamic range and a smaller size. External balances are further divided into the sidewall or the direct type in which the body is connected to one side of the wind tunnel wall, and the indirect type or the connection via supports where the balance is placed either over or below the test section. The indirect external balance provides a higher flexibility and accuracy compared to the sidewall type.[34] It should be mentioned that internal balances can be further divided into box and sting balances.[26]

2. Pressure-based velocity measurement methods

Pressure probes, namely, Pitot tube and Prandtl tube, which are used for the measurement of total and static pressures, respectively, can be indirectly employed for the determination of the flow velocity in the wind tunnel.[28] Although this technique is intrusive, it benefits from simplicity and low cost.[26] In applications with three-dimensional flows or an unknown incoming flow angle such as the swirling flow, more sophisticated types of pressure-based velocity measurement methods, for example, multi-hole cobra probes, can be implemented.[26,28,35] The cobra probes are composed of a stagnation pressure hole, which is symmetrically surrounded by static pressure holes.[26] Three-hole and five-hole probes, which are more common, are used for the measurement of the boundary layer and three velocity components, respectively.[28] Information about four-hole and seven-hole types can be found in Refs. 36 and 26, respectively. This technique was successfully implemented for the measurement in vortex tubes,[37] turbulent mixing layers,[38] and planar turbulent flows.[39] However, it suffers from several sources of error due to instantaneous yaw and three-dimensional fluctuation intensity in the turbulent flow, larger disturbance of the probe, and flow separation. Furthermore, it is not recommended for flows with a significant gradient in the total pressure.[26]

3. Hotwire anemometry

Hotwire anemometry (HWA) has been considered as a classical technique for a local and indirect measurement of high frequency and amplitude velocity fluctuations. The wire is usually made of platinum or tungsten and has a few micrometers in diameter. In this technique, the velocity of the fluid flow can be related to the convective heat transfer of the electrically heated wire. A good frequency response together with high accuracy and resolution for a wide range of velocity makes this method suitable for the measurement of flows with rapidly altering velocity such as in transient and turbulent regimes. However, this technique is not recommended for flow that contains hard particles due to the fragility and sensitivity of the wire. In addition, owing to the directional insensitivity, hotwires are not adequate for measurements where large changes occur in the flow direction (e.g., separated or recirculating flows).[28,34,40] The above problem is mitigated with the flying hotwire technique,[41] however, superseded by the laser Doppler velocimeter (LDV). Nonetheless, the hotwire remains a powerful tool for the high-temporal resolution needed in the analysis of turbulent boundary layers, wakes, and jets.[26]

The emergence of laser-based techniques has revolutionized flow measurement methods due to the capabilities they have shown for measuring flow velocity non-intrusively. Laser Doppler velocimetry (LDV) and particle image velocimetry (PIV) are two popular and well-known laser-based techniques that have been extensively used for flow velocity measurement in past decades.

4. Laser Doppler velocimetry

LDV is an efficient and accurate instrument for non-intrusive measurement of the local and instantaneous velocity. In this technique, the velocity is measured by determination of the frequency change (Doppler shift) with respect to the incoming laser light, when scattered by small particles moving with the fluid (Fig. 3).[34] A small measurement volume is generated where two laser beams, obtained splitting a single laser beam, are focused and cross each other at the desired location.[28] The photodetector receives the scattered light from tracer particles crossing the pattern of fringes and the frequency of the signal is translated into the particle velocity. In contrast to the hotwire method, LDV requires no calibration.[42] Developments over several decades have rendered LDV an instrument with high spatial resolution and measurement accuracy, with a wide velocity range, including supersonic flow regimes. Directional sensitivity has become possible with the frequency shifting technique alongside the measurement of multiple velocity components.[26] As a result, LDV has been used for the detailed characterization of the Reynolds stress tensor components, of primary importance in turbulent flows, and to support the development of advanced RANS models. One of the shortcomings of LDV is that the velocity is only measured when a tracer is crossing the measurement volume, resulting in irregular spacing of the samples in time. Thus, the hotwire is more appreciated in applications requiring a robust and higher frequency response.[28]

5. Particle image velocimetry

PIV has attracted much attention in recent decades as a versatile and accurate technique for the measurement of flow fields. Tracer

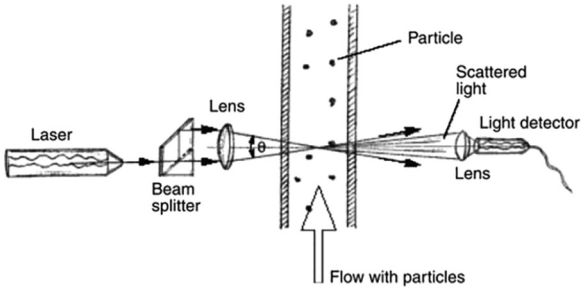

FIG. 3. Configuration of a LDV measurement setup. From Wilson, *Sensor Technology Handbook*. Copyright 2005 Elsevier. Reproduced with permission from Elsevier.[42]

particles are inserted in the fluid flow and illuminated over a plane or a volume of interest at least twice, separated by a short time interval. By recording the light scattered by these particles, the displacement is obtained via spatial cross-correlation techniques,[43] in turn yielding their instantaneous velocity. PIV combines the immediacy of insight offered by flow visualization techniques and the repeatability of experiments characteristic of quantitative measurements.[40] A major advantage to LDV is that PIV yields the measurement of the instantaneous velocity field at multiple spatial locations simultaneously, therefore paving the way for the analysis of the instantaneous vorticity, of paramount importance in vortex-dominated flows. In unsteady flow regimes, the flow characteristics are time-dependent and the use of LDV to derive correlations becomes challenging. The latter limitation along with the cost and effort required for the alignment of LDV systems has made PIV the preferred choice for bluff body flows. Nevertheless, LDV remains valuable in some applications like boundary layer measurements, where it attains near-wall measurement resolution on the order of 100 μm.[28] The fundamentals of PIV measurement for two components of velocity with a single camera have been fully established and available in textbooks.[43] In this section, the progress of the PIV technique is briefly reviewed, focusing on PIV configurations that have played a leading role to advance the knowledge of bluff body wakes.

a. Planar PIV. Two components of velocity can be measured in two dimensions (2D-2C PIV) with a plane of light formed by a laser sheet [Fig. 4(a)].[28] Although very popular for its simplicity, this method only yields the in-plane velocity components, whereas the out-of-plane component is not captured, with some limitations in the assessment of the physical behavior of three-dimensional flows.[44]

The stereoscopic PIV technique overcomes the above limitation and yields three velocity components of the velocity vector in a two-dimensional domain (2D-3C PIV), as illustrated in Fig. 4(b). The particle image motion is captured from two directions and combined to yield the three components.[28] The angular method (by lens-tilt adapters) is the most practiced as it allows larger viewing angles and a higher accuracy of the out-of-plane component.[26] Compared to fully three-dimensional PIV methods, stereoscopic PIV remains a simpler option for measuring three components of velocity.[44]

b. Scanning PIV (N×2D-3C). This technique is based on the standard planar PIV and introduces rapid scan of the light sheet across the measurement volume, while the particle images are recorded by one or more cameras.[34,46] The result is a straightforward approach to image processing, and the in-plane spatial resolution remains as high as that of planar PIV. However, high repetition rate illumination and imaging hardware are required, along with the use of the optical scanning system.[46] Furthermore, the application of the method remains limited to low-velocity experiments because the volume scanning time needs to be smaller than the time-scales of the unsteady or turbulent phenomenon under investigation. If the above requirement is not respected, a distorted representation of the flow structure may occur.[34]

c. Tomographic PIV (3D-3C). The simultaneous measurement of the three velocity components over a volume requires, multiple viewing directions, typically 3–4 cameras, and the illumination is thickened from a sheet to a volume (Fig. 5).[28] The 3 D intensity field of the scattering particles is reconstructed over discrete voxels arranged on a Cartesian mesh. Furthermore, the particle displacement is evaluated by spatial cross-correlation, this time performed over cubic interrogation volumes. This technique has impacted fluid mechanic research enabling researchers to investigate complex fluid flows such as turbulent flows in three dimensions.[34] It is worth mentioning that spatial resolution in this method sits in between particle tracking velocimetry (PTV) (low seeding density) and the scanning PIV method (high seeding density).[46]

d. 3D particle tracking velocimetry (3D-3C). In this case, the motion of PIV tracers is identified on individual basis. The hardware setup and the preparation stages like the optical calibration remain identical to tomographic PIV. However, the post-processing is much more rapid and less memory intensive than that required for

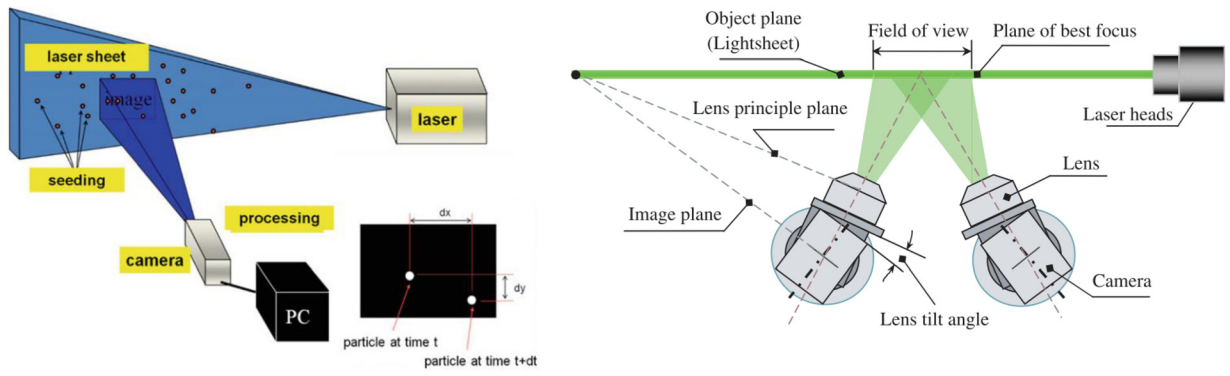

FIG. 4. Schematic description of planar PIV for the measurement of (a) two velocity components. From Chanetz *et al.*, *Experimental Aerodynamics.* Copyright 2020 Springer Nature. Reproduced with permission from Springer Nature.[28] (b) Three velocity components. Reproduced with permission from Liu *et al.*, Chem. Eng. Sci. **61**, 4252–4261 (2006). Copyright 2006 Elsevier.[45]

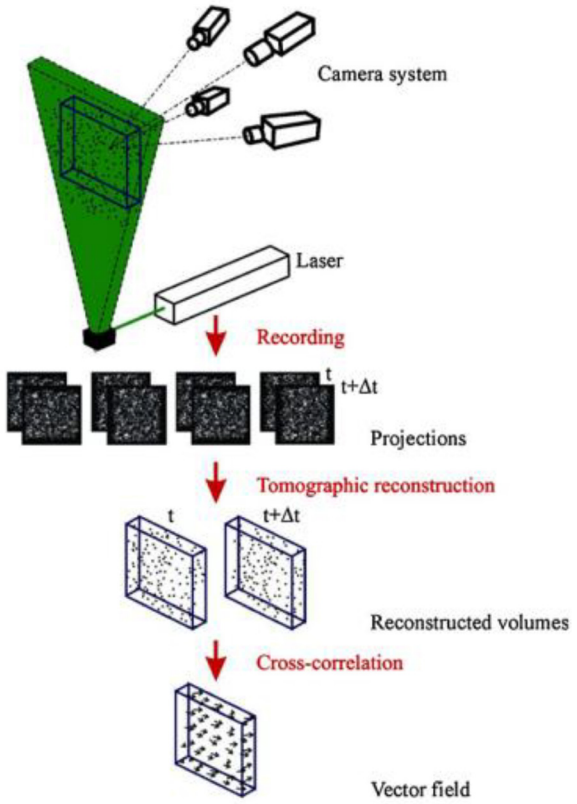

FIG. 5. Schematic description of tomographic PIV. Reproduced with permission from Elsinga *et al.*, Exp. Fluids **41**, 933–947 (2006). Copyright 2006 Springer Nature.[46]

tomographic PIV, especially with the Shake-the-Box algorithm.[47] As a result, 3D measurements by tomographic PIV are now becoming superseded by Lagrangian particle tracking methods.

III. EFFECTS OF REYNOLDS NUMBER (CLASSICAL PERSPECTIVE)

A bluff body is defined as a non-streamlined object in that the flow separation makes the streamlines deviate from the contour of the object in its aft part.[48] The circular cylinder is by far the most extensively studied bluff body, which has been the focus of many investigations in the last century. Past studies have indicated complexities of wake behind circular cylinders. In particular, the wake properties exhibit a strong dependence upon the Reynolds number, based on the cylinder diameter D and free-stream velocity U_∞, leading to the definition of distinct flow regimes as illustrated in Fig. 6.

Roshko[49] identified seven flow regimes based on the variation of the base pressure coefficient (calculated at a position 180° from the front stagnation location[1]) vs Reynolds number (Fig. 6). Such conditions were divided by Cadot *et al.*[50] into four categories of subcritical ($Re < 2 \times 10^5$), critical ($2 \times 10^5 \leq Re \leq 5 \times 10^5$), supercritical ($5 \times 10^5 \leq Re \leq 5 \times 10^6$), and transcritical ($Re > 5 \times 10^6$). It should be mentioned that discrepancies in the boundary values of these categories have been reported and disputed in the literature.[18,49,51] Referring to Fig. 6, flow regimes of laminar vortex shedding (A-B), secondary

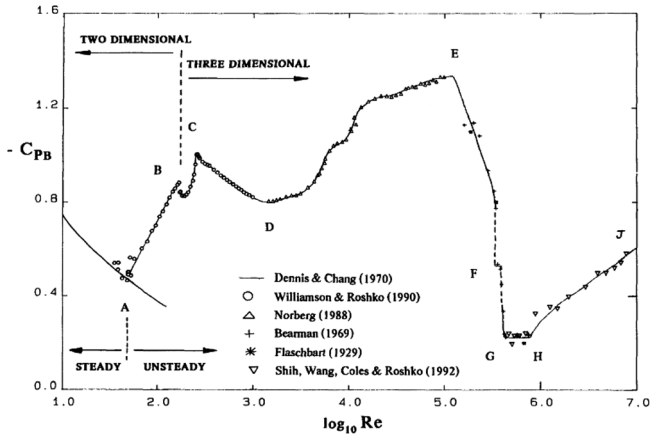

FIG. 6. Variations of the base pressure coefficient with Reynolds number.[49] (up to A) Laminar steady regime, (A-B) laminar vortex shedding, (B-C) 3D wake-transition regime, (C-D) disorder increment in the fine-scale three dimensionalities, (D-E) shear-layer transition regime, (E-G) asymmetric reattachment, (G-H) symmetric reattachment, and (H-J) boundary-layer transition regime. Reproduced with permission from Roshko, J. Wind Eng. Ind. Aerodyn. **49**, 79–100 (1993). Copyright 1993 Elsevier.[1]

vortices (B-C), shear layer vortices (D-E), and finally the laminar separation bubbles (E-H), which were introduced in Refs. 1 and 49, are the focus of this paper. It is worth mentioning that the aforementioned classifications are based on a standard circular cylinder and could be changed by many factors like surface roughness and the degree of three dimensionalities.[1] Readers are referred to Refs. 52–55 for detailed discussions on the effects of aspect ratio [the ratio of cylinder's length (L) to its width (W)].

A. Laminar vortex shedding ($50 \leq Re \leq 190$)

The first transition occurs in this flow regime where the shedding of vortices and the formation of a vortex street begins to appear. The Reynolds number where the transition occurs is named critical Reynolds number and is specified to be 49.[1] Before such value Reynolds number, the flow regime is steady and two counter-rotating symmetric recirculation regions develop on each side of the wake (Fig. 7).[56] It was shown that the length of these vortices increases with Reynolds number in this flow regime.[57]

After exceeding this first critical Reynolds number, oscillations of the separated region appear in the wake and the flow regime initiates periodic oscillations.[58] Consequently, large and spanwise

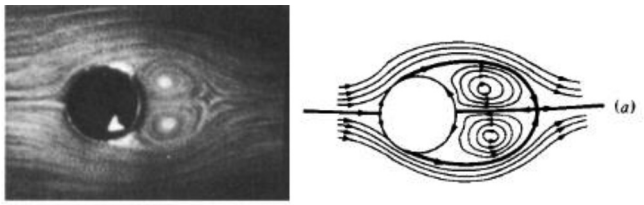

FIG. 7. Flow visualization behind a circular cylinder in the steady flow regime. Reproduced with permission from Perry *et al.*, J. Fluid Mech. **116**, 77–90 (1982). Copyright 1982 Cambridge University Press.[56]

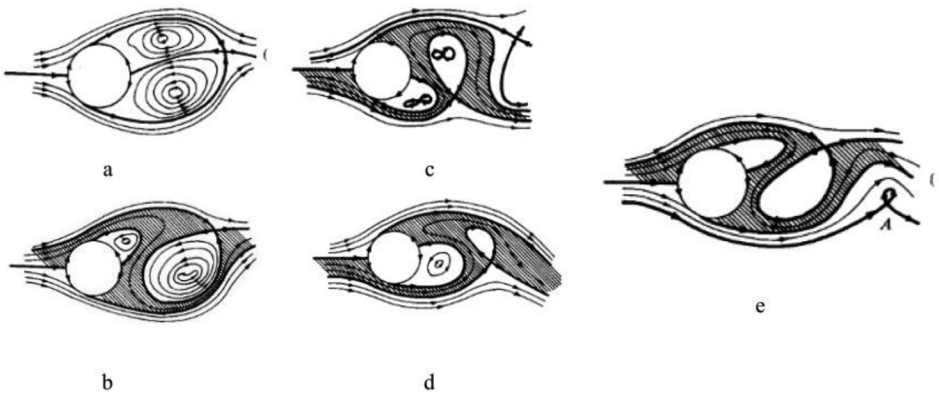

FIG. 8. Time progression of onset of the laminar vortex shedding. Vortex shedding is started with (a) and continues to (e) with the non-dimensional time increment ($U_\infty \Delta t/D$) of 0.3. Reproduced with permission from Perry *et al.*, J. Fluid Mech. **116**, 77–90 (1982). Copyright 1982 Cambridge University Press.[56]

homogeneous vortices are shed from the rear surface and transported downstream.[59] The transition to vortex shedding occurs when the recirculation region, which had been formed behind the circular cylinder in the steady flow regime, is opened, and immediate fluid alleyways are penetrated into the recirculation region.[56] This process is schematically shown in Fig. 8. It should be mentioned that the mixing resulting from the unsteady flow in the laminar vortex shedding is strong in the near-wake zone, leading to a contraction of the formation length.[1]

While most investigations in this flow regime have been dedicated to the near-wake region, some researchers studied the far-wake zone, generally defined as the region past three cylinder diameters and up to hundred diameter downstream.[60] By visualizing the fluid flow for $70 < Re < 154$, Karasudani and Funakoshi[61] described an almost parallel shear flow with a Gaussian profile downstream of the primary vortex street. According to Fig. 9(a), Vorobieff *et al.*[62] came to the same conclusion and manifested that these two parallel shear layers are converted to the second wake, which moves upstream toward the cylinder when the Reynolds number increases [Fig. 9(b)]. Lin and Hsieh[63] found that at Reynolds number 160, the ratio of the convection velocity of the shed vortices to the freestream velocity increases from 0.53 to 0.84 for $1.6 < x/D < 6$ and remains constant for $x/D > 6.0$.

B. Transition toward three-dimensional regimes ($190 \leq Re \leq 260$)

With a further increase in the Reynolds number to around 190, secondary vortices that had been formed at the far-wake region in the previous flow regime move upstream to the near-wake zone.[62] In this flow regime, the second transition, that is, inception of three dimensionalities, starts and secondary, longitudinal, or streamwise vortices are created. This flow regime is mainly characterized by two patterns, known as mode A and mode B, and can easily be identified in the base pressure coefficient vs Reynolds number diagram in Fig. 6.[64] Referring to Fig. 10(a), in mode A, streamwise vortex loops are formed with a spanwise length scale, defined as the distance between vortex pairs in the spanwise direction,[65] around 3–4 cylinder diameters.[1] As schematically shown in Fig. 11(a), tongue-shaped vortex sheets are observed in mode A, which pass one Kármán vortex tube and cover the subsequent one. Each tongue contains vortex lines (dashed lines), which are stretched in the streamwise direction, resulting in the formation of a pair of secondary vortices.[66] Gerrard[67] described the vortex topology of this mode as fingers of dye, and Zhang *et al.*[68] characterized it as a hysteretic discontinuity or a hard transition. Gibeau and Ghaemi[59] stated that these vortices alter their rotation direction in half of each shedding cycle of the primary instability.

The second discontinuity or mode B starts when the Reynolds number reaches 230–250.[1] This mode, as demonstrated in Fig. 10(b), contains finer-scale, more uniform, and softer streamwise vortices and has a spanwise length scale of around one cylinder diameter.[69] As can be seen in Fig. 11(b), Brede *et al.*[66] described the secondary vortices in this mode as continuous vortex tubes, and in some studies, the structure was found resembling a mushroom.[2,70] It was also found that the vortices in this mode maintain their rotation directions during the primary shedding cycles.[59] Wei and Smith[71] claimed that the instability of the free shear layers causes the separated boundary layer to roll up

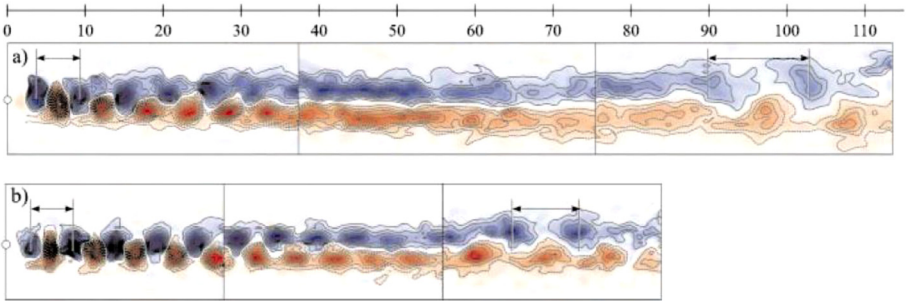

FIG. 9. Instantaneous vorticity behind a circular cylinder (a) $Re = 100$ and (b) $Re = 150$. Reproduced with permission from Vorobieff *et al.*, Phys. Fluids **14**, 53–56 (2002). Copyright 2002 AIP Publishing LLC.[62]

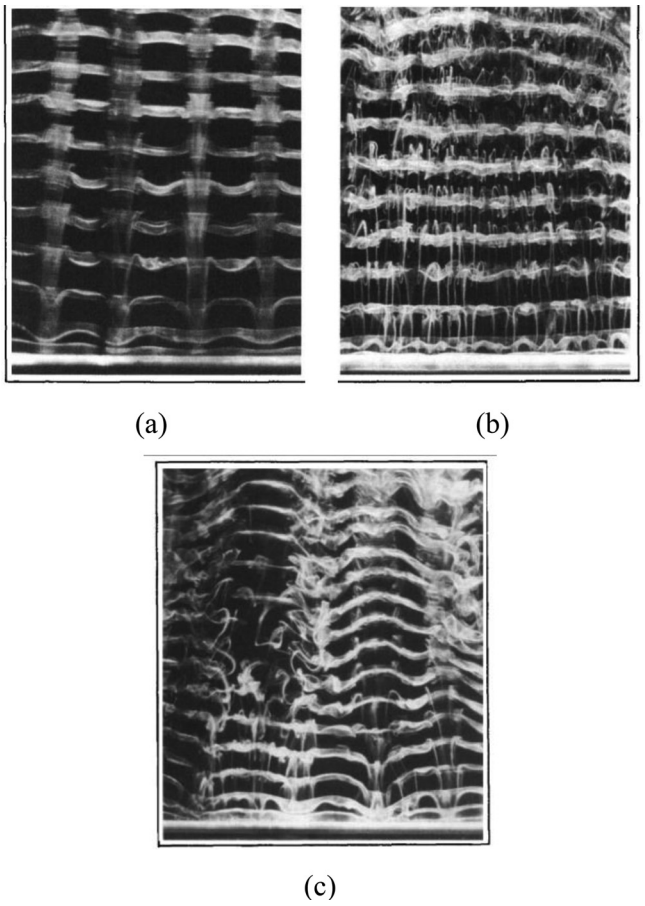

FIG. 10. Spanwise flow visualization by a laser light and fluorescein dye behind a circular cylinder (a) mode A, (b) mode B, and (c) vortex dislocations. Reproduced with permission from Williamson, J. Fluid Mech. **243**, 393–441 (1992). Copyright 1992 Cambridge University Press.[69]

and form the streamwise vortices. However, Williamson *et al.*[72] concluded that streamwise vortices could be found in the vortex street and also in the shear layers separating from sides of the body. Brede *et al.*[66] proposed that the braid-like instability region between the primary Kármán vortices owing to centrifugal forces is the main reason for the formation of mode A, while mode B is created due to the instability of the separating shear layer in the near-wake. Soria[73] highlighted that three dimensionalities in the near-wake region could be ascribed to the penetration of a notable high-velocity upstream fluid toward the stagnant zone in the near-wake at the x-y plane (normal to the cylinder axis). It was shown that this upstream influx is shifted normal to the x-y plane when it reaches the cylinder's stagnation zone. It is worth mentioning that end-walls and aspect ratio of the model play important roles in the primary vortex shedding from the cylinder and are of high importance in capturing mode A and mode B in experiments.[74–76]

In addition to these two modes or discontinuities, another pattern could be identified in this range of Reynolds number, which is referred to as large-scale vortex dislocations or adhesions.[77,78] This phenomenon, which is visualized in Fig. 10(c), is characterized by a

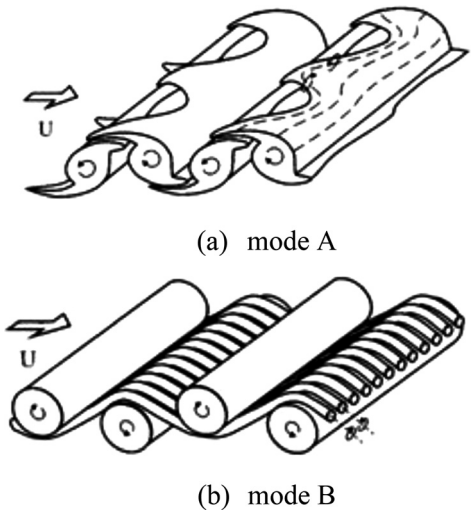

FIG. 11. Schematic representations of primary and secondary vortices (a) mode A and (b) mode B. Reproduced with permission from Brede *et al.*, Phys. Fluids **8**, 2117–2124 (1996). Copyright 1996 AIP Publishing LLC.[66]

large intermittent low-frequency fluctuation of velocity, and the vortex structure is enlarged moving downstream.[69,79] Vortex dislocations are generally occurring where particular vortex loops exist (mode A) and develop spontaneously spanwise.[1] Williamson[69] highlighted that dislocations are the main cause of the large-scale distortion as well as the breakup to the wake turbulence. Zhang *et al.*[68] highlighted a different kind of three dimensionalities, namely, mode C, with a spanwise length scale of around two cylinder diameters. This mode, which was observed in the Reynolds number range of 170–270, significantly decreases the Strouhal number ($Sr = fD/U$, where f denotes the dominant frequency). Another mode, namely, quasi-periodic (QP), was detected by Barkley and Henderson[80] using a Floquet stability analysis of the wakes behind the circular cylinder. This mode occurs at a higher critical Reynolds number than those of modes A and B, while its spanwise wavelength lies in-between.[81] Vortex pairs in the quasi-periodic mode alter their rotation direction after every primary shedding cycle.[59] Blackburn *et al.*[82] added that while modes A and B are synchronous, one breaking and one maintaining the space–time symmetry, the bifurcated state in the quasi-periodic mode might be regarded as a modulated traveling wave or a modulated standing wave.

Using time-resolved PIV at $Re = 360$, Sung and Yoo[83] described a secondary vortex filament in the region between two consecutive Kármán vortices, which is sequentially linked to the newly formed one and separated from the formerly linked one. Using time-resolved tomographic PIV, Scarano and Poelma[84] visualized the vorticity distribution behind a circular cylinder at $Re = 180$ (Fig. 12). They observed a different shedding regime to the literature also at a Reynolds number of 360. According to Fig. 13, they noted that the flow structure in this regime resembles rhombus vortex cells with some similarity to the pattern of vortex dislocations.

C. Vortices in the free shear layer ($1000 \leq Re \leq 2 \times 10^5$)

This flow regime is recognized in Fig. 6 as an increase in the base pressure coefficient between Reynolds numbers of 1000 and 200 000

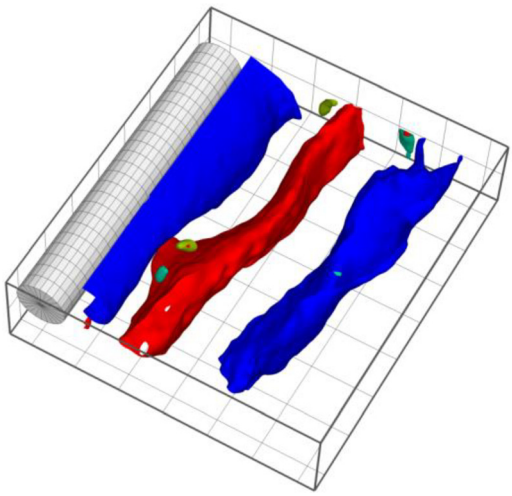

FIG. 12. Vorticity distribution at $Re = 180$ with incipient mode A (tongue) visible.[84]

and is associated with the Kelvin–Helmholtz instability, Bloor–Gerard vortices, the shear layer instability, or shear layer vortices.[85] Compared with Kármán vortices, the size of shear layer vortices is significantly smaller.[86] There is much controversy about the critical Reynolds number for the incipit of the shear layer instability.[67,75,87] The latter may be ascribed to the difficulty of reproducing the same experimental conditions for a phenomenon, like transition, that is notably sensitive to small variations of inflow conditions. For example, Wu *et al.*[70] expressed that the critical Reynolds number might be reduced in a highly turbulent background. As shown schematically in Fig. 14, the formation of shear layer vortices begins with instability in the two free shear layers separated from the circular cylinder. These shear layers are located between the formation region and the freestream. Therefore, the velocity in the outer line of the separated shear layer is close to that of the freestream, while the velocity of the inner line is close to zero. As a consequence, small-scale vortices are developed and carried downstream by the Kármán vortices.[70,71] A contraction of the formation length and a small reduction of the Strouhal number are characteristics of this flow regime.[88] Rajagopalan and Antonia[85] discovered that the position of the instability inception is moved upstream toward the cylinder with an increase in the Reynolds number in this flow regime.

Chyu and Rockwell[89] visualized the near-wake region at a $Re = 10\,000$ using PIV, showing that the three dimensionalities and the vorticity concentration are not equally developed at lower and upper shear layers. Furthermore, the formation of small-scale vortices for two shear layers does not occur simultaneously. Lin *et al.*[90] concluded that the lifetime of the streamwise vorticity at Reynolds number of 1000 is on the order of half of the Kármán vortex shedding period. Furthermore, the spanwise wavelength of the vortex tube is of the order of one cylinder diameter and increases considerably in the near-wake region.[91] Characteristics of the vortex formation, shedding, and convection at $Re = 9000$ were studied by Rockwood *et al.*[92] Khor *et al.*[93] measured the time-mean velocity profiles in the near-wake region to analyze the instability characteristics for $600 < Re < 4600$. Results indicated a region of convective instability forming instantly downstream of the separation location of the shear layers. Transition

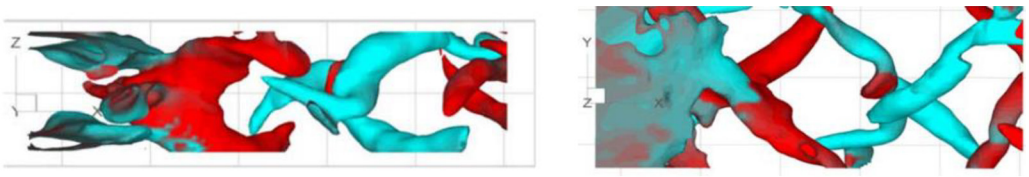

(a) side view (b) top view

FIG. 13. Rhombus vortex cells at $Re = 360$ from (a) side view and (b) top view. Reproduced with permission from Scarano and Poelma, Exp. Fluids **47**, 69 (2009). Copyright 2009 Author(s), licensed under a Creative Commons Attribution Noncommercial License (CC BY-NC 2.0).[84]

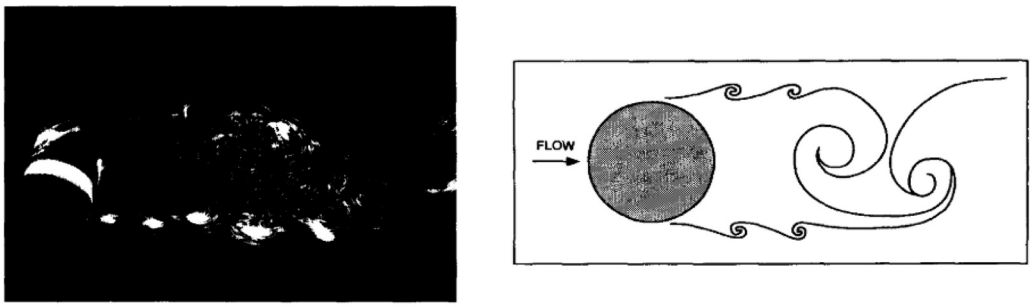

(a) (b)

FIG. 14. Visualization of the shear layer separated from a circular cylinder at $Re = 2700$ (a) water tunnel flow visualization, (b) conceptual diagram. Reproduced with permission from Wu *et al.*, Exp. Therm. Fluid Sci. **12**, 169–174 (1996). Copyright 1993 Elsevier.[70]

to absolute instability occurs further downstream with the wake development and thickening of the separated shear layer. They also showed that the development of a considerable convectively unstable zone downstream is in accordance with the initial presence of Bloor–Gerrard vortices in the shear layers mentioned in the literature when the Reynolds number is beyond about 1000. Khabbouchi *et al.*[94] investigated the effects of the freestream turbulence on the shear layer separation at $4500 < Re < 47\,000$ and showed that the breakdown of the shear layer vortices is accelerated when the turbulence intensity increases.

Elucidating the spanwise organization of vorticity requires three-dimensional measurements made possible with tomographic PIV. In the past two decades, some three-dimensional measurements of instantaneous vorticity in the wake of cylinders, ranging from $Re = 1000$ to $Re = 27\,000$, have been realized with tomographic PIV experiments in water[84] and recently in air flows (Fig. 15). In the latter, helium-filled soap bubbles have been used as tracers that allow measurements over significantly larger regions.

1. Force fluctuations

Norberg[17] conducted measurements and also reviewed available papers in the literature about the fluctuating lift over a stationary circular cylinder and concluded that the fluctuating lift coefficient significantly increases from 0.045 at $Re \approx 1600$ to 0.47 at $Re \approx 20\,000$. Blackburn and Melbourne[95] pointed out that the turbulence length scale is an influential factor on determination of the fluctuating lift at high Reynolds numbers ranging from 100 000 to 500 000. The effects of the Kármán vortex shedding on fluctuating forces of a circular cylinder were assessed by Nishimura and Taniike[96] at $Re = 61\,000$. They clarified that rolling up of a vortex behind the circular cylinder causes some amount of the separated shear layer to be transferred from the opposite side into the vortex itself, leading to the fluctuating lift force over the circular cylinder. Subsequently, the near-surface flow velocity increases, and the separation point is transferred to the leeward direction and a large lift force is generated. The static surface pressure at $Re = 19\,000$ was studied by Rockwood and Green.[48] Maryami *et al.*[97] found that the energy level of the unsteady pressure imposed on the circular cylinder goes up with increasing turbulence intensity at $Re = 14\,700$.

2. Turbulence properties

Using three-component LDV, Brede[98] examined the turbulence structure of the separated shear layers from a circular cylinder at $Re = \{5000;\ 10\,000;\ 20\,000\}$ and concluded that the maximum turbulence intensity occurs upstream of the time-averaged rear stagnation point, where the shear layer reaches the developing primary vortex. Gkiolas *et al.*[86] revealed that the peak value of Reynolds stresses at $Re = 35\,000$ occurs downstream of the vortex center, while the spanwise vorticity, swirling strength, and turbulent kinetic energy reach a maximum value at the vortex centers in a moving frame of reference.

Turbulence studies conducted at high Reynolds numbers of the subcritical regime show different features discussed herein. By measuring the near-wake turbulence properties using LDV at $Re = 140\,000$, Djeridi *et al.*[99] showed that the peak of the mean shear stress occurs at $X/D = 1.3$ and $Y/D = \pm 0.4$, with a formation length of approximately 1.5D, which is higher than that gathered by Norberg[100] (1.3D) from various authors in the high Reynolds number range. Braza *et al.*[101] measured $\overline{u^2}$, $\overline{v^2}$, and $\overline{w^2}$ at $Re = 140\,000$ and documented the two-lobe structure of streamwise fluctuations $\overline{u^2}$ attaining a maximum $X/D = 1$ and $Y/D = \pm 0.5$. In contrast, $\overline{v^2}$ and $\overline{w^2}$ have a one-lobe structure with maxima at $X/D = 1.4$ and $X/D = 1$, respectively. These locations for the maximum normal stress components are close to those reported by Djeridi *et al.*[99] Iso-contours of the Reynolds stress tensor components as obtained from the study of Braza *et al.*[101] are shown in Fig. 16.

3. Inclination effects

The angle between the flow direction and the plane perpendicular to the cylinder axis is defined as yaw angle. Zhou *et al.*[102] revealed that the rms value of streamwise and spanwise velocities and the vortex shedding frequency are reduced with increasing inclination angle. Similar to Kozakiewicz *et al.*,[103] Najafi *et al.*[104] detected two different flow patterns and a bi-stable pattern behind an inclined circular cylinder. As demonstrated in Fig. 17, the first flow pattern was observed at relatively small yaw angles, while the second at values ranges from 35° to 45°.

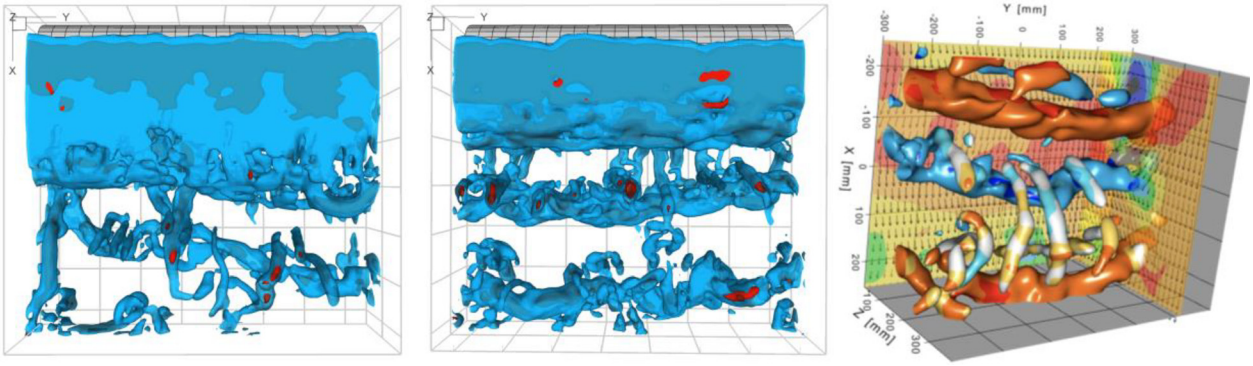

FIG. 15. Instantaneous vorticity of cylinder wake flow at $Re = 1000$ (left), $Re = 5400$ (middle),[84] and instantaneous visualization of vortices by Q-criterion at $Re = 27\,000$ (right).

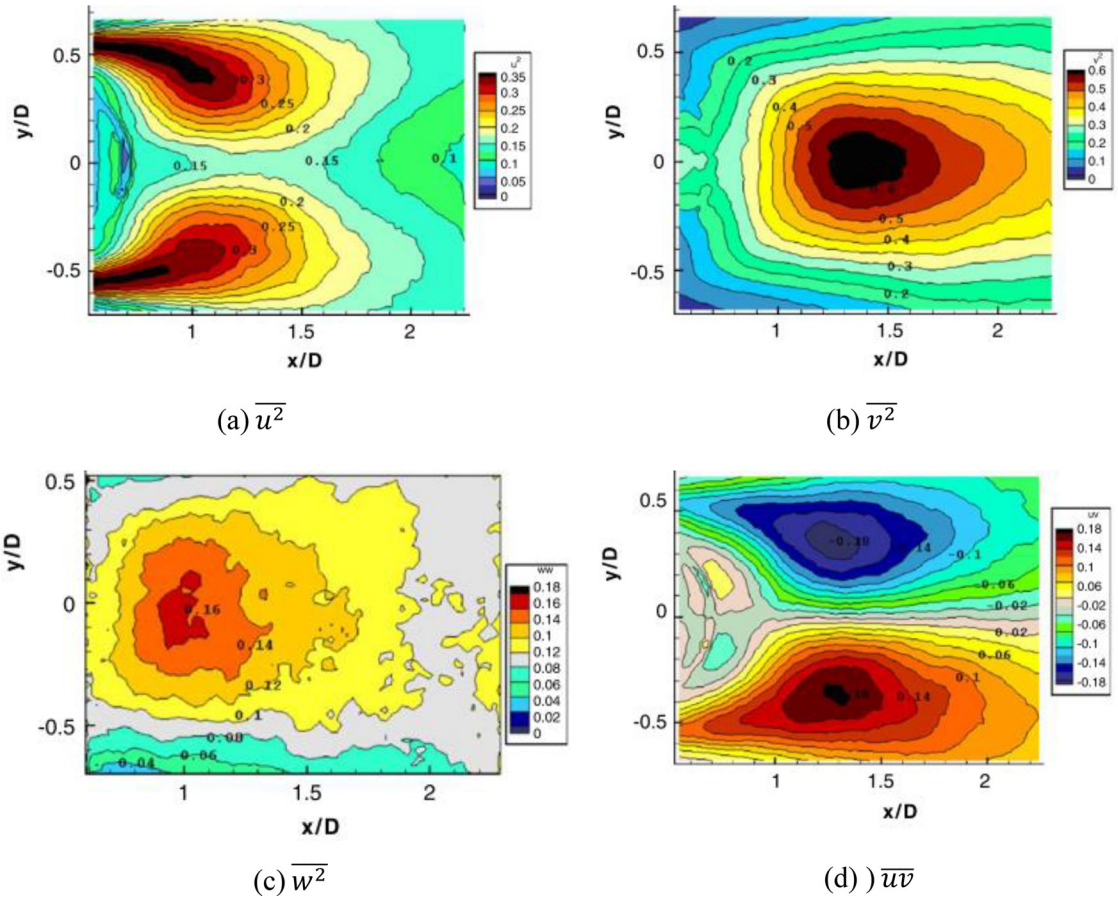

FIG. 16. Turbulence properties behind a circular cylinder at $Re = 140\,000$ (a) $\overline{u^2}$, (b) $\overline{v^2}$, (c) $\overline{w^2}$, and (d) $\overline{uv}$. Reproduced with permission from Braza *et al.*, J. Fluids Struct. **22**, 757–771 (2006). Copyright 2006 Elsevier.[101]

D. Drag crisis and laminar separation bubbles ($2 \times 10^5 \leq Re < 10^6$)

The main characteristic of this flow regime is the early flow transition within the attached boundary layer. As a consequence, an abrupt reduction of the base pressure and drag coefficient is observed (Fig. 6), also known as the drag crisis.[1] When the Reynolds number reaches a critical value, disturbances in the boundary layer occur featuring a small separation bubble on one side of the cylinder, where the disturbance is first started or amplified. Point F in Fig. 6 indicates the formation of such a separation bubble on only one side of the cylinder.

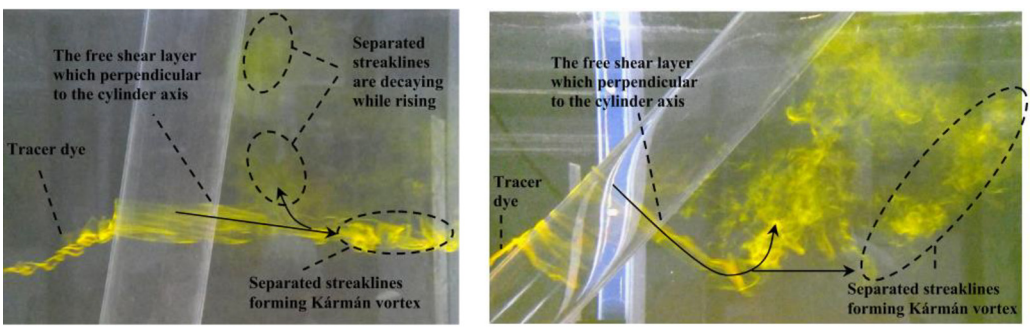

(a) the first flow pattern (yaw angle = 10°) (b) the second flow pattern (yaw angle = 45°)

FIG. 17. Instantaneous wake patterns behind an inclined circular cylinder at $Re = 5000$ (a) yaw angle = 10°, and (b) yaw angle = 45°. Reproduced with permission from Najafi *et al.*, Ocean Eng. **113**, 335–349 (2016). Copyright 2016 Elsevier.[104]

As shown in Fig. 18, this bubble is known as the laminar separation bubble and is formed when the boundary layer detaches undergoing rapid transition and reattaches in the turbulent state. This process is known as transition A, the first drop of drag or the asymmetric state, and can be recognized in Fig. 6 from point E to F. A second transition with an additional drag crisis (F-G) features a second laminar separation bubble.[1,50,51,105] It has been shown that the formation of laminar separation bubbles is an intermittent phenomenon. Furthermore, their characteristic frequency and appearance increases with Reynolds number.[106] Points G-H in Fig. 6 indicate the flow is symmetric and two laminar separation bubbles are formed, one on each side of the cylinder.

This two-stage drag crisis was also observed by Desai *et al.*[51] However, referring to Fig. 18(e), they clarified that the onset of one-bubble and two-bubble states occurs for Reynolds numbers of 379 000 and 410 000, respectively. With further increase in Reynolds number to 440 000, the two-bubble state is stabilized and the drag crisis process is completed. Miau *et al.*[107] showed that transition A belongs to subcritical category, while transition B in terms of a higher vortex shedding frequency and a narrower wake is close to the critical category. Using proper orthogonal decomposition and spectral proper transformation techniques, Qiu *et al.*[108] successfully separated the dominant aerodynamic behavior from the fluctuating pressure field over a circular cylinder for $166\,000 \leq Re \leq 828\,000$. Miozzi *et al.*[109] provided more detail about laminar separation, turbulent reattachment, and final separation for $79\,000 \leq Re \leq 238\,000$. In the same range, Capone *et al.*[110] highlighted that the increasingly energetic boundary layer is less sensitive to the fluctuations of the flow when Reynolds number reaches the critical border. Lin *et al.*[111] emphasized that the frequency of the vortex shedding seems to become higher ($Sr > 0.2$) and exhibiting larger fluctuations when one bubble is formed on one side of the cylinder only. Furthermore, the frequency of fluctuations tends to become even higher and with a broader distribution once two bubbles are installed on both sides of the cylinder.

IV. EFFECTS OF BLUFF BODY'S GEOMETRY

Compared with circular cylinder wakes, the flow around other bluff bodies, including square, rectangular or polygonal, and D-shaped cylinders, has been far less investigated. Furthermore, non-cylindrical objects with cross-sectional variation along the span have attracted attention in recent years also due to their role in mitigating vortex shedding. Section IV is dedicated to analyze the effects of non-circular cross sections and non-uniformity in the spanwise direction on the flow characteristics.

A. Non-circular cross sections

1. Square cylinders

Square or rectangular cylinders are widely implemented in architectural structures, including tower buildings and bridge decks, but also in engineering systems, such as heat exchangers. In recent years, a number of studies have been devoted to square section cylinders. Lyn *et al.*[112] revealed that although the qualitative features of the fluid flow past a square cylinder are somehow similar to circular cylinders, quantitative differences can be noteworthy. For example, the peak values of both the turbulent and periodic stresses behind a square cylinder are considerably higher than those behind the circular one. Durão *et al.*[113] emphasized that the mutual interaction of the top and bottom shear layers of the square cylinder (at $Re = 14\,000$) results in a large amplitude vortex shedding (Fig. 19).

Luo *et al.*[114] compared the wake transition to three dimensionalities of a square cylinder with that of a circular cylinder. They found

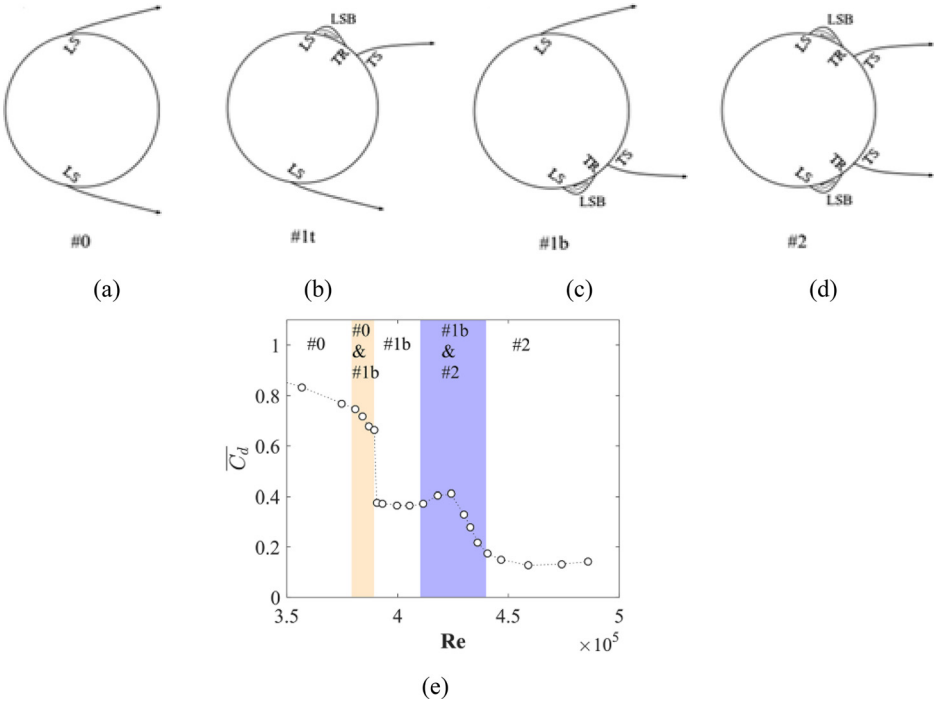

FIG. 18. (Top) Formation of the laminar separation bubbles over a circular cylinder (a) no bubble, (b) upper bubble, (c) lower bubble, (d) two-bubble states. LS, TR, and TS denote the laminar separation, the turbulent reattachment, and the turbulent separation, respectively. (Bottom) (e) Variation of the drag coefficient with *Re*. First and second transitions are indicated by the yellow and blue region, respectively. Reproduced with permission from Desai *et al.*, Phys. Fluids **32**, 014105 (2020). Copyright 2020 AIP Publishing LLC.[51]

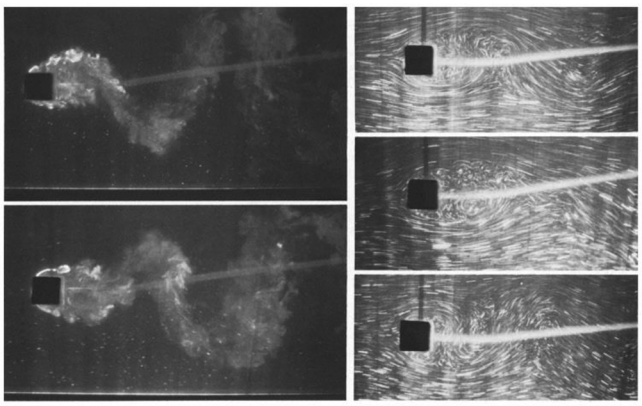

FIG. 19. Flow visualization around a square cylinder at $Re = 14\,000$. Reproduced with permission from Durão *et al.*, Exp. Fluids **6**, 298–304 (1988). Copyright 1988 Springer Nature.[113]

that the critical Reynolds for mode A and mode B appear to reduce to 160 and 200 for the square cylinder, respectively. The vortical structure of the modes was found to be similar to those past circular cylinders (Fig. 20). The mushroom structure, which was previously characterized in the circular cylinder's wake,[1] was also detected in the square cylinder. In addition, the spanwise length scale of modes A and B for the square cylinder was determined to be 5.2 and 1.2 of the cylinder's height (H), respectively, which is longer than those in the circular cylinder wake. However, Dobre and Hangan[115] reported a spanwise length scale nearly half of the mode A (about $2.4H$), which could be ascribed to their higher Reynolds number (22 000). With help of time-resolved PIV, streamlines and the periodic Kármán vortex shedding behind a square cylinder were visualized by Yu *et al.*[116] at a Reynolds number of 2150. Minguez *et al.*[117] focused on the interaction between the Kármán and shear layer vortices in the near-wake region at a Reynolds number of 21 400 and discovered that the flow separation occurring at the leading-edge of the square cylinder is accompanied by three-dimensional Kelvin–Helmholtz pairings within the separated shear layer.

Consistent with circular cylinders, the quasi-periodic mode was also identified behind square cylinders using a Floquet stability analysis. It was at first named as the subharmonic or mode S by Robichaux *et al.*[119] However, Blackburn and Lopez[81] clarified that similar to circular cylinders, the intermediate mode in square cylinders has complex-conjugate pair Floquet multipliers, which can be shown as quasi-periodic standing-wave or traveling-wave type solutions. The quasi-periodic instability mode alters its rotation direction after each shedding cycle of the primary instability. Another secondary mode was also recognized in the wake of square cylinders, which has been named as mode C. This mode was reported to occur when the square cylinders are at angle of incidence and was found to be related to the

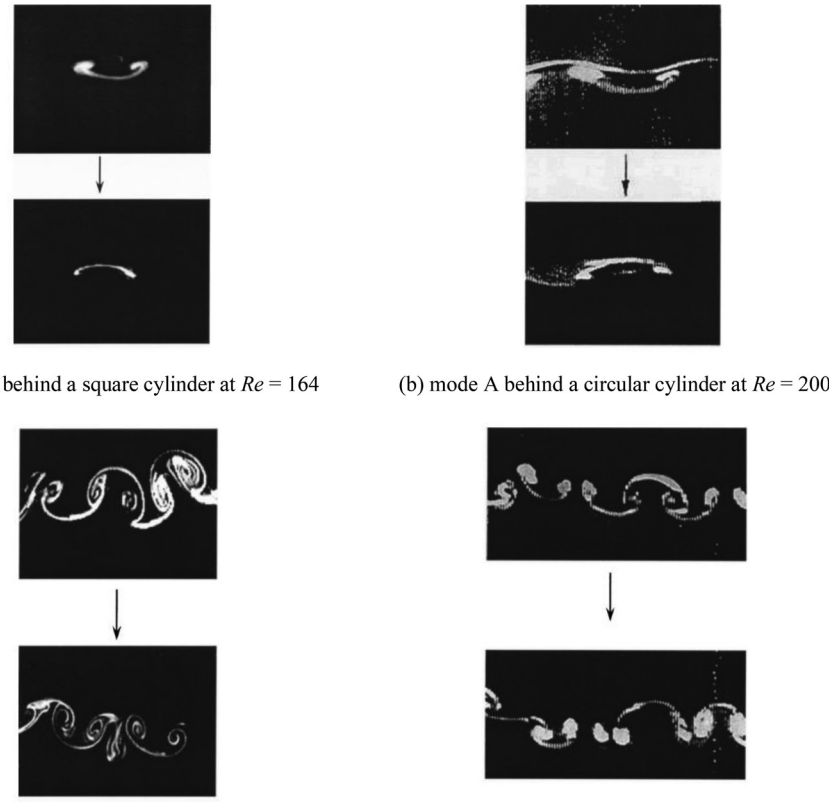

(a) mode A behind a square cylinder at $Re = 164$

(b) mode A behind a circular cylinder at $Re = 200$

(c) mode B behind a square cylinder at $Re = 220$

(d) mode B behind a circular cylinder at $Re = 280$

FIG. 20. Comparison of streamwise vortices behind square and circular cylinders (a) mode A behind a square cylinder at $Re = 164$,[114] (b) mode A behind a circular cylinder at $Re = 200$,[118] (c) mode B behind a square cylinder at $Re = 220$. Reproduced with permission from Luo *et al.*, Phys. Fluids **15**, 2549–2559 (2003). Copyright 2020 AIP Publishing LLC.[114] (d) Mode B behind a circular cylinder at $Re = 280$. Reproduced with permission from Williamson, J. Fluid Mech. **328**, 345–407 (1996). Copyright 1996 Cambridge University Press.[118] (The top and bottom pictures indicate top and bottom rows of vortices.)

breaking of the symmetry of the wake flow.[59] It was shown by Sheard *et al.*[120] that mode C takes place for angles of incidence between 12° and 26°, while mode A was observed for angles of incidence from 0° to 12° and between 26° and 45°. They also revealed that the most unstable conditions of mode C lie between angles of incidence leading to the greatest asymmetry around the wake centerline (angles of incidence between 20° and 25°). This is in agreement with the results of Yoon *et al.*[121] In addition, Sheard *et al.*[120] predicted the critical Reynolds number for onset of different stability modes behind the square cylinder along the angle of incidence, which is shown in Fig. 21(a). As can be seen, the critical Reynolds number at which mode C appears decreases with angle of incidence. Referring to Fig. 21(b), they also analyzed the spanwise wavelength of these modes along the angle of incidence. According to this figure, the spanwise wavelength of mode C is around 2D for different values of the incidence angle.

Using HWA, Saha *et al.*[123] measured the time-averaged and fluctuating streamwise and transverse components of velocity in the square cylinder wake at Reynolds numbers of 8700 and 17 625. They compared their results to those obtained from the LDV measurements of Lyn *et al.*[112] and the LES simulation of Wang.[124] They showed that results of experimental and numerical studies are in agreement for the time-averaged velocities, the streamwise velocity fluctuations, and the turbulent shear stress. However, numerical results yield comparatively higher transverse velocity fluctuations. Kurtulus *et al.*[125] confirmed the capability of time-resolved PIV as a non-intrusive technique for the measurement of unsteady aerodynamic loads for two-dimensional flows. They also showed that the periodicity of the drag coefficient during vortex shedding is less than that of the lift coefficient at Reynolds number of 4890.

As discussed in Sec. III, instability in shear layers over bluff bodies gives rise to transition and causes Kelvin–Helmholtz vortices to be formed. Last studies indicated that the ratio of Kelvin–Helmholtz frequency to von Kármán frequency is non-linearly related to the Reynolds number. A power-law scaling with an exponent of 0.5 was first proposed by Bloor,[126] while Prasad and Williamson[127] found an exponent larger than 0.5. Investigations about the nature of the shear layer transition over a square cylinder are rare. Lander *et al.*[128] assessed the scaling of the shear layers behind a square cylinder and found a power law pattern for the ratio between the shear layer frequency and the Kármán shedding frequency at Reynolds numbers between 15 000 and 75 000. They also compared the flow structure behind a square cylinder at a low Reynolds number of 16 700 and a high Reynolds number of 101 000. As can be seen in Fig. 22, the laminar vortices could be recognized in both cases, however much smaller and closer to the windward side for the higher Reynolds number case.

The aspect ratio (AR) of a cylinder is defined as the length (L) to width (W) ratio. Most classical studies adopt a large value of AR to mitigate edge effects. As AR decreases, the cylinder gradually changes to a three-dimensional body having unique wake features, which differ from that of a large AR (elongated) cylinder.[129] Dutta *et al.*[130] employed PIV to visualize the fluid flow past square cylinders for two aspect ratios of 16 and 28 at $Re = 410$. They ascertained that the separation between vortices from the opposite shear layers behind the square cylinder with $AR = 16$ is higher than that for $AR = 28$. As a result, the square cylinder with a lower aspect ratio has also a lower Strouhal number and a higher drag coefficient. Furthermore, they showed that transition to three dimensionalities occurs earlier at lower AR.

Compared to circular cylinders, square cylinders introduce the angle of incidence, which is defined as the orientation of its side face to the incoming flow, as an additional parameter profoundly affecting the flow characteristics.[131] Unlike a circular cylinder, the separation points for a square cylinder are fixed at its sharp edges.[132] Therefore, flow development has been found to be highly dependent on the incidence angle.[133] The study conducted by Dutta *et al.*[133] concerned the

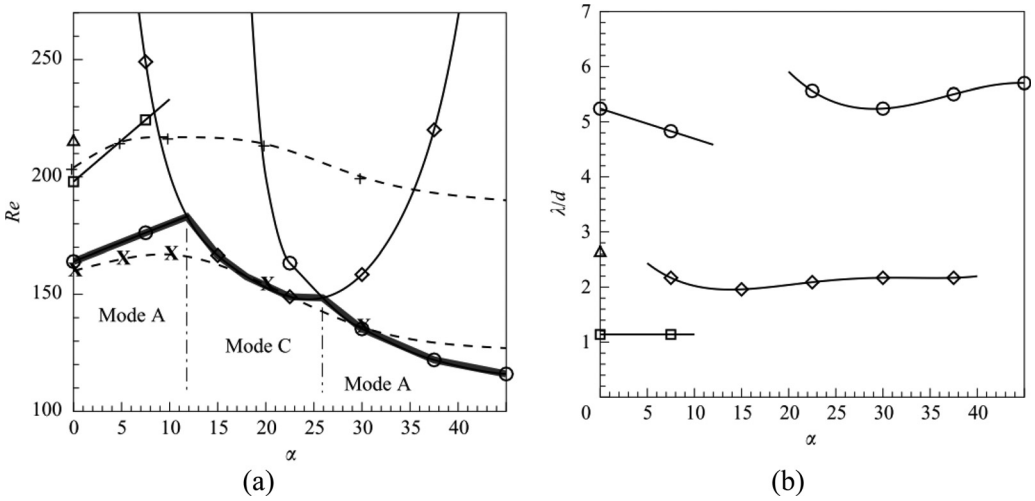

FIG. 21. Effect of incidence on flow instability modes and their characteristic wavelengths: (a) critical Reynolds number of different instability modes against angle of incidence obtained from numerical study of Sheard *et al.*[120] and experimental data of Tong *et al.*,[122] and (b) the spanwise wavelength of different instability modes against angle of incidence. [Results of Sheard *et al.*[120] are represented by solid line including mode A(○), mode B(□), mode C(◇), and quasi-periodic mode (Δ)]. Data of Tong *et al.*[122] are shown by dashed line including mode A (×) and mode B (+). Reproduced with permission from Sheard *et al.*, J. Fluid Mech. **630**, 43–69 (2009). Copyright 2009 Cambridge University Press.[120]

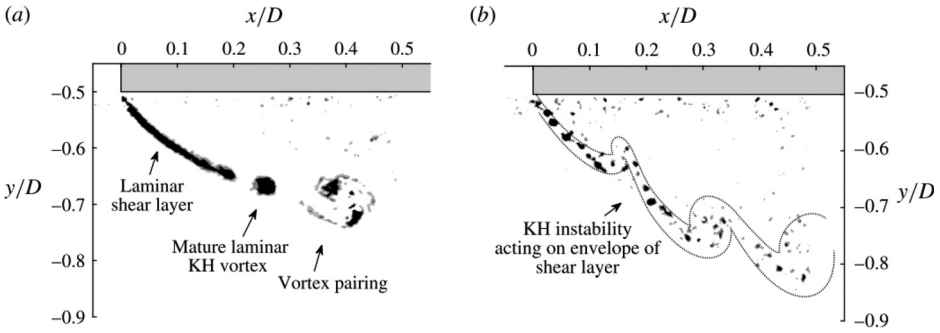

FIG. 22. Instantaneous Q criterion for (a) $Re = 16\,700$ and (b) $Re = 101\,000$ behind the square cylinder. Reproduced with permission from Lander *et al.*, J. Fluid Mech. **849**, 1096–1119 (2018). Copyright 2018 Cambridge University Press.[128]

effects of the incidence angle, ranging from 0° (face oriented) to 60° on the wake properties of a square cylinder. They found that the wake size and the Strouhal number increase for the inclined cylinders, while the drag coefficient decreases. According to Fig. 23(a), Oudheusden *et al.*[134] pointed out that for low incidence angle (up to 10°), the rear and side recirculation regions merge at the upper side of the cylinder. For the lower side, however, the side recirculation region shrinks, and the mean flow reattaches for the angle of incidence between 10° and 15°. As shown in Fig. 23(b), Huang *et al.*[132] divided the flow behind the square cylinder into three regimes of subcritical, supercritical, and wedge for Reynolds numbers between 5000 and 120 000. They explained that for angles of incidence between 0° and 15°, the flow is subcritical and the boundary layer is separated from the leading-edge of upper and lower sides and never reattached. In contrast to Oudheusden *et al.*,[134] they pointed out that small dual-ring bubbles formed close to the leading-edge of the upper and lower sides. This discrepancy between the outcomes of Huang *et al.*[132] and Oudheusden *et al.*[134] could be ascribed to their different experimental setups. In the supercritical regime, where the angle of incidence is between 15° and 45°, the separated boundary layer of the lower side is reattached to the surface, leading to the formation of a recirculation bubble. However, the separated boundary layer on the upper side is never reattached. Instead, a large recirculation bubble is created, which is stretched to the rear part of the surface. For the angle of incidence of 45°, a symmetric wedge flow is seen on the leading-edge surfaces.

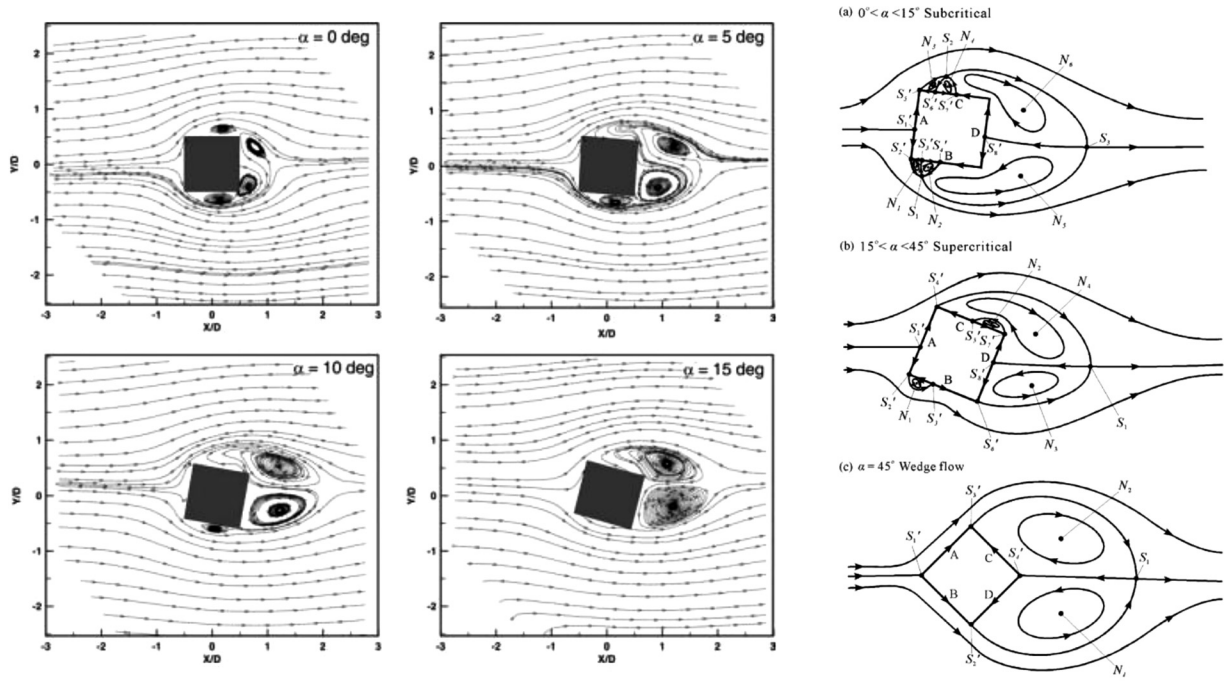

FIG. 23. Fluid flow behind an inclined square cylinder with the angle of incidence (a) mean flow streamline topology. Reproduced with permission from Oudheusden *et al.*, Exp. Fluids **39**, 86–98 (2005). Copyright 2005 Springer Nature.[134] (b) Conceptual topological flow patterns. Reproduced with permission from Huang *et al.*, J. Fluids Struct. **26**, 406–429 (2010). Copyright 2010 Elsevier.[132]

Similar to Huang *et al.*,[132] Yen and Yang[135] classified the flow behind a square cylinder into three regimes of leading-edge separation, separation bubble, and attached flow based on the angle of incidence (Fig. 24). They highlighted that the flow topology in the leading-edge separation regime is similar to what Oudheusden *et al.*[134] previously showed. It was also found that the minimum drag and lift are experienced at incidence angles of 12° and 13°, respectively. van Oudheusden *et al.*[131] showed that the intense fluctuation regions are moved downstream with the increment of the angle of incidence.

Lou *et al.*[136] analyzed the effects of the yaw angle ranging from zero to 45° at a $Re = 3600$ on wake characteristics behind a square cylinder and observed that as the yaw angle increases, the rms components of the velocity, and the spanwise and transverse vortices, decrease. This considerable reduction of velocity fluctuations on the centerline leads to a reduction of the vortex strength. This paper also compared the flow properties between yawed square and circular cylinders and found that the square cylinder experiences a faster decay of the vortex strength with the yaw angle than the circular cylinder because of a stronger three-dimensionality effect in the former.

Some research has also been conducted on the specific effect of edge rounding for square cylinders. Carassale *et al.*[137] revealed that the flow reattaches at a smaller critical angle around square cylinders when their corners have been rounded. Furthermore, they stated that the flow reattaches on the lateral surfaces even at zero incidence by rounding the corners. van Hinsberg *et al.*[138] clarified that the maximum drag coefficient, the rms values of lift fluctuations, and the critical Reynolds number all reduce by increasing corner roundness (viz., edge radius of curvature). Furthermore, decreasing the angle of incidence to a negative value causes the drag force, the Strouhal number, and the base pressure to increase. In another research study, van Hinsberg *et al.*[139] proved that higher vortex shedding frequency at all flow regimes is yielded with a larger corner radius. Hu and Zhou[140] evaluated the flow characteristics around a square cylinder with some corners rounded. They concluded that asymmetry in the cross section of the cylinder results in the movement of the wake centerline toward the sharp corner side. However, the wake remains symmetric about the shifted centerline.

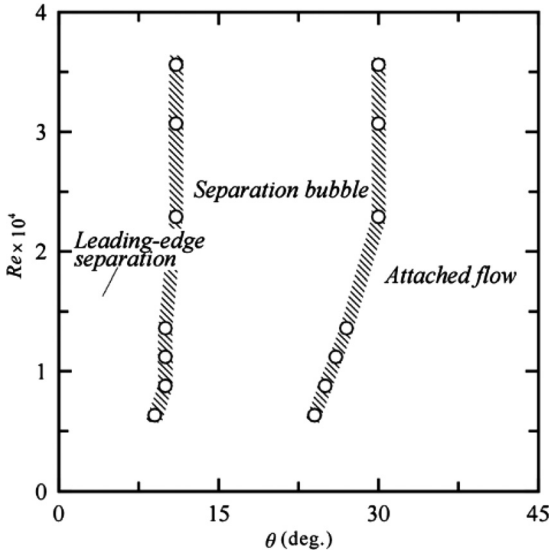

FIG. 24. Flow regimes behind a square cylinder based on the angle of incidence. Reproduced with permission from Yen and Yang, J. Wind Eng. Ind. Aerodyn. **99**, 868–878 (2011). Copyright 2011 Elsevier.[135]

2. Rectangular cylinders

Side ratio (SR) of a rectangular cylinder is defined as the ratio of its width (W) to its height (H). Two flow features can be characterized for a rectangular cylinder with a sufficiently high side ratio: (a) leading-edge flow separation–reattachment, and (b) vortex shedding at the trailing-edge.[141] Nakagawa *et al.*[142] highlighted that for low side ratios ($W/H = 0.5, 1$), the separated shear layers at the leading-edges penetrate into the rear side of cylinders, whereas at higher side ratios ($W/H = 3$), they reattach onto the side walls. The fluid flow behind an inclined flat plate ($SR \ll 1$) at a high Reynolds number of 200 000 was investigated by Deri *et al.*[143] using tomographic PIV. They identified two asymmetric recirculation regions behind the plate with incidence of 10° and showed that the streamwise and spanwise components of the rms velocity are formed by a two-lobe structure, while the transverse component indicates a single-lobe structure. An investigation of the separated shear layer behind three rectangular cylinders with side ratios of 1, 3, and 5 at Reynolds numbers ranging from 13 400 to 118 000 was performed by Moore *et al.*[144] As shown in Fig. 25, for cylinders with side ratios of 1 and 3, a small negative vorticity region is formed just upstream of the trailing-edge. However, for the most elongated case, $SR = 5$, no such region exists. On the other hand, the flow is reattached to the surface of the most elongated case, while other cases have no such reattachment point and the separating streamlines continue in the wake. Therefore, it seems that the shear layer bounding a separation bubble is less affected by the wake flow than the case without reattachment. Gu *et al.*[145] studied the effects of the side ratio and chamfered corners on the aerodynamic properties of rectangular cylinders at a Reynolds number of 340 000 and showed the flow reattachment on the lateral surfaces of the rectangular cylinder with side ratios of 3 and 4 and on the lateral surfaces of the rectangular cylinder with a side ratio of 2 with chamfered corners. However, for the square cylinder and the non-chamfered rectangular cylinder with a side ratio of 2, the separated flow does not reattach to the lateral surfaces. Xu *et al.*[146] showed that the drag coefficient of the rectangular cylinder could be reduced by up to 23% by corner modification of the leading-edge at a Reynolds number of 2240.

3. D-shaped cylinders

This kind of cylinders is classified based on their leading-edge and trailing-edge shapes. They usually consist of a central rectangular cylinder and semi-circular, semi-elliptical, or triangular leading-edge and/or trailing-edge. It is worth mentioning that D-shaped cylinders are employed near the root of large wind turbine blades and are responsible for reducing the weight and improving the structural performance.[65] Taylor *et al.*[147] compared the flow topology behind two D-shaped cylinders with semi-circular and triangular leading- and trailing-edge, and a side ratio of 7 to a rectangular cylinder at a Reynolds number of 30 000. They proved that in contrast to the cylinder with semi-circular leading- and trailing-edge, the rectangular cylinder and the cylinder with triangular edge undergo a leading-edge separation–reattachment. This separation–reattachment process at the

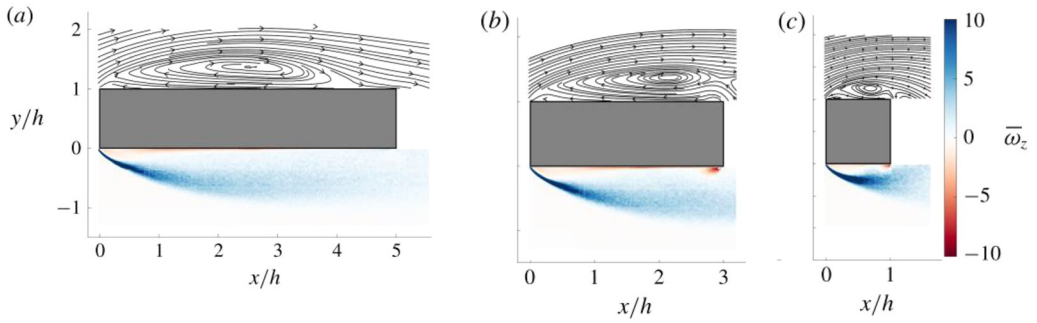

FIG. 25. Time-averaged streamlines (top) and vorticity contours (bottom) (a) $SR = 5$, (b) $SR = 3$, and (c) $SR = 1$. Reproduced with permission from Moore *et al.*, J. Fluid Mech. **875**, 543–575 (2019). Copyright 2019 Cambridge University Press.[144]

leading-edge of the cylinder with triangular edge is not as strong as that in the rectangular cylinder.

The wake instability behind a D-shaped cylinder with a semi-elliptical leading-edge and a side ratio of 12.5 was studied by Naghib-Lahouti *et al.*[148] for $2000 \leq Re \leq 50\,000$. They found that similar to square and circular cylinders, the structure and the spanwise wavelength of the small-scale secondary vortices, demonstrated in Fig. 26, are less affected by the boundary layer state upstream of the separation point. Results obtained by Naghib-Lahouti *et al.*[148] are in agreement with Ryan *et al.*[149] who found the mode B secondary instability with wavelengths ranging from 2.0 to 2.5 of the cylinder's height. However, Gibeau *et al.*[65] believed that the POD-based analysis approach implemented in Ref. 148 misrepresents the streamwise vortices structure. They found the same mode B secondary instability as the circular cylinder wake, however, with a spanwise length scale of 0.7 to 0.8 of the cylinder's height for $W/H = 46.5$ at Reynolds numbers of 3500, 5200, and 7000. Nevertheless, they suspected that this discrepancy might be ascribed to the difference of the side ratios.

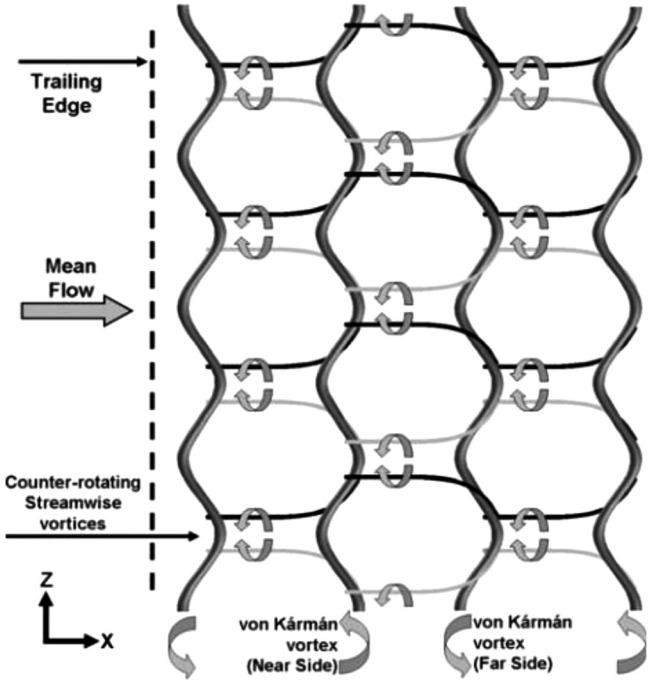

FIG. 26. Vorticity structure of the secondary vortices behind a D-shaped cylinder with a semi-elliptical leading-edge. Reproduced with permission from Naghib-Lahouti *et al.*, Exp. Fluids **52**, 1547–1566 (2012). Copyright 2014 Springer Nature.[151]

Later, Gibeau and Ghaemi[59] focused on a D-shaped cylinder with a semi-elliptical leading-edge and a side ratio of 12.5, reproducing the experimental conditions of Naghib-Lahouti *et al.*[148] coming to nearly the same results of the latter for the formation length, the frequency of vortex shedding, and the wavelength of the spanwise or Kármán vortices at Reynolds numbers ranging from 2600 to 25 800. However, the mean values for the spanwise length scale of the streamwise vortices ranged from 0.77 to 0.96 of the cylinder's height. Therefore, they could not confirm a clear relation between the spanwise scaling of the mode B in the wake of a blunt trailing-edge and the side ratio. However, they claimed that the side ratio of a bluff body may not affect the formation of the streamwise vortices. As a conclusion, it seems that the flow physics in the range of the secondary or streamwise vortices behind the elongated bluff bodies are not well understood and more investigations are required. Shu and Li[150] studied the flow characteristics around a D-shaped cylinder with different triangulated leading-edges and clarified that the distribution of the surface pressure is significantly dependent on the apex angle of the leading-edge. To be more specific, the mean reattachment length, the magnitudes of rms and the peak suction pressure coefficients all increase with the apex angle.

4. Trapezoidal, triangular, and polygonal cylinders

Investigations of cylinders with a trapezoidal, triangular, or polygonal cross section are even more rarely found in the literature. Using smoke-wire visualization technique, Wu *et al.*[152] focused on the fluid flow behind a trapezoidal cylinder for $1800 < Re < 27\,000$ and identified two distinct modes, namely, modes L and S. As can be seen in Fig. 27, mode L is characterized with a long formation region while three-dimensionality effect of the vortex shedding is more intense in mode S where the formation length is smaller. Xu *et al.*[146] explained that the strength and the vortex scale reduce when the cross section of a cylinder changes from the rectangular to trapezoidal. Hence, the fluctuation intensity of the wake is diminished and the wake width is narrowed, while the recirculation region is elongated.

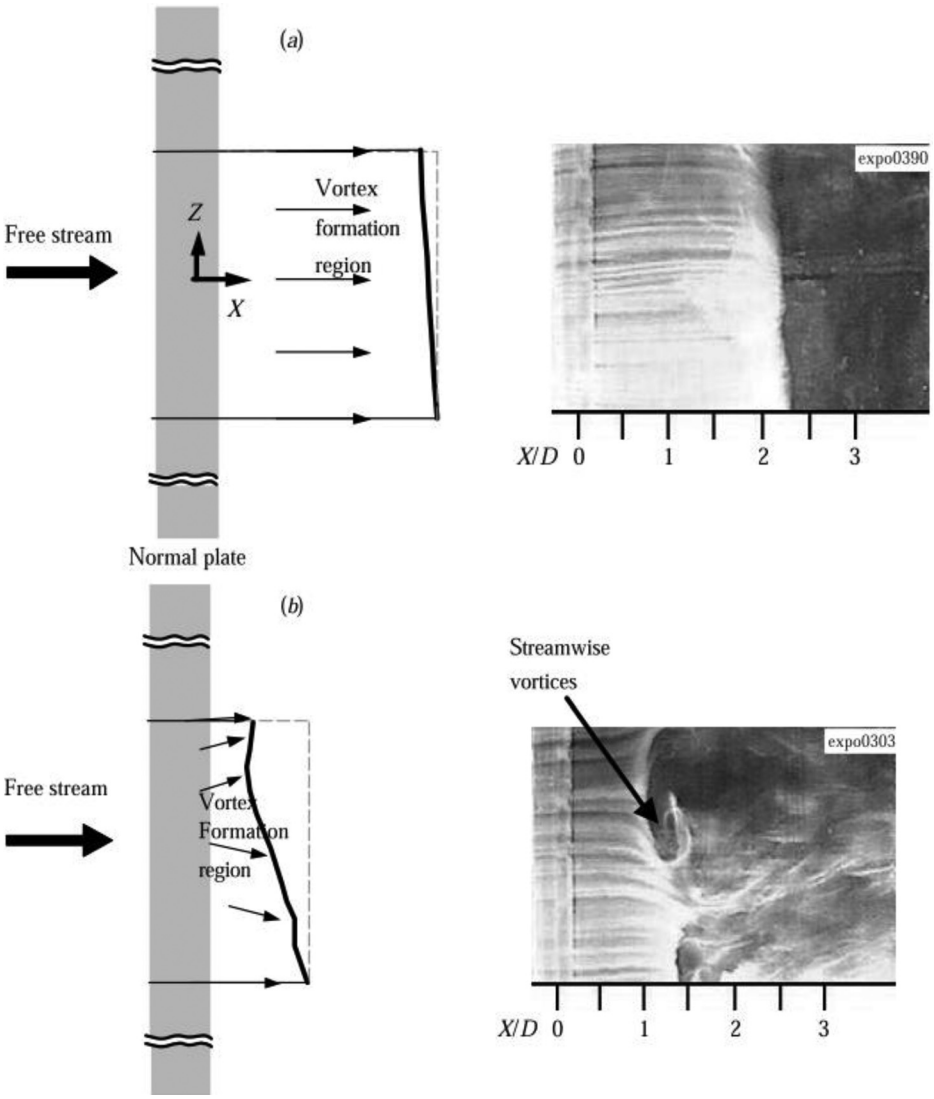

FIG. 27. Vortex formation modes behind a trapezoidal cylinder (a) mode L and (b) mode S. Reproduced with permission from Wu *et al.*, J. Fluid Mech. **526**, 117–146 (2005). Copyright 2005 Cambridge University Press.[152]

Agrwal *et al.*[153] focused on triangular cylinders and studied the effects of the apex angle on the flow structure and aerodynamic characteristics. Results indicated that the drag coefficient increases with the apex angle, while the Strouhal number is reduced. That is to say, the minimum drag coefficient and the maximum Strouhal number are obtained at the apex angle of 30°. These findings were supported by several measurements conducted with PIV, HWA, and corroborated with flow visualization methods. As shown in Fig. 28, when the apex angle is increased, a larger vortex structure and recirculation zone is created behind the cylinder, resulting in a higher wake width and consequently a higher drag coefficient. Mode C, which was previously detected behind the square cylinder wake at inclination, was also identified by Ng *et al.*[154] in the wake of triangular cross-sectional cylinders using a Floquet stability analysis. They reported that mode C becomes the primary instability for transition to three dimensionalities for angles of incidence between 34.6° and 55.4°, and spanwise wavelengths from 1.6 to 1.8. Sun *et al.*[155] investigated the near wake and vortex characteristics behind an equilateral triangular cylinder using high speed PIV for Reynolds numbers ranging from 10 700 to 17 700. Results indicated that the streamwise velocity of the vortex core center downstream the vortex formation is about 0.8 of the freestream velocity. This value is larger than that behind a circular cylinder, which is about 0.7 at the same Reynolds number.

Polygonal cylinders have gained a considerable interest due to their applicability in various engineering fields, such as fluid machineries, ocean engineering, architecture, and power generation systems. Understanding the flow characteristics behind polygonal cylinders is of importance due to the remarkable effects of the integer side number (N) on vortex formation, flow separation, and vortex convection in the wake zone.[156] Using three-component force measurement transducer, HWA, PIV, and flow visualization technique, Xu *et al.*[157] measured the flow characteristics around polygonal cylinders for two principal

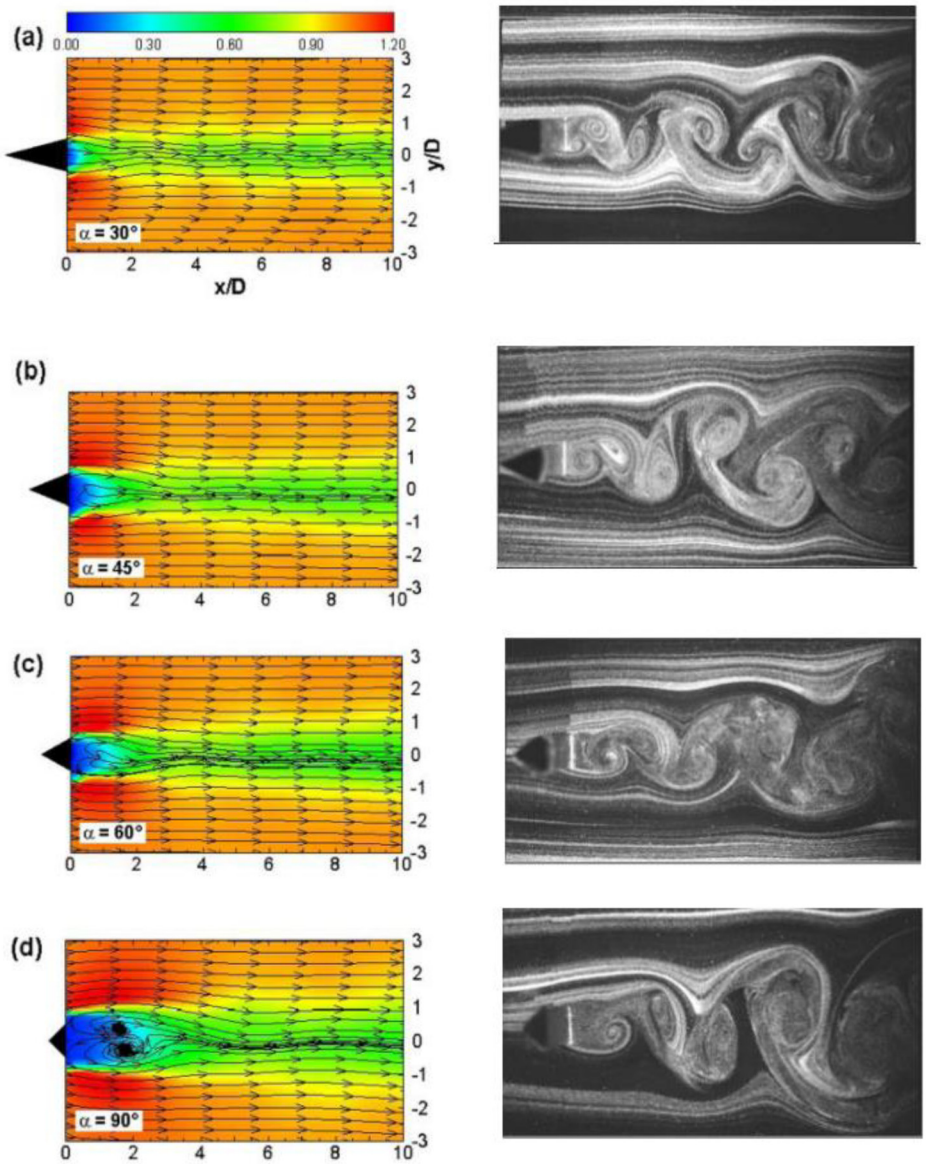

FIG. 28. Time-averaged velocity magnitude with stream traces (left) and instantaneous flow visualization images (right) in the wake of a triangular prism (a) apex angle = 30°, (b) apex angle = 45°, (c) apex angle = 60°, and (d) apex angle = 90°. Figure adapted with permission from Agrwal *et al.*, Exp. Therm. Fluid Sci. **72**, 97–111 (2016). Copyright 2016 Elsevier.[153]

orientations, with a flat surface or a corner facing normally to the free-stream. According to Fig. 29, the flow separation point is fixed at the corner at the maximum width for $N \leq 8$, while the drag coefficient and the Strouhal number are almost not related to the Reynolds number. Cylinders with $N = 12$ and $N = 16$, however, experience transition at $Re = 24\,000$ and $Re = 34\,000$, respectively. As a result, their drag coefficients decrease significantly, while their Strouhal numbers exhibit a considerable increase. In subsequent studies, Wang *et al.*[158] unveiled that the Strouhal number, the drag, and fluctuating lift coefficients are in a close relation with the vortex formation length and the wake width. Wang *et al.*[156] focused more on the wake features and the vortex evolution. They proved that the vortex circulation reaches its maximum value at the vortex formation length and then undergoes a two-step reduction. The first step is almost independent of the polygon side number and is greatly under the influence of the vorticity diffusion and viscous dissipation. However, the second step is characterized with a faster decay rate and is a function of the cylinder's geometry. Table I summarizes experimental studies about non-circular cylinders discussed in this section. It should be mentioned that the star symbol (*) in this table indicates the properties estimated by the authors of this review on the basis of the information provided in the surveyed articles.

B. Non-uniformity in spanwise direction

This section deals with the effects of shape variations in the spanwise direction on the flow characteristics and topology.

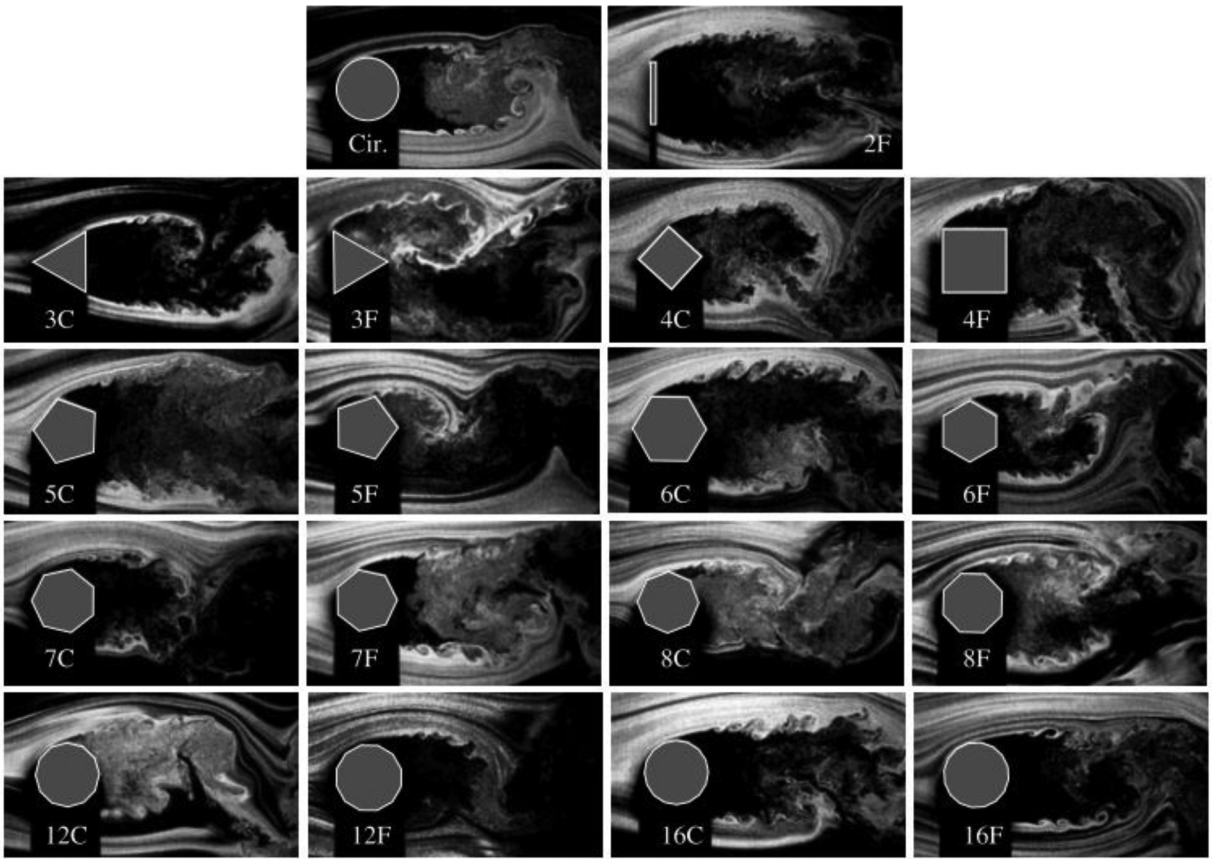

FIG. 29. Flow visualization behind polygonal cylinders at different orientations. Reproduced with permission from Xu *et al.*, J. Fluid Mech. **812**, 251–278 (2017). Copyright 2017 Cambridge University Press.[157]

Non-uniformity in spanwise direction is mainly used as a technique to manipulate the vortex shedding around cylinders. Herein, the focus is given to two types of common spanwise-varied cylinders, namely, sinusoidal or wavy cylinders and dual-step cylinders. Tapering is another type of spanwise shape variation but is not discussed here. Interested readers are referred to Refs. 159 and 160.

1. Sinusoidal or wavy cylinders

Sinusoidal or wavy cylinders have recently attracted a great deal of attention not only for the role wavy profiles play in controlling the flow but also in the context of bio-inspired engineering. For example, seals look for their underwater prey through their wavy-cylinder-like vibrissae. As demonstrated in Fig. 30, the geometry of a sinusoidal cylinder in spanwise direction is obtained by changing the local diameter through the saddle and nodal points using the following equation: $D = D_m + 2A \cos(2\pi z/\lambda)$. In this equation, D_m is the mean diameter, A the amplitude or the half distance between the lowest diameter (saddle point) and the highest diameter (nodal point), and λ the wavelength, which is the distance between two consecutive saddle and nodal points.

Although the geometry of sinusoidal cylinders is axisymmetric, the separated flow structures appear to be distinctly asymmetric near the nodal points.[162] Saddle and nodal points play a major role in changing the boundary layer separation angle, which was determined to be about 81°. Ahmed *et al.*[163] pointed out that the separation angle is advanced to approximately 70°–80° behind saddle points while delayed to 90°–100° behind nodal points. As depicted in Fig. 31, this behavior could be ascribed to the near-wake region, which is wider behind the saddle points.[164] Furthermore, in contrast to a circular cylinder, the wake pattern behind a wavy cylinder curves up like a balloon.[165]

Based on the wavelength and amplitude, different flow regimes can be formed behind wavy cylinders. Although the main focus of this paper is on experimental research studies, the numerical work conducted by Lam and Lin[166] is recalled here to systematically discuss different flow regimes and aerodynamic characteristics behind wavy cylinders at different values of wavelength and amplitude. As demonstrated in Fig. 32, they classified the wavy cylinders into three different wavelength regimes of $1 \leq \lambda/D_m < 2.5$ (regime I), $2.5 \leq \lambda/D_m < 6$ (regime II), and $6 \leq \lambda/D_m \leq 10$ (regime III) each of which can have different flow topologies of A, B, and C. While the flow structure past a wavy cylinder is similar to that past a circular cylinder in the flow

TABLE I. A summary of experimental studies about non-circular cylinders.

Paper	*Re*	Bluff body	SR (*W*/*H*)	AR (*L*/*W*)	TI (%)	BR (%)	Methodology
Gibeau and Ghaemi[59]	2600–25 800	Rectangular cylinder with semi-elliptical leading-edge (L1.2 × W0.163 × H0.013 m^3)	12.5	7.36	≤0.5	0.5	Closed-loop wind tunnel (L11 × H1.2 × W2.4 m^3) •2C-PIV •Stereo-PIV •HWA
Gibeau *et al.*[65]	3500 5200 7000	Rectangular cylinder with semi-elliptical leading-edge (L1.2 × W0.6 × H0.012 9 m^3)	46.5	2*	<0.4	0.5	Wind tunnel (H1.2 × W2.4 m^2) •2C-PIV • Stereoscopic PIV
Lyn *et al.*[112]	21 400	Square cylinder (W0.04 × H0.04 m^2)	1	9.75	2	7	Closed water channel (0.39 × 0.56 m^2) •LDV
Durão *et al.*[113]	14 000	Square cylinder (W0.02 × H0.02 m^2)	1	6	6	13	Water channel (0.12 × 0.156 m^2) •LDV
Luo *et al.*[114]	100–250	Square cylinder (L0.4 × W0.007 9 × H 0.007 9 m^3) Square cylinder (W0.001 2 × H 0.001 2 m^2)	1	44.3 225	<0.35 ≈1	1.56*	Recirculating water channel (L1.83 × H0.45 × W0.45 m^3) •FV [dye and laser-induced fluorescence (LIF)] Open-loop wind tunnel (H0.34 × W0.34 m^2) •HWA (single-wire)
Dobre and Hangan[115]	22 000	Square cylinder (H0.03 × W0.03 m^2)	1	40	≈0.17	≈2	Close-return wind tunnel •Simultaneous multi-point HWA
Yu *et al.*[116]	2150	Square cylinder (L0.15* × W0.015 × H0.015 m^3)	1	10*	···	7.5*	Low-speed water tunnel (L1.05 × H0.2 × W0.15 m^3) •Time-resolved PIV
Minguez *et al.*[117]	20 000–22 000	Square cylinder (W0.1 × H0.1 m^2)	1	50	<0.8	5	Looped-wind tunnel (H2 × W2 m^2) •Two-component LDV
Saha *et al.*[123]	8700 17 625	Square cylinder (L0.4 × W0.025 × H0.025 m^3)	1	16	0.05	6.25	Open-circuit wind tunnel (L3 × H0.4 × W0.4 m^3) •HWA
Kurtulus *et al.*[125]	4900	Square cylinder (W0.03 × H0.03 m^2)	1	17	<0.5	-	Closed-loop wind tunnel •Time-resolved PIV
Lander *et al.*[128]	15 000–75 000	Square cylinder (L0.508 × W0.076 2 × H0.076 2 m^3)	1	6.67	<0.3	9.1	Blow-down, open return wind tunnel (L5 × H0.8 × W0.8 m^3) •2C-PIV and HWA •Time-averaged surface pressure measurements
Zhao *et al.*[129]	34 000	Square cylinder (L0.4, 0.2 × W0.04 × H0.04 m^3)	1	5, 10	0.5, 5, 12.1	3.95	Open-circuited low-speed wind tunnel (L1 × H0.45 × W0.45 m^3) •2C PIV •Pressure scanners

TABLE I. (*Continued.*)

Paper	*Re*	Bluff body	SR (*W*/*H*)	AR (*L*/*W*)	TI (%)	BR (%)	Methodology
Dutta *et al.*[130]	410	Square cylinder (W0.003 × H 0.003 4 m^2)	0.88*	16 28	<0.05	3	Vertical test cell (L2 × H0.095 × W0.048 m^3) •HWA and PIV •Flow visualization
van Oudheusden *et al.*[131]	4000 10 000 20 000	Square cylinder (L0.35 × W0.03 × H 0.03 m^3)	1	11.7	0.1	7.5	Open-circuit wind tunnel (H0.4 × W0.4 m^2) •PIV
Huang *et al.*[132]	5000–120 000	Square cylinder (L0.6 × W0.06 × H0.06 m^3)	1	10	0.5	10–14	Closed-return wind tunnel (L1.2 × H0.6 × W0.6 m^3) •HWA (single-wire) •FV (surface-oil) •FV (smoke-wire)
Dutta *et al.*[133]	1340 4990 9980	Square cylinder (W0.025 × H 0.025 m^2)	1	15	<0.05	6.25*	Open-circuit wind tunnel (L2 × H0.4 × W0.4 m^3) •HWA (X-wire)
Oudheusden *et al.*[134]	4000 10 000 20 000	Square cylinder (L0.35 × W0.03 × H 0.03 m^3)	1	11.7*	0.1	7	Open-circuit wind tunnel (H0.4 × W0.4 m^2) •PIV
Yen and Yang[135]	4000–36 000	Square cylinder (L0.5 × W0.02 × H0.02 m^3)	1	25	<0.4	4	Open-loop wind tunnel (L1.2 × H0.5 × W0.5 m^3) •FV (smoke-wire technique) •PIV •Pressure transducer
Lou *et al.*[136]	3600	Square cylinder (L0.38 × W0.012 7 × H0.012 7 m^3)	1	29.9*	···	4.8*	Blower type wind tunnel (L2 × H0.25 × W0.38 m^3) •6-component loadcell •HWA (single wire)
Carassale *et al.*[137]	17 000–230 000	Square cylinder (L0.5 × W0.05–0.15 m^2)	1	3.3* 10*	≈0.2 ≈5	1.1*	Closed-circuit wind tunnel (1.64 × 1.35 m^2) •Force balance •Pressure scanners
van Hinsberg *et al.*[138]	80 000–12 200 000	Square cylinder (L0.6 × W0.06 × H0.06 m^3)	1	10	<0.8	10–14	Closed-circuit wind tunnel (L1 × H0.6 × W0.6 m^3) •Piezoelectric balances •Static wall pressure sensors •FV (surface-oil flow)
van Hinsberg *et al.*[139]							
Hu and Zhou[140]	2600 6000 8500	Square cylinder (L0.6 × W0.012 7 × H0.012 7 m^3)	1	47	<0.4	2.1	Closed-circuit wind tunnel (L2.4 × H0.6 × W0.6 m^3) •Piezoelectric load cell •LDV (two-component) •PIV

TABLE I. (*Continued.*)

Paper	*Re*	Bluff body	SR (*W*/*H*)	AR (*L*/*W*)	TI (%)	BR (%)	Methodology
Nakagawa *et al.*[142]	3000	Square and rectangular cylinder (L0.35 × H0.01 m^2)	0.5 1 2 3	11.7* 17.5* 35 70*	6	20	Closed water channel (L0.5 × H0.05 × W0.35 m^3) •LDV •Flow visualization (FV) (hydrogen bubble technique)
Deri *et al.*[143]	200 000	Flat plate (rectangular cylinder) (L0.6 × W0.3 × H0.015 m^3)	20	2	<1	7.4	Closed loop wind tunnel (L2 × H0.7 × W0.6 m^3) •Tomographic PIV
Moore *et al.*[144]	13 400–118 000	Square and rectangular cylinders (L0.508 × W0.050 8 × H0.050 8 m^3)	1 3 5	10*	<0.25	0.4* 1.2* 2*	Blow-down wind tunnel (L5 × H0.8 × W0.8 m^3) •Two single HWA •PIV
Gu *et al.*[145]	340 000	Rectangular cylinders (L1.5 × H0.2 m^2)	1 2 3 4	1.88* 2.5* 3.75* 7.5	≈0.26	4	Closed-circuit wind tunnel (H2.5 × W3 m^2) •Pressure taps
Xu *et al.*[146]	2240	Rectangular and trapezoidal cylinders (L0.48 × W0.005 × H0.04 m^3)	0.125*	96*	<0.8	5.4*	Water channel (L3 × H0.6 × W0.6 m^3) •2D time-resolved PIV
Taylor *et al.*[147]	30 000	Rectangular cylinder Rectangular cylinders with triangular and semi-circular ends (W0.175 × H0.025 m^2)	7	18	≈0.8	5.4	Open-return wind tunnel (L1.5 × H0.46 × W0.46 m^3) •PIV •Pressure taps
Naghib-Lahouti *et al.*[148]	2000–50 000	Rectangular cylinder with semi-elliptical leading-edge (L0.685 8 × W0.317 5 × H0.025 4 m^3)	12.5	2.16*	0.05	3.2	Closed-circuit wind tunnel (L5 × H0.8 × W1.2 m^3) •HWA and PIV
Shu and Li[150]	18 000–31 000	Rectangular cylinder Rectangular cylinder with triangular leading-edge (L1 × W0.75 × H0.05 m^3)	15	1.33*	1.71–30.8	0.59	Return-flow wind tunnel (L20 × H2 × W4.2 m^3) •Pressure taps
Wu *et al.*[152]	1800–27 000	Trapezoidal (W0.013 × H0.032 m^2)	0.41*	11.57*	≈0.7	21	Closed-return wind tunnel (H0.15 × W0.15 m^2) •HWA (single wire) •FV (smoke-wire)
Agrwal *et al.*[153]	520	Triangular cylinder (L0.16 × W0.006 × H0.006 m^3)	1	26.7	<0.08	6	Open-circuit wind tunnel (L1.5 × 0.16 × 0.1 m^3) •PIV •HWA
Sun *et al.*[155]	10 700–17 700	Triangular cylinder (L0.076 × W0.0096 2 × H0.0096 2 m^3)	1	7.9	≈2	16	Wind tunnel (L0.6 × W0.076 × H0.06 m^3) •High-repetition rate PIV

TABLE I. (*Continued.*)

Paper	*Re*	Bluff body	SR (*W*/*H*)	AR (*L*/*W*)	TI (%)	BR (%)	Methodology
Wang *et al.*[156]	16 000	Polygonal cylinders (L0.42 × D0.025 m^2)	1	16.8	<0.5	5	Open-circuit wind tunnel (L2 × H0.5 × W0.5 m^3) •2-C PIV
Xu *et al.*[157]	10 000–100 000	Polygonal cylinders (L0.46 × D.05–0.025 m^2)	1	16.8	<0.5	≈5	Open-loop wind tunnel (L2 × H0.5 × W0.5 m^3) •3-component force meas. •FV (smoke flow) •PIV and HWA
Wang *et al.*[158]	10 000–60 000	Polygonal cylinder (L0.42 × D.025 m^2)	1	16.8	<0.5	5	Open-circuit wind tunnel (L2 × H0.5 × W0.5 m^3) •2C-PIV •Load cell

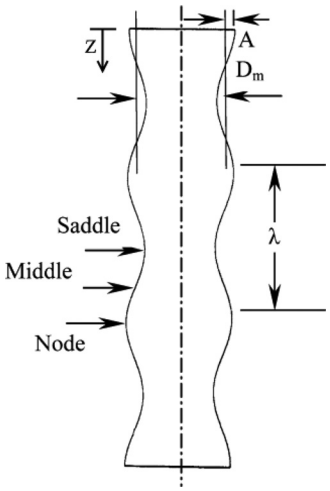

FIG. 30. Geometry of a sinusoidal cylinder. Figure adapted with permission from Zhang *et al.*, Exp. Fluids **38**, 824–832 (2005). Copyright 2005 Springer Nature.[161]

pattern A, the vortex formation length and three-dimensional wake vortex distortion increases in flow pattern B. For flow pattern C, no vortex shedding is seen and the flow structure resembles a steady regime. In addition, both the drag coefficient and the fluctuating lift coefficient experience two troughs at wavelengths of 2.5 and 6 in which transition of the flow pattern to regimes II and III occur, respectively. Regarding the wake width, nodal and saddle planes showed different behaviors with wavelength and amplitude. While the wake width increased and decreased behind saddle and nodal planes, respectively, for flow patterns A or B of regimes I and II, it decreased and increased behind saddle and nodal planes, respectively, for flow patterns A or B of the regime III. In comparison with circular cylinders, the flow separation angle alters in the spanwise direction of all wavy cylinders, resulting in development of three-dimensional vortex structures.

With regard to the spanwise velocity in the outside zone of the separated shear layer, Wang *et al.*[167] found that the flow direction is from the saddle plane toward the nodal plane, leading to a spanwise movement of shed shear layers originating from the points near the saddles. The shear layers are then contracted around the nodal points, resulting in a three-dimensional vortex structure. They also showed that the vortex formation length in a wavy cylinder is larger than that in a circular cylinder for the Reynolds numbers from 3000 to 9000. This point was also confirmed by Lee and Nguyen.[168] This feature leads to lower drag and fluctuating lift coefficients because the drag coefficient is generally considered to be related to the curvature of the separated shear layer, and a longer formation length results in a reduction in the streamline curvature and therefore a lower pressure drop across the shear layer.

According to Fig. 33, Wang *et al.*[164] revealed that the formation length is larger in the wake of the saddle plane than in that of the nodal plane. A rib-like structure was observed by Wang *et al.*[164] at $t/T = 1.25$ particularly in the saddle planes, which has a tendency to join neighboring vortices. This structure subsequently causes the vortex filaments to be distorted until they breakdown in the near-wake region. It should be mentioned that distortions of the vortex filaments

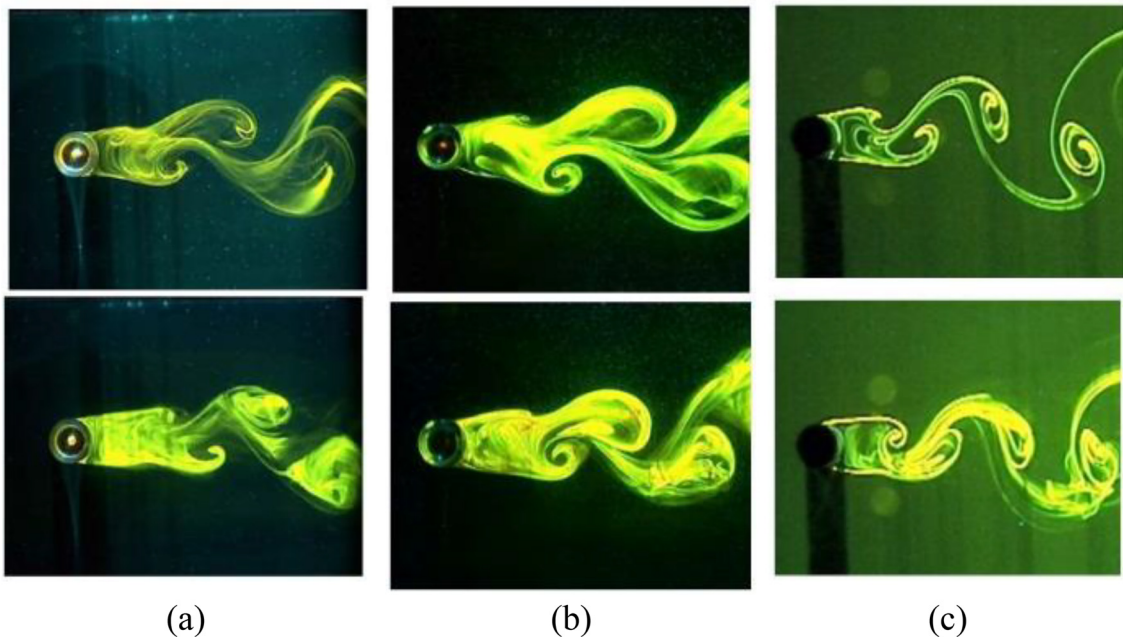

FIG. 31. Flow pattern in the near-wake of wavy and circular cylinders at $Re = 200$ (top) and 400 (bottom) (a) nodal plane, (b) saddle plane, and (c) circular cylinder. Reproduced with permission from Wang *et al.*, J. Visualization **8**, 49–56 (2005). Copyright 2005 Springer Nature.[164]

had been previously reported by Gerrard[67] behind a circular cylinder as a fingerlike structure. Zhang *et al.*[161] clarified that the counter-rotating streamwise vortices created near the nodal points interact with the large-scale spanwise vortices. These streamwise vortices, which are different to modes A and B behind the circular cylinder, impede the regular vortex shedding, and suppress the formation of the large-scale spanwise vortices. As a consequence, the wake width is reduced behind the nodal plane. They also found that the turbulent kinetic energy behind the saddle plane is lower than that behind the nodal plane. Therefore, the turbulence kinetic energy in the near-wake of a sinusoidal cylinder is lower than in that of a circular cylinder predominantly owing to the reduction of the turbulent kinetic energy in the saddle plane.

Similar to Wang *et al.*,[167] Lee and Nguyen[168] emphasized that the flow is expanded laterally behind the saddle plane as it goes downstream. This behavior was attributed to the entrainment of a large

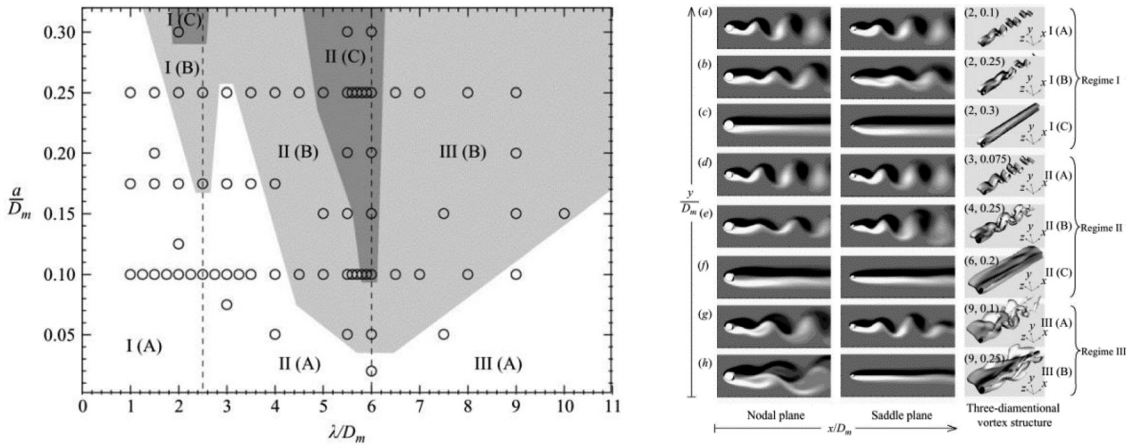

FIG. 32. (a) Formation of different flow regimes behind wavy cylinders based on the wavelength and amplitude, and (b) three-dimensional flow structure together with the flow field behind the nodal plane and the saddle plane at different flow regimes. (The symbol ○ stands for each wavy cylinder case in simulations of Lam and Lin[166]). Reproduced with permission from Lam and Lin, J. Fluid Mech. **620**, 195–220 (2009). Copyright 2009 Cambridge University Press.[166]

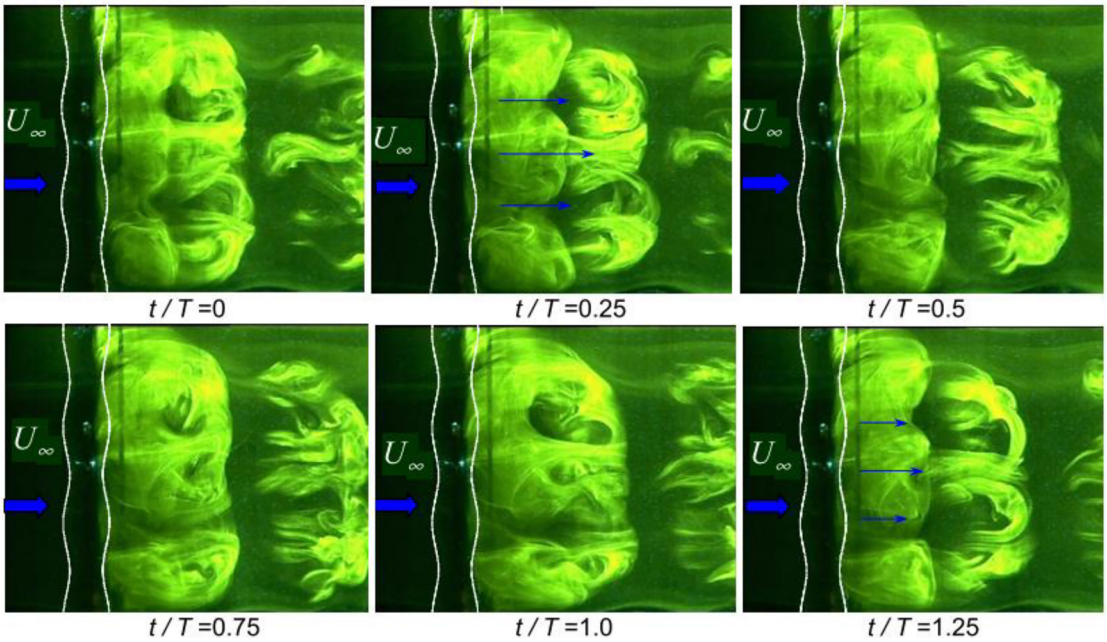

FIG. 33. Spanwise flow structure behind a wavy cylinder at $Re = 600$. Reproduced with permission from Wang *et al.*, J. Visualization **8**, 49–56 (2005). Copyright 2005 Springer Nature.[164]

amount of the ambient fluid. New *et al.*[169] found that the aspect ratio, the exact geometric nodal and saddle locations, and the presence of end-walls could have significant effects on the flow characteristics around sinusoidal cylinders. This could be ascribed to the formation of recirculating regions near the end-walls, which can alter the distributions of the spanwise fluid flows, where the fluid moves from the saddles to the nodes, and vortex formation length. However, sinusoidal cylinders with a shorter wavelength are less affected by these geometric parameters. In subsequent work, New *et al.*[170] added that the coherent cylinder and wall vortex shedding behind a confined sinusoidal cylinder could be suppressed with a shorter wavelength and a higher wave amplitude.

Doddipatla *et al.*[171] investigated the effects of the trailing-edge waviness on the flow characteristics behind a D-shaped cylinder with a semi-elliptical leading-edge. It was found that although the near-wake region is considerably influenced by the sinusoidal trailing-edge, the fluid flow is less affected for $X/D > 4$ and behaves similarly to the smooth trailing-edge case where the flow tends to develop naturally with small-scale flow features and streamwise vortices. They also highlighted that the streamwise vortices in the sinusoidal trailing-edge case are more energetic than in the smooth trailing-edge case. However, the spanwise vortices are less organized and weaker. This was considered to be the main reason for the base drag reduction in the sinusoidal trailing-edge case. In contrast to Wang *et al.*,[164] Bai *et al.*[172] found that in a sinusoidal cylinder with a long wavelength of 6D, the wake is relatively wide behind the nodal plane, while a narrower wake is produced behind the saddle plane. This discrepancy was attributed to the different flow separation angles over the wavy cylinder. The results also showed that the shedding of the large-scale vortical structures behind the saddle plane occurs at a higher frequency than that behind the nodal plane. Moreover, they found a larger recirculation bubble length downstream of the saddle plane than the nodal plane for $\lambda/D = 2$, while an opposite behavior is reported for $\lambda/D = 6$.

Seal-vibrissa-shaped cylinders have recently become popular due to the outstanding capability of seals to hunt in the dark sea, which is believed to be related to their vibrissa's shape.[173] According to Fig. 34, Hanke *et al.*[174] characterized the geometry of seal-vibrissa-shaped cylinders with the lengths of the major and minor axes of two governing ellipses (a, b, k, and l), the distance between these two ellipses (M), and

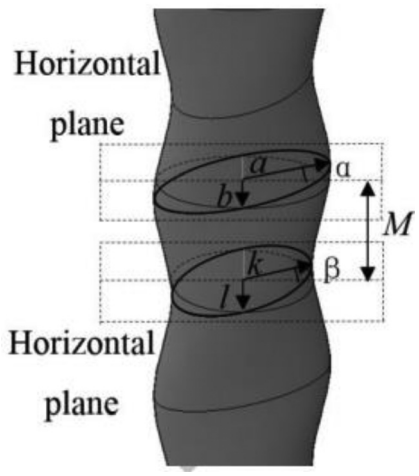

FIG. 34. Geometry of seal-vibrissa-shaped cylinders. Reproduced with permission from Chen *et al.*, Exp. Therm. Fluid Sci. **99**, 169–180 (2018). Copyright 2018 Elsevier.[176]

the incidence angles from each vibrissa (α, β). Wang and Liu[175] investigated the fluid flow behind a seal-vibrissa-shaped cylinder and compared it to those behind circular, elliptical and sinusoidal cylinders. They found that the streamwise and longitudinal velocity fluctuation intensities substantially decrease behind the seal-vibrissa-shaped cylinder. Furthermore, the recirculation zone was notably reduced in the nodal plane of the seal-vibrissa-shaped cylinder. Chen *et al.*[176] highlighted that turbulent kinetic energy is lower behind the seal-vibrissa-shaped cylinder than behind the circular one. In addition, this type of bionic cylinders could suppress the fluctuating lift and decrease the mean drag. More details of experimental studies, including the effect of Reynolds number, amplitude, wavelength, and turbulence intensity, are given in Table II for wavy cylinders. It should be mentioned that the details marked by the star symbol are calculated by the authors of this review.

2. Cylinders with discontinuous cross section

Investigations of the flow developments over single-step and dual-step cylinders and the effects of the step length on the vortex shedding dynamics have been conducted aiming to understand the complex flow features behind the step change zone. In addition to their capability for passively controlling the fluid flow, cylinders of different diameters have been utilized in many devices or structures like control towers of airports, antenna members, and radio communication towers.[177] Referring to Fig. 35, three types of vortex cells (distinct coherent structures shed at different frequencies in bluff body wakes[178]) were identified behind the single-step cylinders. The spanwise vortices behind the large and small cylinders are named L-cell and S-cell, respectively, while the N-cell belongs to the distinct vortex shedding in the zone between the S-cell and L-cell. Furthermore, two kinds of streamwise vortices, namely, the junction vortex and edge vortices, are created behind this type of cylinders. The junction vortex resembles a hairpin shape and wraps around the small cylinder base, while the edge vortices roll up over both sides of the step zone along the larger cylinder.[179] Single-step cylinders have been studied by several scholars in the past decades.[180,181] Dunn and Tavoularis[179] found that the N-cell has the lowest shedding frequency among spanwise vortices, and emerges cyclically behind the large cylinder near the step. They also ascribed the formation of N-cells to the downwash from the step trailing-edge. Morton and Yarusevych[182] revealed that the shedding frequency of the N-cell is slightly lower than that of the L-cell at a turbulent vortex shedding regime. Morton and Yarusevych[183] revealed that the difference in the frequency and strengths of vortex cells causes complex vortex interactions at cell boundaries. For example, N-cell vortices are separated to at least two vortex filaments. While one of these filaments is linked to the S-cell vortex, the other one is connected to the next N-cell vortex. On the other hand, a wider transition zone was found at the N-L cell boundary and its spanwise extent fluctuates temporally.

Morton and Yarusevych[182,184–187] have carried out extensive investigations in this area and made significant contribution in broadening our knowledge about the flow topology and characteristics behind stepped cylinders. Below, their most important findings regarding the physics of flow behind single- and dual-step cylinders are discussed and summarized. Based on the aspect ratio of the larger cylinder (L/D) and the dimeter ratio (D/d), Morton and Yarusevych[187] classified the fluid flow behind dual-step cylinders into different regimes, which is shown in Fig. 36. Wake topology of these flow regimes visualized with the help of a tomographic PIV is demonstrated in Fig. 37. In the cellular shedding regime (CS) where L/D is high, multiple vortex shedding cells are formed in the wake of the large cylinder. With a decrease in L/D, transition to the low-frequency shedding (LFS) regime occurs. Hence, a single-cell vortex shedding is formed over the entire span of the larger cylinder. Furthermore, the vortex shedding frequency of this cell is lower than that reported for a uniform cylinder with a diameter of D. According to Fig. 37(a), the recirculation region behind the larger cylinder in this flow regime is comparable to that behind a smooth circular cylinder.

The behavior of the flow regime becomes a function of the diameter ratio when L/D is further reduced. The irregular shedding (IS) regime is formed at a higher diameter ratio, which is identified as the shortage of consistent vortex shedding pattern in the wake of large cylinders. The coherence and strength of the vortex shedding in this flow regime is lower than those in LFS and CS regimes. As shown in Fig. 37(b), the IS regime is characterized by a wider and longer recirculation zone behind the larger cylinder and vortices shedding into the wake deform as hairpin-like structures. However, no recirculation zone is found behind the small cylinder near the boundary zone. This flow regime is recognized as the asymmetric irregular shedding (AIS) regime when it is accompanied by asymmetry in the flow topology with respect to the zx symmetry plane. The high frequency shedding (HFS) is another regime observed in almost the same L/D range as IS and AIS flow regimes, however, at a lower diameter ratio. The frequency of shedding in this regime is up to 30% higher than that of a uniform circular cylinder. As shown in Fig. 37(c), the vortex dislocations are detected in this flow regime between the large and small vortices downstream of the step changes. Finally, no shedding (NS) regime is formed when L/D is sufficiently low. Collapse of separated shear layers extending from the large cylinder is the main feature of this flow regime. As shown in Fig. 37(d), no significant recirculation region downstream of the larger cylinder is observed in NS regime, while the spanwise vortices are formed behind the smaller cylinder.

V. EFFECTS OF UNSTEADY INFLOW

Unsteady inflow has been the focus of many studies since it resembles real working conditions. It could be classified into two main categories, periodic and non-periodic. In periodic inflow, the velocity is regulated with a defined frequency and amplitude, while in non-periodic inflow, the velocity reaches a higher or a lower value with specified acceleration or deceleration rates.

A. Periodic inflow

Bluff bodies under a periodic inflow have many applications in engineering and in the environment like power cables and civil engineering structures working under the periodic wind flow. The periodic inflow can be further divided into pulsating and oscillatory flows. A periodic inflow with a non-zero mean velocity is referred to as a pulsating flow where the velocity is regulated as $U(t) = U_0 + \Delta u \times \sin(2\pi Ft)$. In contrast, in a purely oscillatory flow, the mean velocity is zero. As most of studies in this field of research are dedicated to the pulsating inflow, only this type of inflow is discussed here.

TABLE II. A summary of experimental studies about wavy cylinders.

Paper	Bluff body	Re	A	λ	TI (%)	Methodology
Zhang *et al.*[161]	Circular cylinder (L0.3 × D_m0.02 m^2)	3000	0.2D_m	2D_m	···	Circulating water channel (L1.2 × W0.3 × H0.25 m^3) •PIV
Ahmed and Bays-Muchmore[162]	Circular cylinder (L0.61 × D_m0.063 5 m^2)	20 000	0.006 35 m	0.050 8 m 0.076 2 m 0.101 6 m 0.127 m 0.152 4 m	<1	Low-speed wind tunnel (0.61 × 0.9 m^2) •Pressure taps Water tunnel (0.61 × 0.9 m^2) •FV (dye injection)
Ahmed *et al.*[163]						•LDV
Wang *et al.*[164]	Circular cylinder (L0.148 × D_m0.017 6 m^2)	200 400	0.001 6 m	0.040 m	···	Return-circuit water tunnel (L0.48 × 0.15 × 0.15 m^3) •Digital PIV •LIF
Lam *et al.*[165]	Circular cylinder (L = 18.2D_m)	3000–9000	0.091D_m	2.273D_m	<0.2	Closed-circuit wind tunnel (L2 × 0.6 × 0.6 m^3) •Two-color fiber-optic LDV Closed-loop water tunnel (L0.5 × 0.15 × 0.15 m^3) •Digital PIV •LIF
Wang *et al.*[167]	Circular cylinder (L0.6* × D_m0.033 m^2)	3000–9000	0.003 m	0.075 m	<0.2	Closed-circuit wind tunnel (L2 × 0.6 × 0.6 m^3) •Two-color fiber-optic LDV
Lee and Nguyen[168]	Circular cylinder (D_m0.02 m)	5000–20 000	0.004 m	0.02 m 0.04 m	<0.08	Subsonic wind tunnel (L6 × W0.72 × H0.6 m^3) •Three-component load cell •Micromanometer •HWA (I-type) particle tracing •FV (smoke-wire)
New *et al.*[169] New *et al.*[170]	Circular cylinder (L0.12 × D_m0.02 m^2)	2700	0.002 m 0.004 m 0.006 m	0.04 m 0.08 m	<2	Recirculating water tunnel (L1.05 × W0.15 × H0.25 m^3) •Time-resolved PIV
Doddipatla *et al.*[171]	Rectangular cylinder with semi-elliptical leading-edge and wavy trailing-edge (L0.61 × H0.025 4 × W0.317 5 m^3)	24 000 46 000	···	2.4H 5.6H	0.3	Open-loop wind tunnel (1.21 × 0.61 × 0.61 m^3) •PIV •Pressure transducer
Bai *et al.*[172]	Circular cylinder (L0.36 × D_m 0.02 m^2)	3000	0.003 04 m	0.12 m	<2.5	Closed-loop water tunnel (L1.1 × W0.45 × H0.6 m^3) •Time-resolved PIV
Wang and Liu[175]	Circular, elliptical, wavy and vibrissa-shaped cylinders	1800	0.000 75 m*	···	<1	Recirculating open-water channel (L1.05 × W0.15 × H0.25 m^3) •Time-resolved PIV

TABLE II. (Continued.)

Paper	Bluff body	Re	A	λ	TI (%)	Methodology
Chen *et al.*[176]	Circular cylinder (L0.8 × D0.07 m^2)	50 000	0.001 75 m*	0.07 m	0.4	Closed-circuit wind tunnel (H1.2 × W0.8 m^2)
				0.14 m		•Pressure taps
	Vibrissa-shaped cylinder (L0.8 × D0.073 3 m^2)			0.28 m		•Six-component force balance •High-resolution PIV

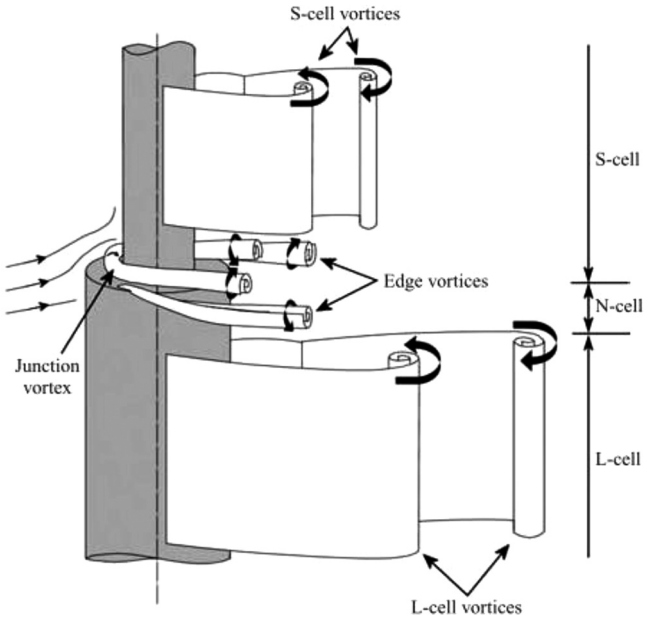

FIG. 35. Different types of vortices past a single-step cylinder. Reproduced with permission from Dunn and Tavoularis, J. Fluid Mech. **555**, 409 (2006). Copyright 2006 Cambridge University Press.[179]

1. Pulsating inflow

The most important physical phenomenon regarding the pulsating inflow is the vortex shedding lock-on, where the shedding frequency changes to the frequency of the pulsation frequency or its subharmonic and remains constant over a range of inflow velocities (Fig. 38).[188] This phenomenon occurs either when a cylinder is vibrated in the streamwise direction or when the inflow oscillates over a fixed cylinder. It was shown that the lock-on for a circular cylinder happens when the ratio of the pulsation frequency (F) to the natural shedding frequency (F_{S0}) is around two.[189] It can be seen in Fig. 39, under the lock-on condition, vortex formation occurs closer to the cylinder when compared to steady vortex shedding.[190] Pulsation amplitude is an important parameter to describe the unsteady inflow, which can either be defined as $A = \Delta U/U_0$ or $A^* = \Delta U/2\pi FD$. Al-Asmi and Castro[191] showed that the lock-on phenomenon happens at a lower range of the frequency ratio (F/F_{S0}) for a lower pulsation amplitude. For instance, for a cylinder having a trapezoidal leading-edge and a triangular cylinder, the lock-on phenomenon happens over frequency ratios from 1.1 to 2.1 at pulsation amplitude of 0.15. However, frequency ratios are restricted to $1.5 < F/F_{S0} < 2.1$ at a lower amplitude of $A^* = 0.05$. The ranges of the frequency ratio for a flat plate and a rectangular cylinder are even lower at the same pulsation amplitude, $1.9 < F/F_{S0} < 2.05$ for the flat plate and $1.9 < F/F_{S0} < 2.3$ for the rectangular cylinder. The same observation was also made by Wolochuk *et al.*[188] They calculated the lock-on range behind a triangular cylinder and compared it with those of three other types of cylinders (a flat plate, a circular cylinder, and a cylinder with a semi-circular trailing-edge) investigated in Ref. 192. They concluded that the lock-on range in the circular cylinder is nearly two times larger than that in bluff bodies with sharp edges. Hu *et al.*[193] studied the flow characteristics

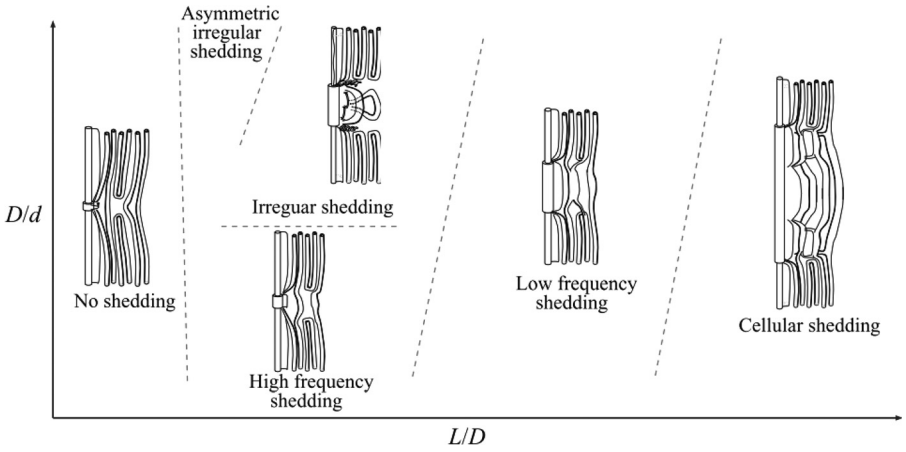

FIG. 36. Flow pattern behind a dual-step cylinder based on L/D and D/d. Reproduced with permission from Morton and Yarusevych, J. Fluid Mech. **902**, A29 (2020). Copyright 2020 Cambridge University Press.[187]

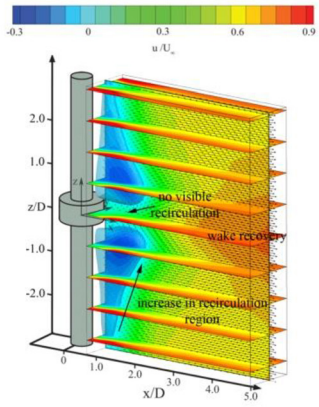

(a) low frequency shedding regime ($L/D = 5$, $D/d = 1.33$)

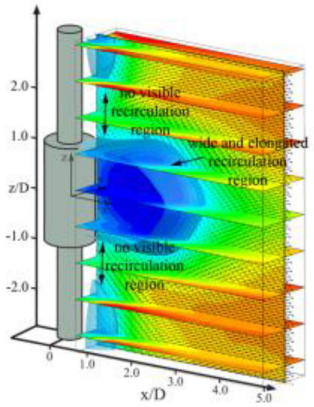

(b) irregular shedding regime ($L/D = 2$, $D/d = 2$)

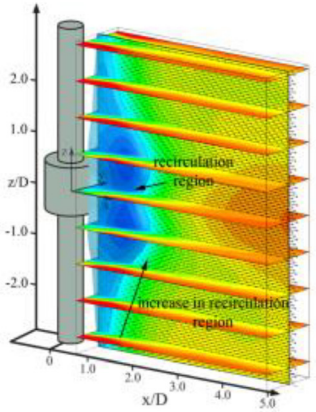

(c) high frequency shedding regime ($L/D = 1$, $D/d = 2$)

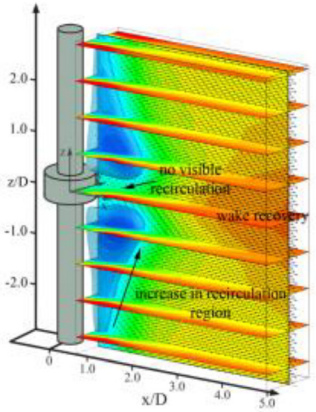

(d) no-shedding regime ($L/D = 0.5$, $D/d = 2$)

FIG. 37. Planar contours of the mean streamwise velocity behind a dual-step cylinder at $Re = 2000$ (a) low-frequency shedding regime, (b) the irregular shedding regime, (c) high-frequency shedding regime, and (d) no-shedding regime. Reproduced with permission from Morton *et al.*, Phys. Fluids **28**, 025104 (2016). Copyright 2016 AIP Publishing LLC.[186]

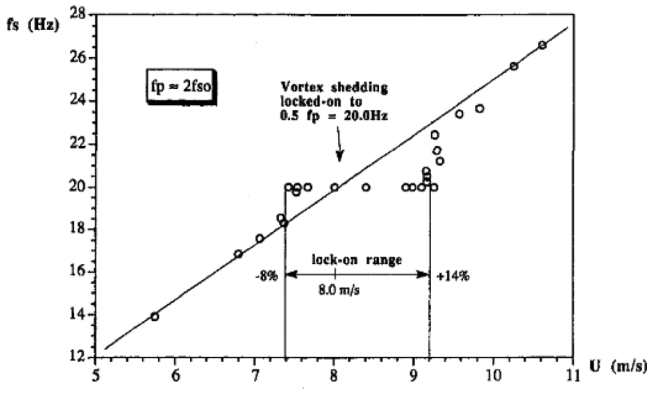

FIG. 38. Shedding frequency against the inflow velocity during the lock-on at $F/F_{S0} = 2$. Reproduced with permission from Wolochuk *et al.*, J. Fluids Eng. **118**, 18–25 (1996). Copyright 1996 The American Society of Mechanical Engineers.[188]

behind a cylinder with a trapezoidal leading-edge under the pulsating water pipe flow for $6170 < Re < 24\,600$. They identified three flow regimes of quasi-steady vortex shedding at $F/F_{S0} < 0.23$, hysteresis vortex shedding at $F/F_{S0} = 0.23$–0.64 and finally non-interactive vortex shedding at $0.64 < F/F_{S0} < 3.45$.

Konstantinidis and his colleagues carried out extensive investigations on the effects of unsteady inflow on the bluff body wakes.[195–199] Here, some of their most important experimental studies are reviewed. By analyzing the wake characteristics behind a circular cylinder under periodic inflow conditions, Konstantinidis *et al.*[194] revealed that the recirculation bubble length and the vortex formation length behind a circular cylinder under the pulsating inflow reduce to a minimum value about the middle of the lock-on range. It was also found that increasing pulsation amplitude at constant frequency leads to a further decrease in the size of the recirculation bubble as well as the vortex formation region. In another research study, Konstantinidis *et al.*[195] assumed that the forced wake behind a stationary circular cylinder in a low-amplitude pulsating inflow is equivalent to a cylinder, which is forced to oscillate in a steady fluid flow at a wavelength larger than the cylinder diameter. They also mentioned that there exists a notable consistency between the response branches of a freely oscillating cylinder and the wake modes behind a cylinder forced to oscillate. Therefore, pulsation frequency of the inflow (F) was correlated with the structural frequency (F_n) of the cylinder, acting as an excitation frequency in free vibrations. According to Fig. 40, two positive excitation regions were found for a flexibly mounted cylinder on either side of the lock-on region for a forced cylinder oscillation. Analysis of the symmetric vortex shedding behind a circular cylinder at $3 < F/F_{S0} < 4$ was conducted in their further research.[196] They showed that the symmetric pattern of twin vortices in the very near-wake becomes antisymmetric further downstream and the number of cycles that the symmetric arrangement remains stable depends on the pulsation frequency and amplitude.

Konstantinidis *et al.*[197] focused on the bimodal vortex shedding, where two different modes ($2S \leftrightarrow 2P$) are recognized in the wake of a perturbed cylinder. Mode S is identified as compressed and well-defined vortices after shedding from the cylinder, while the elongated shear layer vorticity strand is the main characteristic of mode P, which exists only for $F/F_{S0} < 2$. More recently, Konstantinidis and Balabani[198] clarified that an increase in the pulsation amplitude causes the velocity fluctuations and Reynolds stresses in the wake region to increase substantially. Furthermore, the drag coefficient linearly increases with the pulsation amplitude due to the separated shear layers to roll up closer to the cylinder, and consequently, the vortex strength is amplified. Similar to Konstantinidis *et al.*,[194] Jarża and Podolski[199] reported a shortening of the vortex formation length in the lock-on region.

Reynolds stress in the near-wake region of a circular cylinder in the lock-on region was studied by Kim *et al.*[200] using high-definition PIV. Similar to Konstantinidis and Balabani,[198] they found that Reynolds stresses in the lock-on region are considerably higher than those in the steady flow and the maximum $\overline{u'u'}$, $\overline{u'v'}$, and $\overline{v'v'}$ are, respectively, 59%, 25%, and 24% higher than those for the natural vortex shedding. Furthermore, $\overline{u'u'}$ and $\overline{u'v'}$ are identified with a twin-peak pattern and a peak-and-valley pattern, respectively, while $\overline{v'v'}$ is characterized by a one-peak pattern on the wake centerline. Based on the dimensionless pulsation amplitude ($\beta = U_{max} - U_{min}/U_{max} + U_{min}$) and the Strouhal number, Mikheev *et al.*[201] classified the flow topology behind a circular cylinder in a pulsating inflow into four regimes of quasi-steady pattern, shedding of pairs of large-scale and non-symmetric vortices, alternative separation-free flow on opposite sides of the cylinder, and finally fully synchronized vortex shedding with forced freestream velocity pulsations. They also claimed that although the blockage and aspect ratio could affect the near-wake region, qualitative characteristics remain almost unchanged. Li *et al.*[202] analyzed aerodynamic pressures of a 5:1 rectangular cylinder under pulsating inflows and indicated that the maximum RMS pressure coefficient and the Strouhal number increase with gust amplitude, while the separation bubble length considerably reduces. In another study, Wu *et al.*[203] measured aerodynamic forces of a 5:1 rectangular cylinder under streamwise sinusoidal flows and also separated inflow-induced and vortex-induced components of the total forces. Aforementioned studies on the pulsating inflow are tabulated in Table III.

B. Non-periodic inflow

Inflow velocity through a non-periodic inflow could be changed either uniformly or impulsively.[204] In contrast to impulsively started cylinder, the inflow velocity in uniformly accelerated or decelerated inflow increases gradually. An impulsively started cylinder is seen in various practical applications like in the pressure suppression pool of boiling water nuclear reactors.[205] Uniformly accelerating flow is also of direct relevance to many structural damages resulted from tornadoes and downbursts having periods of the sudden wind accelerations.[206] Experimental investigations regarding non-periodic inflows were conducted either by moving the body through a quiescent working fluid (towing tank), or by fixing the body and regulating the inflow velocity in a wind tunnel or a water channel. In both conditions, the fluid flow display different features in comparison with the quasi-steady condition.[207] The non-periodic inflow is governed by a dimensionless number, namely, the acceleration parameter $A_p = D/U_0^2(du/dt)$, where D and U_0 are the diameter and the mean velocity of the cylinder, respectively. However, some papers used viscous scale to define their acceleration parameter, $A_P = D^3/\nu^2(du/dt)$ (where ν is the

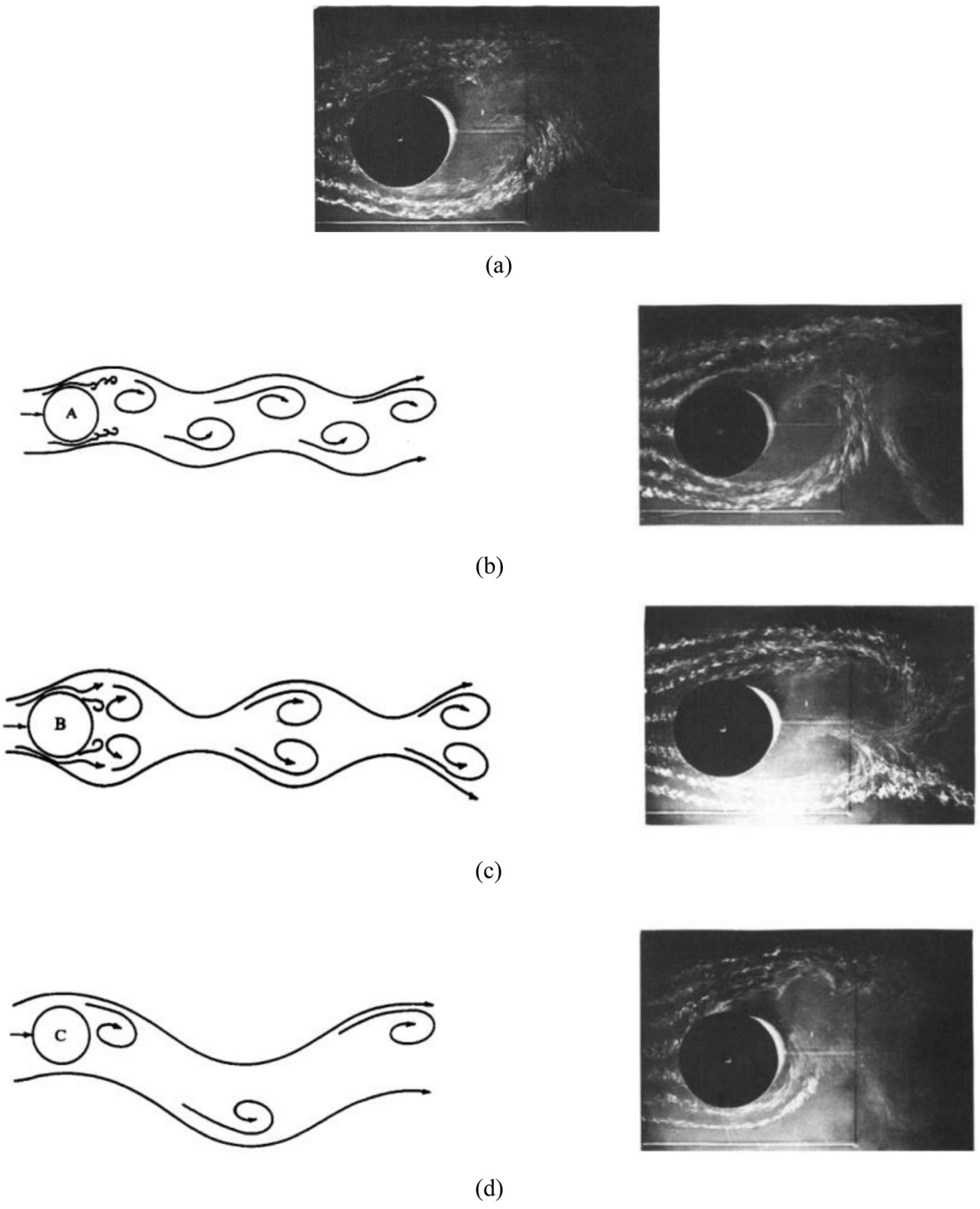

FIG. 39. Flow visualization at $Re = 40\,000$ and $F_{S0} = 3.65$ Hz together with schematic representations of the vortex-shedding pattern (a) steady flow, (b) $F/F_{S0} = 0.41$, (c) $F/F_{S0} = 0.71$, and (d) $F/F_{S0} = 1.23$. Reproduced with permission from Barbi *et al.*, J. Fluid Mech. **170**, 527–544 (1986). Copyright 1986 Cambridge University Press.[190]

kinematic viscosity) and the others used acceleration ($a = du/dt$) directly to show the variation in the mean flow velocity. It is worth mentioning that the flow can be considered as impulsive for large values of A_p while uniformly accelerated or decelerated for $A_p < 0.27$.[208]

1. Impulsive inflow

Similar to the steady flow discussed in Sec. III, the fluid flow behind an impulsively started cylinder could be divided into different regimes based on the Reynolds number. Bouard and Coutanceau[209]

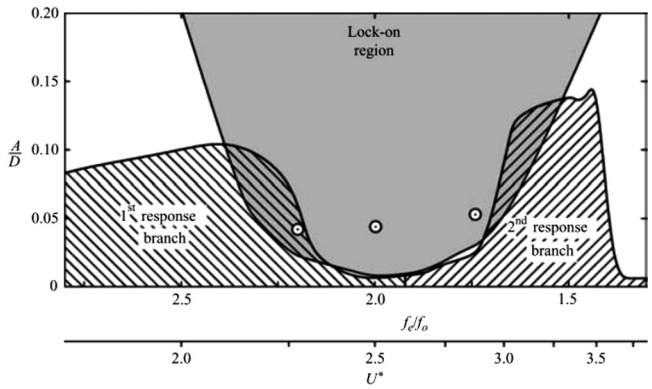

FIG. 40. Flow behavior modes for a forced cylinder oscillations vs a flexibly mounted cylinder. Reproduced with permission from Konstantinidis *et al.*, J. Fluid Mech. **543**, 45–55 (2005). Copyright 2005 Cambridge University Press.[195]

identified three flow regimes, which are $Re < 60$, $60 < Re < 500$, and $Re > 500$. In the first regime, the flow is separated from the cylinder a short time after the impulse and a main eddy is formed. In the second flow regime, as represented in Fig. 41, the streamlines are distorted close to the middle of the rear stagnation and separation points, leading to the formation of a bulge and ultimately a secondary eddy tends to rotate in the opposite direction to the main eddy. In the third regime, as Reynolds number increases, two phenomena (α and β) with distinct features are observed which are highly time-dependent (Fig. 42). For phenomenon α, the secondary eddy formed in the previous regime develops in size and finally is split into two smaller eddies having the same size and strength. However, for phenomenon β, a pair of secondary eddies are found near the separation point, and its adjacent vortex on the right side is in close connection with the rapidly rotating vortex near the center of the cylinder.

Using laser-induced photochemical anemometry, Chu and Liao[210] found the same results as Bouard and Coutanceau[209] and identified phenomenon α behind the circular cylinder at the Reynolds number of 1333. Lin *et al.*[211] focused on the formation process of the main eddy and the secondary vortices, as well as the onset of the vortex shedding behind a circular cylinder in impulsive motion and supplemented the discussions in Bouard and Coutanceau.[209] Table IV explains step by step how the fluid flow is developed in the second flow regime ($Re = 500$).

Finaish[212] found that the flow development behind a square cylinder in an impulsive flow at $Re = 200$ is initially similar to that behind the circular cylinder where separation of the top and the bottom shear layers takes place immediately. The process of vortex splitting, which is resulted from stretching of upper vortex by lower vortex, however, tends to continue for the square cylinder (Fig. 43). Tonui and Sumner[213] concentrated on the development of the near-wake recirculation region behind square, diamond, and circular cylinders right after the impulsive start until the wake turns out to be asymmetric ($t^* = 4$ or 5). They pointed out that the impulsively started square and diamond cylinders have a longer recirculation zone than the circular cylinder. It was also shown that the primary eddy strength, the maximum vorticity magnitude, and the cross-stream spacing of the primary eddies in the wake of the circular and square cylinders are almost the same for $t^* > 2$. Sarpkaya and Ihrig[205] tested the aerodynamic forces on an inclined rectangular cylinder under impulsively start at a Reynolds number of 20 000 and concluded that the shedding of the first few vortices have significant effects on both lift and drag.

2. Uniformly accelerated or decelerated inflow

Different flow characteristics behind bluff bodies could be observed when the inflow is accelerated or decelerated uniformly. Tatsuno and Taneda[214] showed that for a large deceleration rate, the length of the two vortices formed behind cylinders increases monotonically until reaching the rest state where the test body is stopped. However, for a very small deceleration rate, these twin vortices are shortened steadily during the deceleration but elongated rapidly just before stopping. Taneda and Honji[204] discovered that the critical time for the symmetric wake bubble to become asymmetric reduces with increasing acceleration parameter $[A'_P = D^3/\nu^2\ (du/dt)]$. Lee and Budwig[207] manifested that the critical Reynolds number in which the wake instability occurs is shifted to a higher value in a uniformly accelerating flow. The drag coefficient under an unsteady inflow also differs from that of the quasi-steady one, which was found by Lee *et al.*[215] at Reynolds numbers between 40 000 and 164 000. They also clarified that the drag coefficient of the circular cylinder in a uniformly accelerating flow is lower than that in a steady flow at low Reynolds number regime. However, the opposite trend is reported at high Reynolds numbers. On the other hand, the square cylinder in an accelerated flow experiences higher drag than that in a steady flow for the entire Reynolds number range. Yang and Mason[216] examined the aerodynamic forces on a rectangular cylinder with side ratios of 1/3, 1, and 3, for both steady and accelerating inflow. In contrast to Lee *et al.*,[215] they concluded that the lift and drag coefficients in an accelerating flow are generally smaller than those in a steady flow. However, similar to Lee and Budwig,[207] they concluded that the onset of wake instability is delayed to a higher Reynolds number in comparison with that in steady flow. Further information on experimental studies of nonperiodic inflow condition is provided in Table V.

VI. EFFECTS OF SURROUNDING SURFACES

Bluff bodies close to a surface are encountered in various engineering applications. Here, works on flow around bluff bodies, which are either confined in a channel or placed in the vicinity of water free surface or a rigid surface, are reviewed in detail.

A. Confinement or blockage

The importance of flow around confined bluff bodies is recognized mainly for two reasons. The first is credited to their wide applications in industry like heat exchangers and the second is attributed to the characteristics of many experimental facilities like wind tunnels and water channels having solid boundaries.[217,218] Experimental results can be affected in the presence of test section walls due to blockage or wall interference effects. Blockage effect is further divided into three main types: solid blockage, wake blockage, and wall boundary layer blockage. Effect of test section walls on object wake development and effect of boundary layer growth on test section boundaries are known as wake blockage and wall boundary layer blockage, respectively. Increment of freestream velocity outside of the wake is a consequence of these two blockage effects. However, solid blockage ratio,

TABLE III. A summary of experimental studies about pulsating inflow.

Paper	Bluff body	TI (%)	Re	F	A	Methodology
Wolochuk *et al.*[188]	Triangular cylinders (L0.31 × H0.050 8, 0.025 4, 0.014 9 m^2) Square cylinder (L0.31 × H0.003 25 m^2)	<0.7	480–83 000	10–180 Hz	1%-16%[a]	Open-circuit wind tunnel (L0.91 × 0.3 × 0.3 m^3) •HWA •Differential pressure transducer
Telionis *et al.*[189]	Circular cylinders (D0.089 m)	<0.5	23 000–50 000	<23 Hz	0.04–0.3	Blower-type wind tunnel (L1.24 × 0.741 × 0.529 m^3) •HWA •Hot-film probes •Pressure transducers •Skin-friction gages
Barbi *et al.*[190]	Circular cylinders (D0.15, 0.2 m)	0.4–0.8 0.2	3000–40 000	0.2–2 Hz 1.2–6.75 Hz	0.1–0.25 0.1–0.5	Closed-circuit water tunnel (0.3 × 0.25 m^2) •LDV •FV (dye injection) Open-circuit wind tunnel (L3 × 0.5 × 1m^3) •HWA •FV (smoke injection)
Al-Asmi and Castro[191]	Rectangular cylinder (H0.99 × W0.67 m^2) Triangular cylinder (H0.1 × W0.1 m^2) Trapezoidal cylinder (H0.1 × W0.015 m^2) Rectangular cylinder with trapezoidal leading-edge (T-shape) (H0.1 × W0.1 m^2)	<0.4 <0.1	5000–50 000	F/ F_{S0}=0–4	0–0.25	Low-speed wind tunnels (L3 × 0.3 × 0.3 m^3) (L4 × 0.9 × 0.6 m^3) •Micromanometer •HWA •FV (smoke injection)
Armstrong *et al.*[192]	Rectangular cylinder with semi-circular trailing-edge (L1.1 × H0.111 m^2) Circular cylinder (L1.1 × D0.101 m^2) Flat plate (L1.1 × 0.101 × 0.012 m^3)	<0.02	15 000 < Re < 35 000	9.24 Hz 12.36 Hz	<0.03[a]	Wind tunnel (L3 × 1.2 × 1.2 m^3) •HWA •Micromanometer
Hu *et al.*[193]	T-shaped cylinder (L0.16 × H0.032 m^2)	<0.5	6170–24 600	0.146 Hz 0.293 Hz 0.585 Hz F/F_{S0} = 0.29–14.64	<0.4	Circular water pipe (D0.151 m) •Hot-film probe

TABLE III. (*Continued.*)

Paper	Bluff body	TI (%)	Re	F	A	Methodology
Konstantinidis *et al.*[194]	Circular cylinder (L0.072 × D0.007 2 m^2)	3.3	2150	14.6–20 Hz F/F_{S0} = 1.6–2.3	A = 0–0.2 A^* = 0–0.1	Closed-circuit water tunnel (W0.072 × H0.072 m^2) •LDV •Flow visualization
Konstantinidis *et al.*[195]	Circular cylinder (D0.007 2 m)	3.3	2150–2170	15.4–19.5 Hz F/F_{S0} = 1.74–2.2	0.06–0.063	Recirculating-type water rig (W0.072 × H0.072 m^2) •Digital PIV •LDV
Konstantinidis and Balabani[196]	Circular cylinder (D0.007 2 m)	3	1180–1240	F/F_{S0} = 3–4	A^* = 0.02, 0.04	Closed-circuit vertical water tunnel (L0.195 × W0.072 × H0.072 m^3) •Digital PIV •LDV
Konstantinidis *et al.*[197]	Circular cylinder (D0.007 2 m)	···	2100–2200	F/F_{S0} = 1.74–1.87	0.04–0.09	Closed-circuit vertical water tunnel (L0.195 × W0.072 × H0.072 m^3) •Digital PIV
Konstantinidis and Balabani[198]	Circular cylinder (L0.072 × D0.007 2 m^2)	3	2150	17.8 Hz	0.08–0.23	Recirculating-type water rig (W0.072 × H0.072 m^2) •Double-pulsed PIV •LDV
Jarża and Podolski[199]	Circular cylinder (L0.6 × D0.08 m^2)	<0.15	···	0–30 Hz	0.07	Open-circuit wind tunnel (L4 × W0.6 × H0.6 m^3) •Two pressure transducers •HWA •Hot-film probes •Skin friction gauge
Kim *et al.*[200]	Circular cylinder (L0.15 × D0.005 m^2)	0.2	360	F/F_{S0} = 2	0.047	Closed-cycle water tunnel (L1 × W0.15 × H0.1 m^3) •Time-resolved PIV
Mikheev *et al.*[201]	Circular cylinder (D0.05, 0.11 m)	2–5.5	4000–10 600	0–4 Hz	β = 0–0.8	Wind tunnel (L2.73 × W 0.38 × H0.38 m^3) •Flow visualization •HWA
Li *et al.*[202]	Rectangular cylinder (L0.496 × W0.15 × H0.03 m^3)	<0.6	13 000	0.4, 1 Hz	0.055–0.192[b]	Closed-circuit-type wind tunnel (L5 × W 0.5 × H 0.5 m^3) •Pressure taps
Wu *et al.*[203]	Rectangular cylinder (L1.3 × W0.15 × H0.03 m^3)	···	16 080	0.2–1.2 Hz	0–0.25	Open-circuit wind tunnel (L10 × W1.5 × H1.8 m^3) •Pressure scanners

[a]Root-mean-square perturbation amplitude of the velocity ($A/\sqrt{2}$).
[b]Root-mean-square of gust amplitude.

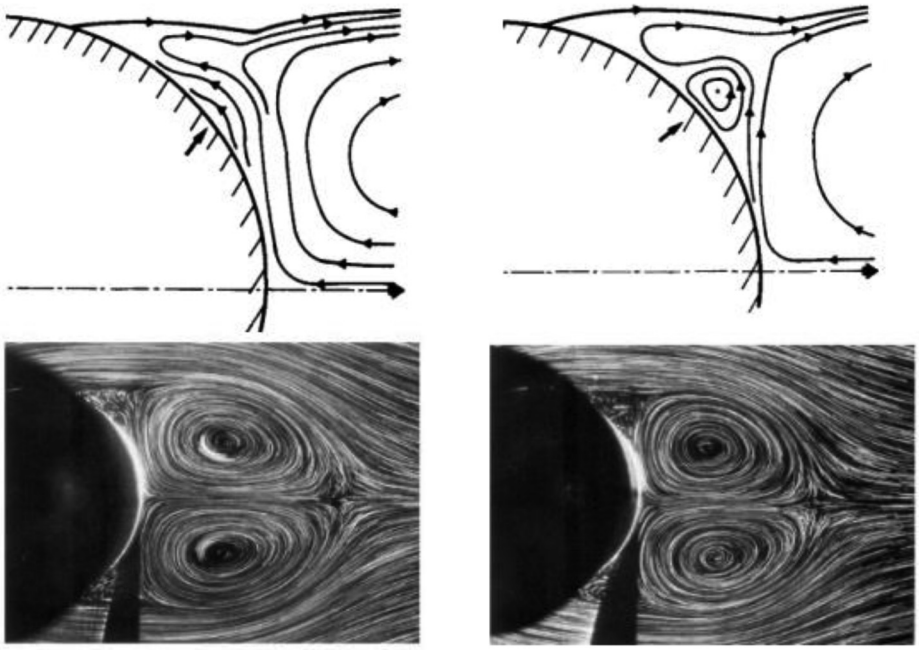

(a) bulge (b) little secondary eddy

FIG. 41. Physics of flow behind an impulsively started cylinder in the second flow regime (a) $Re = 300$ and $t^* = 2.5$ ($t^* = tU/D$), and (b) $Re = 550$ and $t^* = 2.5$. Reproduced with permission from Bouard and Coutanceau, J. Fluid Mech. **101**, 583–607 (1980). Copyright 1980 Cambridge University Press.[209]

which results from mounting of the model in a closed test section, affects force and moment measurement inevitably.[219,220]

Confinement or blockage is conventionally quantified using the ratio of the frontal area of the bluff body to the test section area.[219] It was shown that the onset of vortex shedding is delayed and the Strouhal number increases in a confined channel.[221–223] Reyes *et al.*[224] highlighted that in contrast to unconfined bluff body flows, vortex shedding does not start abruptly behind a confined square cylinder. In fact, there exists a Reynolds number range in which the closed recirculation bubble pulsates prior to the shedding process. Rehimi *et al.*[225] showed that the first transition to three dimensionalities in the flow field past a confined circular cylinder with a blockage ratio of 0.33 occurs at $Re = 159$ with a spanwise length scale of 3D, which is similar to mode A behind an unbounded circular cylinder. As shown in Fig. 44, an increase in Reynolds number above 277 makes the instability longitudinal with a spanwise length scale of D. This longitudinal instability was shown to be similar to mode B recognized in the unconfined cylinder at $Re = 230$–260. The effects of confinement on the transition to three dimensionalities behind a square cylinder were also studied by Madhavan *et al.*[226] for $Re \leq 250$ and a blockage ratio of 0.25. Mean flow patterns, dynamic vortex shedding and pairing, critical blockage ratio, and Reynolds shear stress of three bluff bodies, namely, circular cylinder, square cylinder, and flat plate, were analyzed and compared by Wang *et al.*[227] for blockage ratios from 0.25 to 0.5 at Reynolds numbers of 3200, 4600, and 5400. They showed that vortex shedding pattern is a strong function of blockage ratio rather than Reynolds number particularly for the flat plate. Furthermore, the value of critical blockage ratio at which vortex shedding is suppressed is highest for the circular cylinder.

Fluid flow over bluff bodies confined in a circular pipe has distinct characteristics compared to that in a channel with parallel walls. Based on the *St-Re* diagram, Venugopal *et al.*[228] identified four different flow regimes behind a trapezoidal cylinder placed in a circular pipe for Reynolds number 200 to 200 000 and blockage ratios 0.14, 0.19,

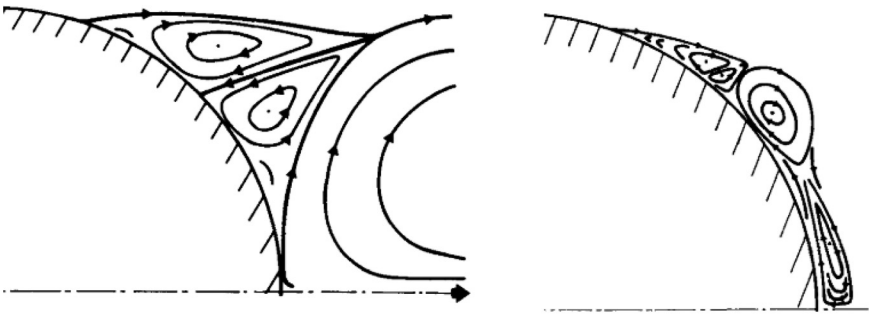

(a) phenomenon α (b) phenomenon β

FIG. 42. Physics of flow behind an impulsively started cylinder in the third flow regime (a) phenomenon α, and (b) phenomenon β. Reproduced with permission from Bouard and Coutanceau, J. Fluid Mech. **101**, 583–607 (1980). Copyright 1980 Cambridge University Press.[209]

TABLE IV. Time progression of the fluid flow behind an impulsively circular cylinder at $Re = 500$.[211]

Phase	Feature
First ($t^* = 0.47$)	•No vortex
	•Flow pattern is like non-viscous flow
Second ($t^* = 0.63$–5.02)	•Formation of two primary vortices
	•Increment of the streamwise and normalwise sizes of these two primary vortices due to the penetration of the ambient fluid in the recirculation region
	•Transition of the core of these two vortices downstream with time
	•Formation of the bulge on the rear surfaces
	•Formation of two pronounced secondary vortices at the separation points
Third ($t^* > 5.62$)	•Onset of the asymmetry in two primary vortices
	•The core of the upper primary vortex is placed at a more downstream distance than that of the lower vortex
	•Domination of one vorticity to another and the onset of the periodic vortex shedding
	•Absence of the secondary vortices after the onset of vortex shedding

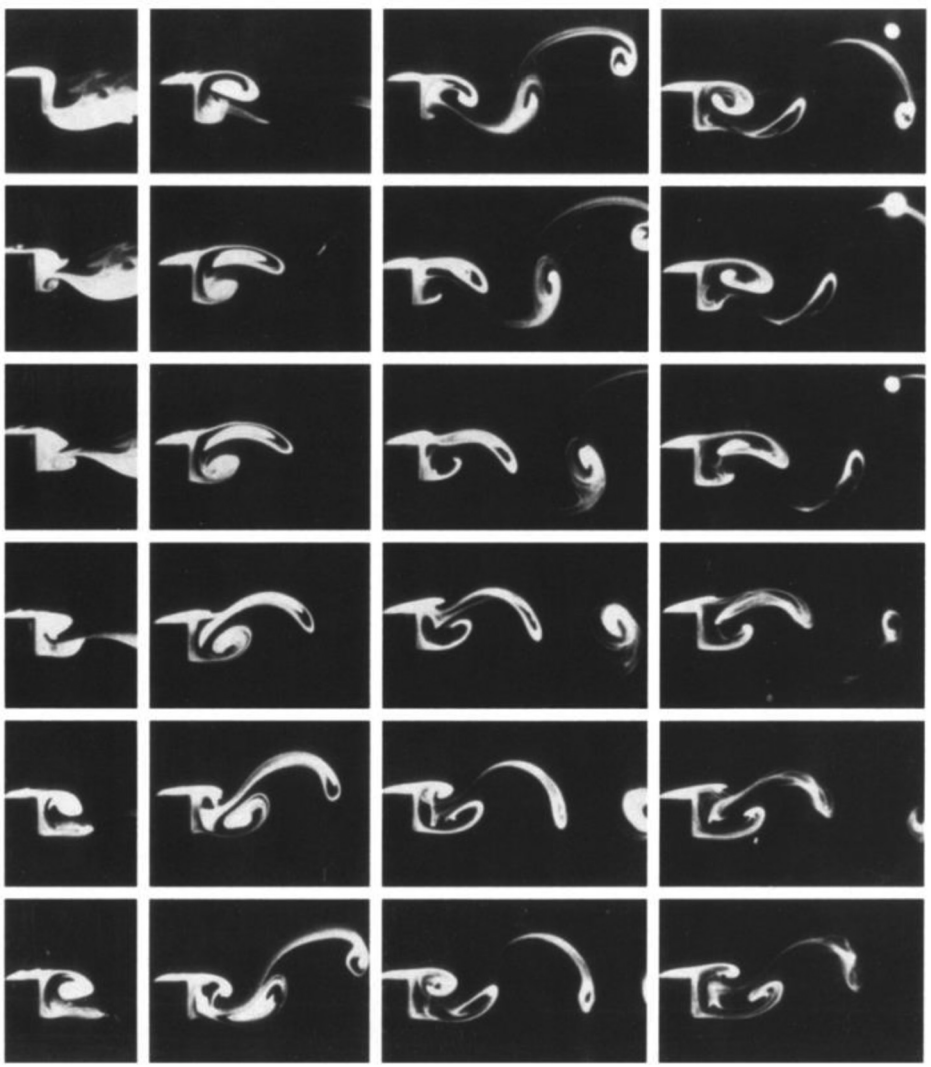

FIG. 43. Flow visualization behind an impulsively started square cylinder at $Re = 200$, $\Delta t = 1/32$s. Reproduced with permission from Finaish, Exp. Fluids **11**, 262–267 (1991). Copyright 1991 Springer Nature.[212]

TABLE V. A summary of experimental studies about non-periodic inflow.

Paper	Bluff body	Inflow type	Re	Acceleration	Methodology
Taneda and Honji[204]	Flat plates ($0.16 \times 0.000\,2 \times 0.013$ m^3) ($0.23 \times 0.001 \times 0.03$–$0.05$ m^3)	Impulsive and uniform acceleration	18–1135	$a = 0.000\,1$–0.10 m/s^2	Two water tanks and a carriage ($L2 \times W0.4 \times H0.4$ m^3) ($L6 \times W0.5 \times H0.5$ m^3) •Aluminum dust method •Electrolysis method •Hydrogen bubble method
Sarpkaya and Ihrig[205]	Rectangular cylinders (0.035, 0.051, $0.043 \times 0.021\,6$, 0.051, 0.07 m^2)	Impulsive	20 000	$A_p = 2.5$	Vertical water tunnel ($L5.2 \times W0.61 \times H0.61$ m^3) •Force transducers •Variable resistance probe
Lee and Budwig[207]	Circular cylinder (D0.000 64, 0.001 2, 0.001 56, 0.003 2, and 0.004 8 m)	Uniform acceleration	20–330	⋯	Suction-type unsteady wind tunnel ($L1.83 \times W0.3 \times H0.3$ m^3) •HWA
Sarpkaya[208]	Two circular cylinders (D0.075, 0.063 5 m)	Uniform acceleration	16 000–50 000	$A_p = 0.05$–1.2	Vertical water tunnel ($L5.2 \times W0.61 \times H0.61$ m^3) •Strain-gaged load cell •Differential pressure transducer
Bouard and Coutanceau[209]	Circular cylinders (D0.03–0.15 m)	Impulsive	40–10 000	$A_p = 49.95$–83.25[211]	Vertical cylindrical tank[57] ($L1 \times 0.46 \times 0.56$ m^3) •FV (magnesium and Rilsan particles)
Chu and Liao[210]	Circular cylinder ($L0.42 \times D0.05$ m^2)	Impulsive	500–3000	$A_p = 11.82$–70.92[211]	Deodorized kerosene towing tank ($L1.52 \times W0.46 \times H0.46$ m^3) •Laser-induced photochemical anemometry
Lin *et al.*[211]	Circular cylinder ($L0.34 \times D0.02$ m^2)	Impulsive	500–2000	$A_p = 6.67$, 7.27	Water towing tank ($L3.06 \times W0.5 \times H0.54$ m^3) •High-resolution PIV •FV (titanium dioxide and thin dye film)
Finaish[212]	Circular and square cylinders ($L0.065 \times D0.013$ m^2)	Impulsive	200	⋯	Stationary support frame and a movable cart ($L1.5 \times W0.91 \times H0.91$ m^3) •Flow visualization
Tonui and Sumner[213]	Circular, square, and diamond cylinders ($L0.711\,2 \times D0.025\,4$ m^2)	Impulsive	200–1000	$A_p = 2$–10	Water towing tank ($L3.96 \times W1.03 \times H0.75$ m^3) •TSI PIV
Tatsuno and Taneda[214]	Three circular cylinders ($L0.112$, 0.214, $0.308 \times D0.002\,61$, 0.005 06, 0.010 25 m^2) Three flat plates ($L0.06$, 0.075, $0.214 \times H0.003\,33$, 0.006 20, 0.012 m^2)	Uniform deceleration	≤ 100	$a = 0.000\,01$–0.1 m/s^2	Two water tanks and a carriage ($L2 \times W0.4 \times H0.4$ m^3) ($L6 \times W0.5 \times H0.5$ m^3) •FV (aluminum dust method)

TABLE V. (Continued.)

Paper	Bluff body	Inflow type	Re	Acceleration	Methodology
Lee *et al.*[215]	Square cylinder (H0.06 m) Circular cylinder (D0.06 m)	Uniform acceleration	40 000–164 000	a = 3.6	Closed-type wind tunnel (L2.44 × W1.3 × H0.96 m^3) (L1.8 × W0.9 × H0.9 m^3) •Pressure transducer
Yang and Mason[216]	Rectangular cylinders (L0.6 × W0.02, 0.06, 0.18 × H0.06 m^3)	Uniform acceleration	0–103 000	$A_p = 0.000\,9–0.002\,6$	Open-circuit suction wind tunnel (L2.36 × W 0.762 × H 0.762 m^3) •HWA •Pressure transducer

and 0.28, which are steady, laminar irregular, transition, and turbulent. While a stationary wake is identified in the steady regime, an irregular and symmetric vortex shedding is observed in the laminar irregular regime. Furthermore, two pairs of mean streamwise vortices are detected in this regime, which are known as the reverse dipole-type structure. The transition flow regime is characterized by a gradual decrease in the Strouhal number and more organized vortex shedding. Finally, in the turbulent regime, the Strouhal number reaches a constant value with regular vortex shedding. Another study recently conducted by Arumuru *et al.*[229] at the same blockage ratios indicated that the flow topology behind a circular cylinder in a circular pipe is similar to the flow structure behind a trapezoidal cylinder mentioned above. A new spectral mode has recently been detected by Ford and Winroth[217] around a D-shaped cylinder with a triangular leading-edge placed in a circular pipe. This mode interacts with the primary vortex shedding mode under certain conditions and creates a lock-on phase, where neither mode can sustain at its own frequency.

B. Ground proximity

This section is concerned with the fluid flow over bluff bodies that are in the vicinity of only one surface, that is, the ground effect. This subject attracts many researchers because of its wide applications particularly in civil engineering where bridges, buildings, or supporting structures are in close proximity to nearby bodies.

Flow around bluff bodies in proximity to a rigid surface parallel to the free steam flow or ground could behave differently in terms of the flow characteristics and topology. Boundary layer thickness, gap ratio (G/D, G being the distance from the bottom of the cylinder to the rigid boundary and D the cylinder's diameter) and Reynolds number are influential parameters in this type of problems.[230,231] For instance, an increase in gap ratio reduces the base pressure and also causes the stagnation point to be shifted upward away from the solid boundary. However, the base pressure increases with the boundary layer thickness on the solid boundary. Furthermore, the drag coefficient increases slightly in thinner boundary layers than in thicker ones at small gap ratios, while it is almost independent of the gap ratio when the cylinder is outside the boundary layer.[230] Based on the gap ratio, Price *et al.*[232] classified the fluid flow behavior into four regimes. Their experiments were performed both in a water channel where the cylinder is stationary, and in a towing tank where the cylinder moves. Results indicated that in the first flow regime with very small gap ratios ($G/D \leq 0.125$), the regular vortex shedding is interrupted, although a periodic motion in the outer shear-layer is observed. Furthermore, the boundary layer on the solid wall separates in both upstream and downstream regions of the cylinder. The second flow regime ($0.125 < G/D < 0.5$) is distinguished from the first one by a noticeable pairing between the separated shear layer from the cylinder and the wall boundary layer. The onset of vortex shedding is observed in the third flow regime ($0.5 < G/D < 0.75$). In the last flow regime ($1 < G/D$), wall boundary layer separation is not seen either upstream or downstream of the cylinder, and the wall effects are insignificant.[233] Visualization of the flow in these regimes is presented in Fig. 45. Khabbouchi *et al.*[234] detected three flow regimes behind a circular cylinder at a Reynolds number of 8700 and stated that the jet-like flow destroys the lower shear layer for $G/D < 0.3$, while the onset of the alternative vortex shedding is prevented. However, a symmetric vortex shedding is found for $G/D > 0.3$.

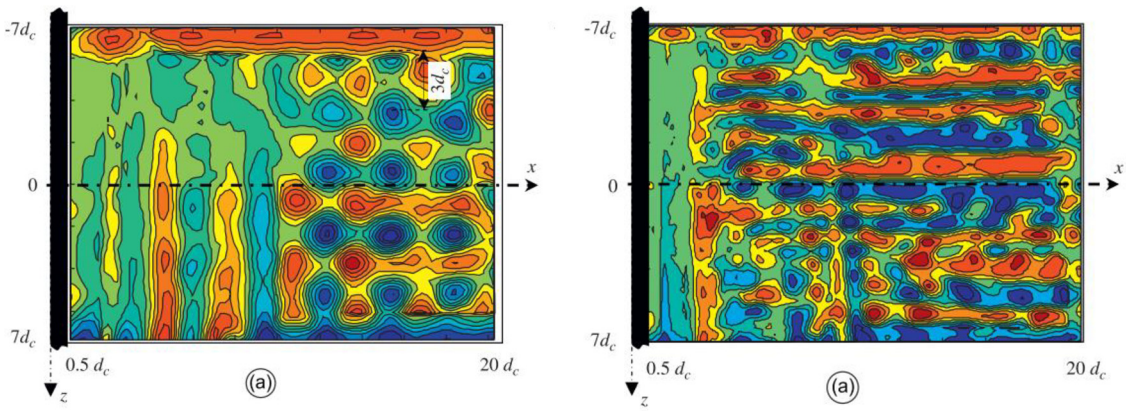

(a) mode A (b) mode B

FIG. 44. Iso-contours for vortex center identification (a) $Re = 159$ and (b) $Re = 400$. Reproduced with permission from Rehimi *et al.*, J. Fluids Struct. **24**, 855–882 (2008). Copyright 2008 Elsevier.[225]

Lin *et al.*[235] found a recirculating eddy on the rigid wall upstream of the circular cylinder for $G/D < 0.5$ and the eddy is enlarged with decreasing gap ratio. This eddy acts as an obstruction and causes the upstream flow to be deflected toward the upper surface of the circular cylinder, resulting in a reduction in the flow velocity through the gap between the cylinder and the rigid wall. They also detected a wall-jet structure for $0.1 < G/D < 0.3$ and concluded that the regular and alternative vortex shedding is suppressed for $G/D < 0.5$.

Yang *et al.*[236] focused on the drag crisis of a circular cylinder close to a rigid wall and demonstrated a remarkable drag coefficient drop from about 0.9 to 0.35 for $G/D \geq 0.5$ at $Re = 1.9 \times 10^5$–2.7×10^5. However, much less reduction in the drag coefficient is reported for the gap ratio between 0.25 and 0.1. It was found by Ouro *et al.*[237] that spanwise rollers with an undulating pattern are formed behind a circular cylinder under wall effects, which are linked to the irregularly located vortices [Fig. 46(a)]. Furthermore, they detected a single vortical structure which is the consequence of the interaction between the von Kármán vortices and a vortex lifted off the ground [Fig. 46(b)]. With the help of PIV, Zhou *et al.*[238] investigated the vortex evolution past a circular cylinder placed close to a solid surface for gap ratio up to 2.5 and the Reynolds number of 1500. It was shown that the Strouhal number increases by 92% when the gap ratio is decreased from 2.5 to 0.25.

Similar to the circular cylinder near a solid boundary, four flow regimes were identified by Martinuzzi *et al.*[239] around a square cylinder, however, with a slight difference in the boundary characteristics. The vortex shedding is fully suppressed in the near-wake zone for $G/D < 0.3$, while it is similar to the unbounded case for $G/D > 0.9$. In addition, an intermittent flow reattachment to the bottom side of the cylinder is observed for $0.3 < G/D < 0.6$, whereas the mean drag and

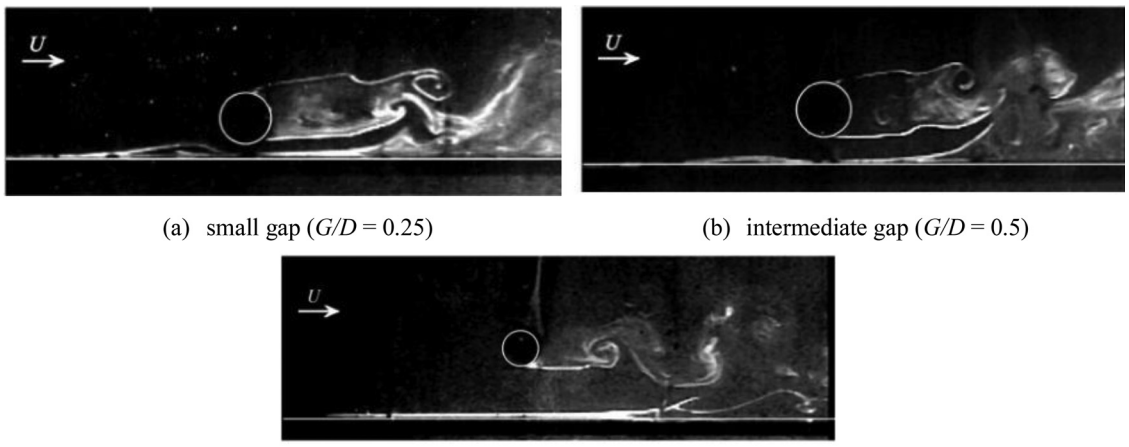

(a) small gap ($G/D = 0.25$) (b) intermediate gap ($G/D = 0.5$)

(c) largest gap ($G/D = 1.5$)

FIG. 45. Flow visualization behind a circular cylinder for $Re = 1200$–1400, (a) $G/D = 0.25$, (b) $G/D = 0.5$, and (c) $G/D = 1.5$. Reproduced with permission from Price *et al.*, J. Fluids Struct. **16**, 175–191 (2002). Copyright 2002 Elsevier.[232]

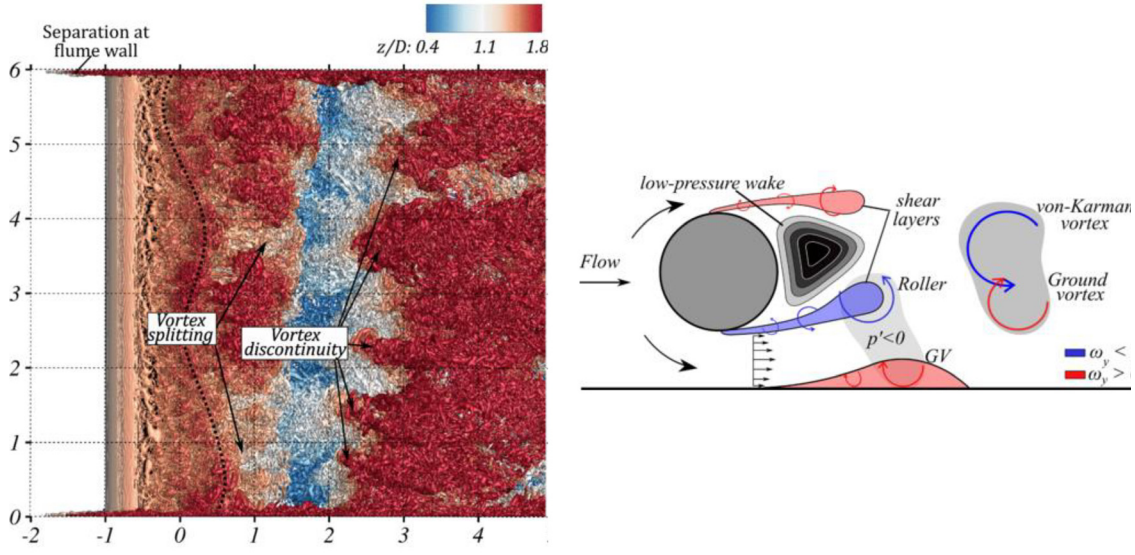

FIG. 46. (a) Top view of iso-surfaces of Q criterion ($Q^* = QD^2/U_0^2 = 21$) for $Re = 13\,333$ and $G/D = 0.5$, and (b) schematic representation of the ground vortex. Reproduced with permission from Ouro *et al.*, Phys. Rev. Fluids **4**, 104604 (2019). Copyright 2019 American Physical Society.[237]

strength of the shed vortices decrease as the gap ratio reduces for $0.6 < G/D < 0.9$. A low-speed separation bubble was found by Shi *et al.*[240] behind a square cylinder for $4.25 \leq X/D \leq 9.25$ at $G/D = 0.25$, whereas a pair of counter-rotating recirculation regions with a stable reversal flow was identified by He *et al.*[241] for $X/D < 3$ at the same gap ratio. As demonstrated in Fig. 47 by Malavasi and Blois,[242] the upper vortex behind an elongated rectangular cylinder is expanded with decreasing gap ratio, while the lower vortex seems to be compressed between the upper vortex and the solid surface. As can be seen, the supply of the fluid from the intrados is restricted for small gap ratios and is completely interrupted for $G/D = 0$, causing the disappearance of this vortex. Panigrahi[243] elucidated that the size of the recirculation bubble is reduced with an increased gap ratio and the turbulent fluctuation intensity behind the cylinder is a strong function of the gap size. Steady flow around a square cylinder near a wall at Reynolds number ranging from 73 400 to 412 000 was investigated by Yang *et al.*[244] for gap ratios up to 3 and different freestream turbulence intensities. Similar to Martinuzzi *et al.*,[239] they showed that vortex shedding is completely suppressed for $G/D \leq 0.3$. For $G/D \geq 1$, an increase in freestream turbulence intensity to 9% leads to an increased base pressure and decreased drag coefficient. However, for small gap ratios ($G/D \leq 0.6$), higher fluctuating drag and lift coefficients are observed due to the growth of separated shear layer and its inherent instabilities. It should be mentioned that the side ratio of a rectangular cylinder as well as the angle of attack were also suggested to be important factors governing the flow characteristics.[246–248] More details of experimental studies regarding near surface bluff bodies are summarized in Table VI.

C. Water free surface

Bluff body wakes in the vicinity of water free surface are a typical and fundamental problem in marine engineering. Offshore structures such as pipelines and oil platforms under the influence of water free surface may exhibit complex responses to hydrodynamic loads. Therefore, getting insight into their flow physics remains as a pressing need for efficient design of these structures.[248] Cross-flows over bluff bodies in the close proximity of water free surface are characterized by the submergence ratio (H_u/D or H_l/D, where H_u and H_l denote the distance from the bluff body's upper and lower surfaces to the free surface, respectively). Bluff bodies could be either fully or partially submerged, or placed in a cross wind completely above the water surface. Moreover, the free surface could be either steady or similar to real sea conditions accompanied by wave,[249] current,[250] or wave-current.[251,252] Herein, only bluff bodies under the steady free surface are discussed.

Sheridan *et al.*[253] revealed that when a vorticity layer generated by the uniform free surface is placed in the vicinity of the layer originated from the upper surface of cylinder, a jet-like flow is formed. By towing a partially submerged cylinder in a tow tank with submergence ratios of $H_l/D = 0.25$, 0.50, and 0.75, Ren *et al.*[254] found a non-parallel wake with decreased deflection angle with an increase in flow velocity. The jet-like flow structure was also detected by Lee[255] behind elliptic cylinders adjacent to a free surface with submergence ratios from up to $H_u/B = 0.709$ (B denotes the minor diameter of the elliptic cylinder). They also divided the near-wake region into three regimes: the formation of a Coanda flow, substantial jet-like flow generation, and jet-like flow structure attachment to the free surface. Jet-like flow topology was also identified by Lee and Daichin[256] for a circular cylinder above the water free surface with gap ratios from 0.25 to 1.25. For a circular cylinder in the air flow above the free surface of quiescent water, the lower shear layer in the air wake was pushed upward under the influence of the wind-induced water surface wave. Hence, it interacts with the upper shear layer and results in a decreased air wake width.

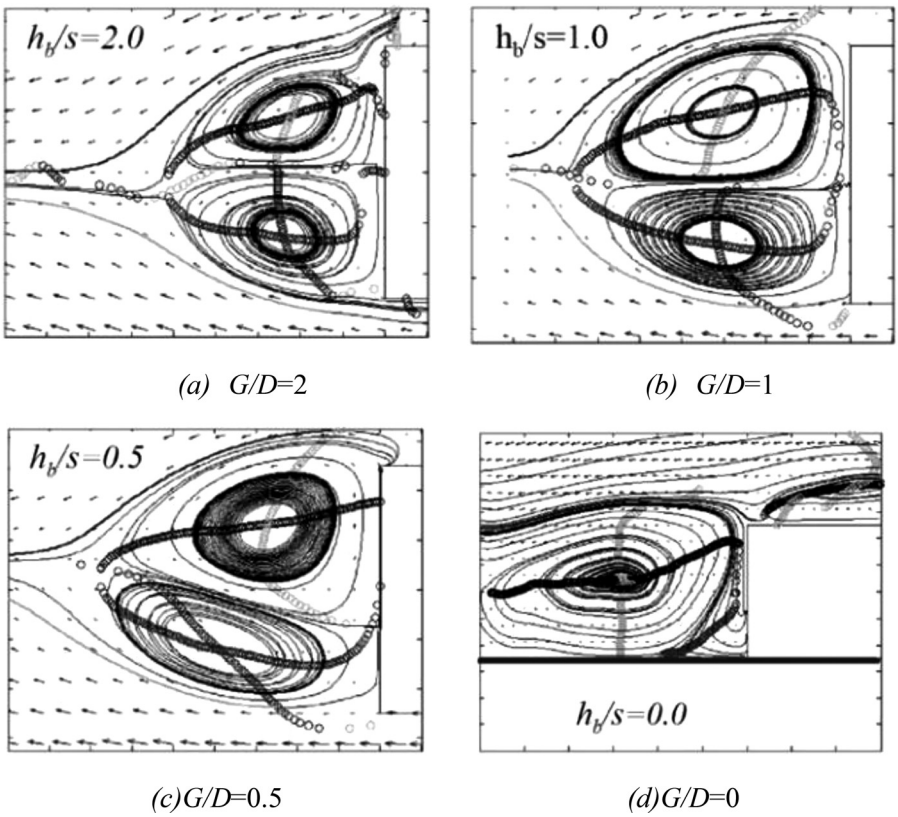

FIG. 47. Mean flow structure past an elongated rectangular cylinder for *Re* = 12 100 (a) *G/D* = 2, (b) *G/D* = 1, (c) *G/D* = 0.5, and (d) *G/D* = 0. Reproduced with permission from Malavasi and Blois, Meccanica **47**, 805–815 (2012). Copyright 2012 Springer Nature.[242]

However, with an increase in the gap ratio, the distance between the lower and upper shear layers increases and the vortex formation region becomes elongated (Fig. 48).

Simultaneous effects of the bottom rigid boundary and the upper water surface on the fluid mechanic responses behind a rectangular cylinder were analyzed by Malavasi and Guadagnini[257] for the Reynolds numbers from 12 000 to 37 000. Results indicated that the mean force coefficients and the vortex shedding frequencies are strongly affected by the asymmetric boundary configurations. Qi *et al.*[258] showed that vortex shedding at a Reynolds number of 4977 disappears when the circular cylinder touches the bottom wall or the water surface. As reported by Negri *et al.*[259] for a rectangular cylinder with a side ratio of 3 and at a Reynolds number of 10 700, the difference in the boundary types causes the wake development to be slightly asymmetric. Time-averaged and instantaneous flow field behind a circular cylinder in different submergence ratios ranging from $H_l/D = 0.25$ to $H_l/D = 2$ was visualized by Tumen Ozdil and Akilli.[260] As illustrated in Fig. 49, only one recirculation zone is conspicuously noticed for $H_L/D = 0.5$, 0.75, and 1. However, two foci and a saddle point were found for $H_L/D = 1.25$, 1.5, and 1.75. In addition, Reynolds stress and the turbulent kinetic energy are high at $H_L/D = 1.25$, 1.5, and 1.75 owing to the transfer of higher momentum from the core flow (non-vortical streamlines) region toward the wake region.

VII. EFFECTS OF NON-NEWTONIAN FLUIDS

Bluff bodies under a non-Newtonian cross-flow are frequently encountered in oil industry, blood flow pass cardiovascular valves, engineering processes of the food and many other chemical and processing industries.[261,262] In spite of the practical significance, the vortex shedding and the flow characteristics behind cylinders in non-Newtonian fluids are not well understood. Due to practical difficulties in conducting experiments with non-Newtonian fluids, most of studies in this field have been done numerically. Most studies performed experimentally have been dedicated to the creeping flow regime, which is beyond the scope of the present review.[263,264] Herein, studies focusing on the effects of fluid type on vertex shedding behaviors are discussed in detail.

In contrast to Newtonian fluids, viscosity in non-Newtonian fluids is not constant and is related to the shear rate. Using LDV and Toepler Schlieren optics, Bergins *et al.*[265] compared the flow structure behind a circular cylinder in a Newtonian fluid and in a dilute solution of the cationic surfactant C_{14} sal. According to Fig. 50, they revealed that the flow topology in the surfactant solution at a very low Reynolds number is very similar to that of the Newtonian fluid in terms of the recirculation area shape and size, the mutually detaching shear layers and the Kármán vortex shedding. However, the large-scale structure in the non-Newtonian fluid flow is rather smoother. With an increase in Reynolds number, the wake in the non-Newtonian fluid case becomes narrower and the vortex shedding is suppressed, leading to a completely steady flow. This suppression of vortex shedding was attributed to a shear-induced structure.

In comparison with Newtonian fluids, Cadot[266] proved that the frequency of vortex shedding behind a circular cylinder in a

TABLE VI. A summary of experimental studies about near surface bluff bodies.

Paper	Bluff body	*Re*	BL type/thickness (δ)	Gap ratio	TI (%)	Methodology
Lei *et al.*[230]	Circular cylinder (L1.3 × D0.05 m^2)	13 000–14 500	Turbulent 0.14D–2.89D	0–3	≈5.3	Boundary layer wind tunnel (L7.5 × W2.8 × H2.2 m^3) •Pressure transducer
Ezadi Yazdi and Bak Khoshnevis[231]	Elliptic cylinder	13 250 26 500	Fully developed turbulent δ = 0.38B	0.1–2	<0.15	(L0.39 × A0.042 2 × B0.021 2 m^3)[a] Open-circuit and blow type wind tunnel (L1.68 × W0.4 × H0.4 m^3) •HWA
Price *et al.*[232]	Circular cylinder (D0.025 4 m) (D0.016 m)	1200–4960	Laminar boundary layer 0.42D–0.46D	0–2	···	Recirculating water tunnel (W0.26 × H0.26 m^2) •Hot-film •Flow visualization Water towing tank (W0.76*0.76 m^2) •PIV
Oner *et al.*[233]	Circular cylinder (D0.05 m)	840 4150 9500	δ = 1.4D–1.6D	0–2	···	Water channel (L14 × W1 × H0.75 m^3) •PIV
Khabbouchi *et al.*[234]	Circular cylinder (D0.02 m)	8700	···	0.15–1	<0.5	Wind tunnel (W0.7 × H0.5 m^2) •PIV
Lin *et al.*[235]	Circular cylinder (L0.43 × D0.013–0.05 m^2)	7800–11 500	Laminar δ = 0.15D–1.41D	0–4	<0.8	Recirculating water channel (L3.05 × W0.5 × H0.54 m^3) •FV (particle trajectory photography) •PIV •Fiber LDV
Yang *et al.*[236]	Circular cylinder (L0.998 × D0.196 m^2)	110 000–430 000	Transition to turbulent δ = 1.28D*	0–1	4–11	Fully closed circulating water channel (L17 × W1 × H1 m^3) •ADV •Pressure transducers
Ouro *et al.*[237]	Circular cylinder (L0.3 × D0.05 m^2)	6666 10 000 13 333	···	0.5 1	···	Recirculating flume (L10 × W0.3 × H0.3 m^3) •Acoustic Doppler velocimetry
Zhou *et al.*[238]	Circular cylinder (L0.24 × D0.015 m^2)	1500	Laminar δ = 0.65D	0–2.5	1.5	Low-speed recirculation water channel (L2 × W0.25 × H0.3 m^3) •2C-PIV
Martinuzzi *et al.*[239]	Square cylinder (L0.45 × H0.03 m^2)	18 900	0.5D	0.07–1.6	1	Boundary layer wind tunnel (L1.5 × W0.45 × H0.45 m^3) •HWA •Pressure scanners •Hot-film probes
Shi *et al.*[240]	Square cylinder (H0.02 m)	13 200	Fully developed turbulent	0.25,0.5		Open-circuit wind tunnel (L2 × W0.3 × H0.3 m^3)

TABLE VI. (*Continued.*)

Paper	Bluff body	*Re*	BL type/thickness (δ)	Gap ratio	TI (%)	Methodology
			$\delta = 0.75$H			•HWA •Microphones •Split-fiber film probe
He *et al.*[241]	Square cylinder (H0.01 m)	3800 7600 11 400	Fully developed turbulent $\delta = 1.8$H–2.3H	0–0.75	<0.6	Open-circuit wind tunnel (L2 × W0.3 × H0.3 m^3) •Temperature-sensitive paint •2C-PIV
Malavasi and Blois[242]	Elongated rectangular cylinder (L0.5 × W0.18 × H0.06 m^3)	12 100	⋯	0–3	⋯	•Split fiber film probe Open water channel (L5 × W0.5 × H0.6 m^3) •Time-resolved PIV
Panigrahi[243]	Square cylinder (L0.45 × H0.015 m^2)	11 075	Turbulent $\delta = 0.2$H	0.2–1	≈0.05	Low turbulence wind tunnel (L6.25 × 1.5 × 0.3 m^3) •FV (oil film) •2-C PIV
Yang *et al.*[244]	Square cylinder (L2 × H0.2 m^2)	73 400–412 000	Turbulent $\delta = 0.2$ D	0–3	1, 9	High-speed wind tunnel (L15 × 3 × 3 m^3) •Pressure sensors
Cigada *et al.*[245]	Rectangular cylinder (L0.9 × H0.04 × W0.12, 0.16 m^3)	6000–40 000	Fully developed	0.15–5	<7	Open test section wind tunnel (0.9*0.9 m^2) •Strain-gauge force-sensing •HWA •Dynamometers
Malavasi and Zappa[246]	Rectangular cylinder (L0.55 × W0.12, 0.16 × H0.04 m^3)	13 800 19 200	⋯	0.5–5	1–2	Open chamber wind tunnel (W0.9 × H0.9 m^2) •Dynamometer •Differential pressure transducer
Choi and Lee[247]	Elliptic cylinder (L0.6 m)	13 600	Thick turbulent $\delta = 0.075$ m	0.7, 1, 1.5	<0.08	Subsonic wind tunnel (L6 × W0.72 × H0.6 m^3) •Pressure taps •HWA •Particle tracer technique

[a]A and B are the largest and smallest radii of the elliptic cylinder, respectively.

Phys. Fluids **34**, 011301 (2022); doi: 10.1063/5.0077323

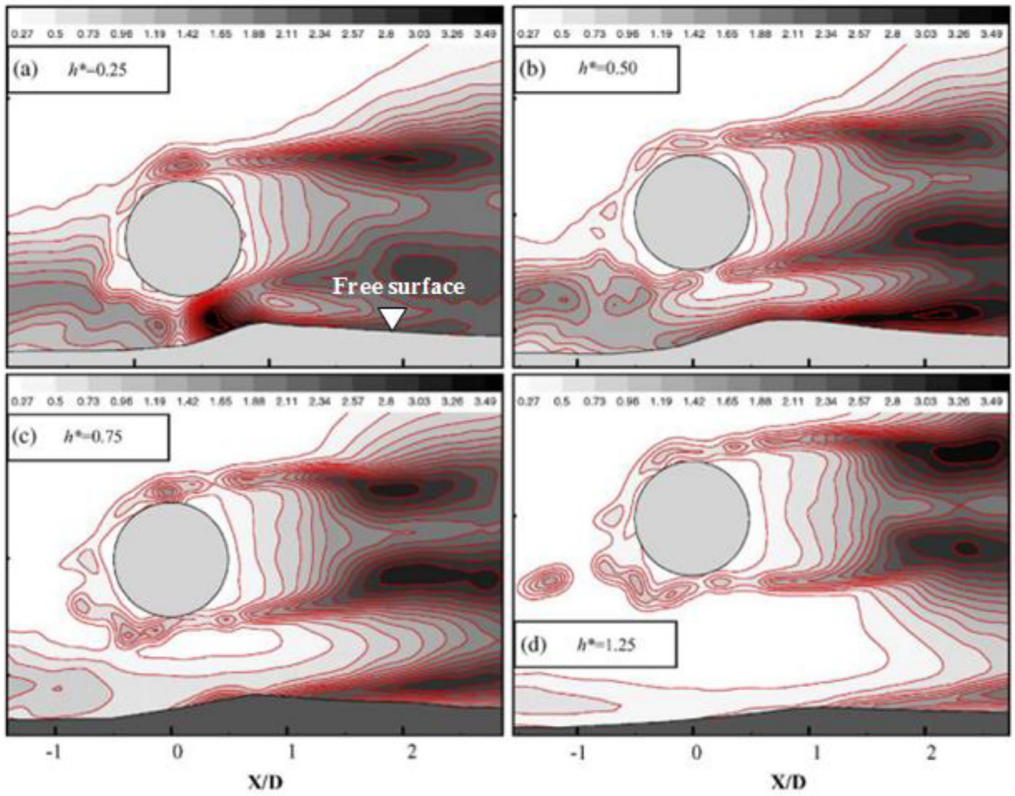

FIG. 48. Spanwise vorticity at different gap ratios for a cylinder above the free surface. Reproduced with permission from Lee and Daichin, J. Fluids Struct. **19**, 1049–1059 (2004). Copyright 2002 Elsevier.[256]

viscoelastic fluid flow (made from the dilution of polyethyleneoxide at 600 wppm in water) is reduced at a Reynolds number of 140 while the formation length increases. They also revealed that the streamlines passing through the saddle points for the Newtonian fluid case resemble a tadpole shape and collapse on one another. However, vortices in the non-Newtonian case have an elliptical shape. The effects of polymer polyethylene oxide solution (with a molecular weight of 5×10^6 and a concentration of 30 wppm) on the vortex shedding behind a circular cylinder were evaluated by Cressman *et al.*[267] at $Re = 400$. Results indicated that the rms velocity fluctuations are suppressed at

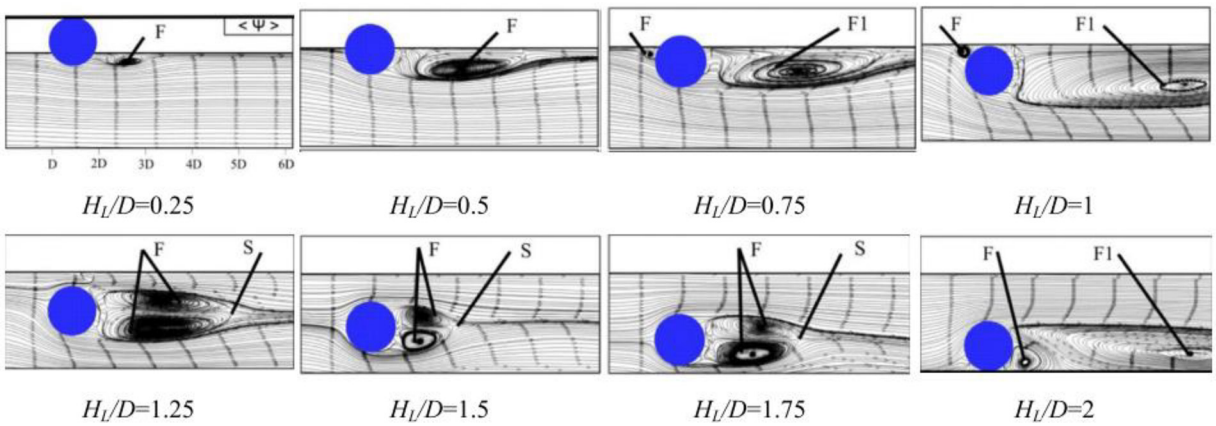

FIG. 49. Flow structure downstream of a circular cylinder at different submergence ratios. Reproduced with permission from Ozdil and Akilli, Ocean Eng. **96**, 56–67 (2015). Copyright 2015 Elsevier.[260]

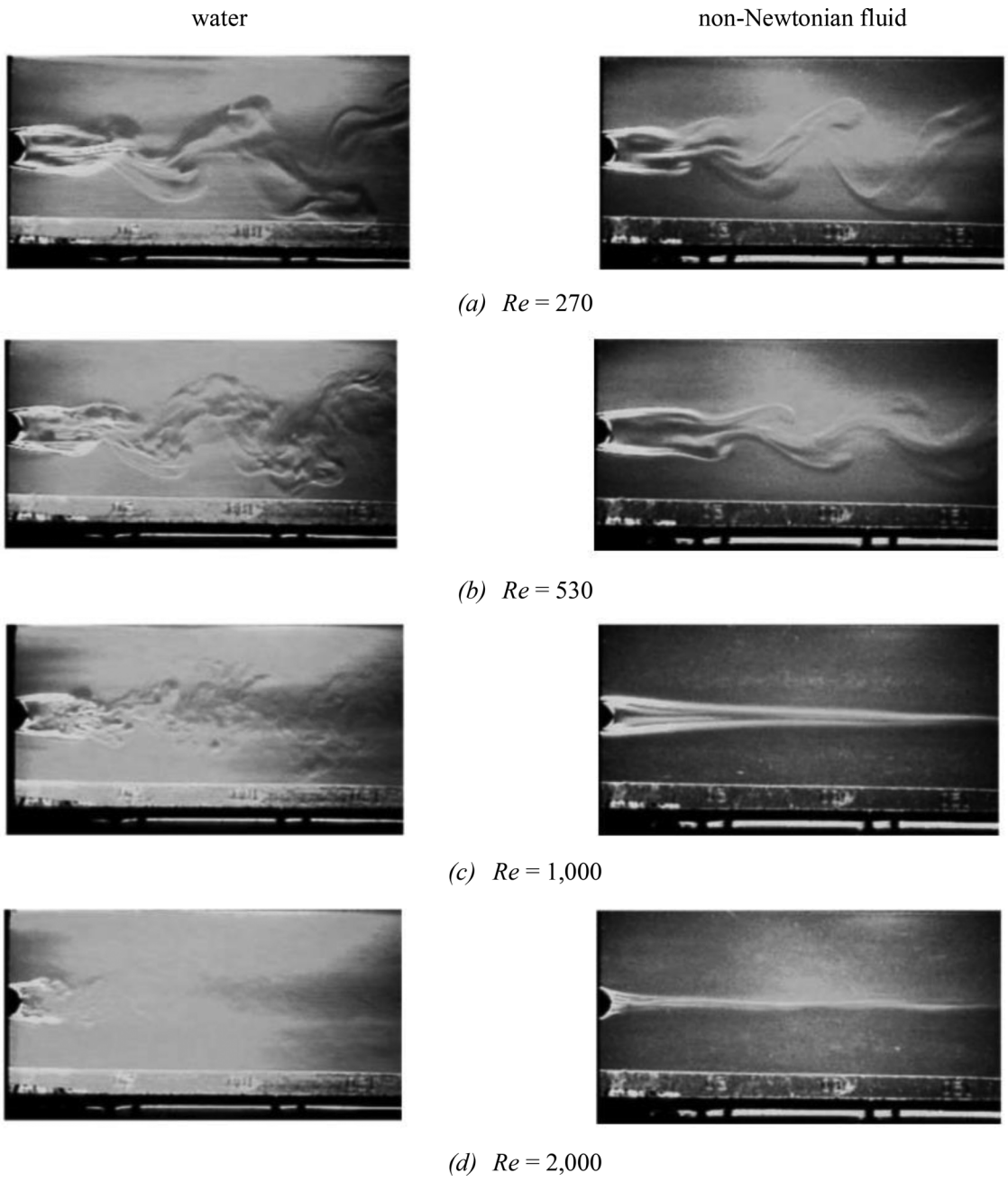

FIG. 50. Flow visualization behind a circular cylinder under water and non-Newtonian fluids (a) $Re = 270$, (b) $Re = 530$, (c) $Re = 1000$, and (d) $Re = 2000$. Reproduced with permission from Bergins *et al.*, Exp. Fluids **30**, 410–417 (2001). Copyright 2001 Springer Nature.[265]

all downstream points for low polymer concentration. Various vortex shedding regimes behind a circular cylinder were analyzed by Coelho and Pinho[268] in aqueous solutions of carboxymethyl cellulose (CMC) and tylose at different weight concentrations from 0.1% to 0.6%. It was found that the fluid elasticity results in an increase in the formation length and a decrease in the Strouhal number. Furthermore, shear-thinning causes the boundary layer to be thinner while the Strouhal number to be larger. However, the total effect of shear-thinning and elasticity is an increase in the Strouhal number.

In another study, Coelho and Pinho[269] pointed out that the wake angle, which is defined as the angle between horizontal line drawn from the base pressure coefficient and the slopping straight line fitted to pressure coefficient values in the adverse pressure gradient zone, and the pressure coefficient in the shear layer transition regime

increase with polymer concentration, resulting in lower drag due to the narrower nearfield wake. The effects of small amounts of fluid elasticity on the laminar vortex shedding behind a circular cylinder at $50 < Re < 150$ were investigated by Pipe and Monkewtiz.[270] They showed that the critical Reynolds number increases in aqueous solutions with lower polyethylene oxide concentration. This behavior was related to the higher shear rates of the flow.

VIII. CONCLUSION AND SUGGESTIONS

The main objective of this paper is to review available experimental studies in the literature on the flow physics around bluff bodies by first summarizing the classical framework of a stationary circular cylinder in an unbounded, steady, and Newtonian cross-flow. Influences of various factors on the flow features and structures are then reviewed, which include bluff body geometry, unsteady inflow condition, confinement condition, and non-Newtonian fluid. The following conclusions can be drawn:

- The classical fluid flow behind a circular cylinder experiences a number of transitions as Reynolds number increases. In the first transition, the steady wake transfers to the shedding of vortices, while in the second transition, onset of three dimensionalities occurs and different characteristics like mode A, mode B, and vortex dislocations are identified in the wake. The third transition is recognized as the Kelvin–Helmholtz instability becomes the dominant features, where the shear layer vortices form. In the last transition, two laminar separation bubbles are identified, one on each side of the cylinder surface.
- Geometrical parameters, such as cross section, side ratio, aspect ratio, corner modification, and angle of incidence, have been found to have significant effects on vortex shedding, flow characteristics, and turbulence properties. It has also been shown that spanwise variation of cylinder shape, including wavy and step changes, induces complex flow physics.
- The formation of a lock-on region, where the vortex shedding frequency shifts to the pulsation frequency or its subharmonics, is the most important phenomenon in the pulsating inflow, which has been found to usually occur at pulsation to natural shedding frequency ratio of around two. The flow behind an impulsively started cylinder can be divided into three regimes based on Reynolds number. While the formation of the main eddy, bulge, and a little secondary eddy are the features of the first and second flow regimes, respectively, the last regime is characterized by phenomena α and β. It is also shown that the uniformly accelerating or decelerating inflow has a great influence on the critical Reynolds number and the drag coefficient.
- The effects of confinement have been shown to be the increment of the Strouhal number and a delay in the critical Reynolds number. Furthermore, suppression of vortex shedding is the main characteristic of the wake behind bluff bodies in the vicinity of a rigid wall when the gap is small enough. It has also been found that when a bluff body is placed close to a water free surface, a jet-like flow is formed due to the interaction of shear layers generated from the free surface and the cylinder surface.
- Frequency of vortex shedding, formation length, Strouhal number, critical Reynolds number, and aerodynamic coefficients have all been found to be a strong dependency on the non-Newtonian fluid properties. Furthermore, the difference between the flow topology in Newtonian and non-Newtonian fluid flows appears more obvious at high Reynolds numbers.

Although most aspects of the bluff body wakes have been well understood, there are still some areas that deserve further experimental study in our opinion.

- Data on circular cylinders under supercritical and transcritical flow regimes are sparse and more investigations are called for.
- More analysis is required to understand the secondary or streamwise vortices behind D-shaped cylinders.
- There are still many types of geometries such as semi-circular cylinders or equilateral triangles with convex sides, which have not been sufficiently investigated experimentally.
- Shape variation in the spanwise direction of bluff bodies with non-circular cross sections could be worth future studies.
- Investigation of turbulence characteristics behind bluff bodies under uniformly accelerating and decelerating flows is of practical importance.
- More oscillating inflow conditions around bluff bodies could be the subject of future investigations.
- Bluff bodies confined in a divergent or a convergent channel where the blockage ratio is not constant have not been studied yet as far as we are aware.
- Confined bluff bodies in a circular pipe deserve further analysis.
- Bluff bodies in the vicinity of a non-flat surface, like a wavy or an inclined surface, could be the aims of future experiments.
- Investigations of non-circular and also inclined bluff bodies in the vicinity of a water free surface could be of interest.
- Due to the difficulties in conducting experiments in non-Newtonian fluids, the flow physics such as turbulence characteristics, fluid forces, and the flow topology particularly in high Reynolds numbers have not been sufficiently explored.
- There are many types of non-Newtonian fluids with different solution properties that are worth further study.

AUTHOR DECLARATIONS

Conflict of Interest

The authors have no conflicts to disclose.

DATA AVAILABILITY

Data sharing is not applicable to this article as no new data were created or analyzed in this study.

REFERENCES

[1]C. H. K. Williamson, "Vortex dynamics in the cylinder wake," Annu. Rev. Fluid Mech. **28**, 477–539 (1996).
[2]C. H. K. Williamson, "Three-dimensional vortex dynamics in bluff body wakes," Exp. Therm. Fluid Sci. **12**, 150–168 (1996).
[3]C. H. K. Williamson, "Advances in our understanding of vortex dynamics in bluff body wakes," J. Wind Eng. Ind. Aerodyn. **69–71**, 3–32 (1997).
[4]P. Hishikar, S. K. Dhiman, A. K. Tiwari, and V. K. Gaba, "Analysis of flow characteristics of two circular cylinders in cross-flow with varying Reynolds number: A review," J. Therm. Anal. Calorim. (published online) (2021).
[5]D. Sumner, "Two circular cylinders in cross-flow: A review," J. Fluids Struct. **26**, 849–899 (2010).
[6]J. Wang, L. Geng, L. Ding, H. Zhu, and D. Yurchenko, "The state-of-the-art review on energy harvesting from flow-induced vibrations," Appl. Energy **267**, 114902 (2020).

[7]J-s Wang, D. Fan, and K. Lin, "A review on flow-induced vibration of offshore circular cylinders," J. Hydrodyn. **32**, 415–440 (2020).
[8]D. Li, Y. Wu, A. Da Ronch, and J. Xiang, "Energy harvesting by means of flow-induced vibrations on aerospace vehicles," Prog. Aerosp. Sci. **86**, 28–62 (2016).
[9]T. Sarpkaya, "A critical review of the intrinsic nature of vortex-induced vibrations," J. Fluids Struct. **19**, 389–447 (2004).
[10]C. H. K. Williamson and R. Govardhan, "A brief review of recent results in vortex-induced vibrations," J. Wind Eng. Ind. Aerodyn. **96**, 713–735 (2008).
[11]X. Wu, F. Ge, and Y. Hong, "A review of recent studies on vortex-induced vibrations of long slender cylinders," J. Fluids Struct. **28**, 292–308 (2012).
[12]M. M. Zdravkovich, *Flow Around Circular Cylinders: Volume 2: Applications* (Oxford University Press, 1997).
[13]H. Bénard, "Formation de centres de giration à l'arrière d'un obstacle en movement," C. R. Acad. Sci. **147**, 839–842 (1908).
[14]T. Von Kármán, "Über den mechanismus des widerstandes, den ein bewegter körper in einer flüssigkeit erfährt," Nachr. Gesells. Wiss. Göttingen **1911**, 509–517.
[15]M. Matsumoto, "Vortex shedding of bluff bodies: A review," J. Fluids Struct. **13**, 791–811 (1999).
[16]J. C. R. Hunt, H. Kawai, S. R. Ramsey, G. Pedrizetti, and R. J. Perkins, "A review of velocity and pressure fluctuations in turbulent flows around bluff bodies," J. Wind Eng. Ind. Aerodyn. **35**, 49–85 (1990).
[17]C. Norberg, "Fluctuating lift on a circular cylinder: Review and new measurements," J. Fluids Struct. **17**, 57–96 (2003).
[18]J. F. Derakhshandeh and M. M. Alam, "A review of bluff body wakes," Ocean Eng. **182**, 475–488 (2019).
[19]M. C. Thompson, T. Leweke, and K. Hourigan, "Bluff bodies and wake–wall interactions," Annu. Rev. Fluid Mech. **53**, 347–376 (2021).
[20]L. N. Cattafesta III and M. Sheplak, "Actuators for active flow control," Annu. Rev. Fluid Mech. **43**, 247–272 (2011).
[21]S. Rashidi, M. Hayatdavoodi, and J. A. Esfahani, "Vortex shedding suppression and wake control: A review," Ocean Eng. **126**, 57–80 (2016).
[22]D.-L. Gao, W.-L. Chen, H. Li, and H. Hu, "Flow around a slotted circular cylinder at various angles of attack," Exp. Fluids **58**, 132 (2017).
[23]D.-L. Gao, W.-L. Chen, H. Li, and H. Hu, "Flow around a circular cylinder with slit," Exp. Therm. Fluid Sci. **82**, 287–301 (2017).
[24]R. Woszidlo, F. Ostermann, and H.-J. Schmidt, "Fundamental properties of fluidic oscillators for flow control applications," AIAA J. **57**, 978–992 (2019).
[25]A. Mehraban, M. Djavareshkian, Y. Sayegh, B. Forouzi Feshalami, Y. Azargoon, A. Zaree, and M. Hassanalian, "Effects of smart flap on aerodynamic performance of sinusoidal leading-edge wings at low Reynolds numbers," Proc. Inst. Mech. Eng. Part G **235**, 439–450 (2021).
[26]C. Tropea, A. L. Yarin, and J. F. Foss, *Springer Handbook of Experimental Fluid Mechanics* (Springer, 2007).
[27]A. J. Smits and T. T. Lim, *Flow Visualization: Techniques and Examples* (Imperial College Press, 2012).
[28]B. Chanetz, J. Délery, P. Gilliéron, P. Gnemmi, E. R. Gowree, and P. Perrier, *Experimental Aerodynamics* (Springer, 2020).
[29]C. Morton and S. Yarusevych, "Three-dimensional flow and surface visualization using hydrogen bubble technique," J. Visualization **18**, 47–58 (2015).
[30]M. Matsumoto, H. Shirato, K. Araki, T. Haramura, and T. Hashimoto, "Spanwise coherence characteristics of surface pressure field on 2-D bluff bodies," J. Wind Eng. Ind. Aerodyn. **91**, 155–163 (2003).
[31]M. M. Alam and Y. Zhou, "Turbulent wake of an inclined cylinder with water running," J. Fluid Mech. **589**, 261–303 (2007).
[32]W.-L. Chen, D.-L. Gao, W.-Y. Yuan, H. Li, and H. Hu, "Passive jet control of flow around a circular cylinder," Exp. Fluids **56**, 201 (2015).
[33]S. Li and M. Li, "Spectral analysis and coherence of aerodynamic lift on rectangular cylinders in turbulent flow," J. Fluid Mech. **830**, 408–438 (2017).
[34]S. Discetti and A. Ianiro, *Experimental Aerodynamics* (CRC Press, 2017).
[35]J. D. Hooper and A. R. Musgrove, "Reynolds stress, mean velocity, and dynamic static pressure measurement by a four-hole pressure probe," Exp. Therm. Fluid Sci. **15**, 375–383 (1997).
[36]J. Chen, B. S. Haynes, and D. F. Fletcher, "Cobra probe measurements of mean velocities, Reynolds stresses and higher-order velocity correlations in pipe flow," Exp. Therm. Fluid Sci. **21**, 206–217 (2000).
[37]Y. Xue, M. Arjomandi, and R. Kelso, "Experimental study of the thermal separation in a vortex tube," Exp. Therm. Fluid Sci. **46**, 175–182 (2013).
[38]Y. Guo and D. H. Wood, "Instantaneous velocity and pressure measurements in turbulent mixing layers," Exp. Therm. Fluid Sci. **24**, 139–150 (2001).
[39]K. M. Argüelles Díaz, J. M. Fernández Oro, and E. Blanco Marigorta, "Extended angular range of a three-hole cobra pressure probe for incompressible flow," J. Fluids Eng. **130**, 101401 (2008).
[40]Z. Zhang, *LDA Application Methods: Laser Doppler Anemometry for Fluid Dynamics* (Springer, 2010).
[41]B. J. Cantwell, "A flying hot wire study of the turbulent near wake of a circular cylinder at a Reynolds number of 140 000, Ph.D. dissertation (California Institute of Technology, 1976).
[42]J. S. Wilson, *Sensor Technology Handbook* (Elsevier, 2004).
[43]M. Raffel, C. E. Willert, F. Scarano, C. J. Kähler, S. T. Wereley, and J. Kompenhans, *Particle Image Velocimetry: A Practical Guide* (Springer, 2018).
[44]J.-H. Yoon and S.-J. Lee, "Direct comparison of 2D PIV and stereoscopic PIV measurements," Meas. Sci. Technol. **13**, 1631–1642 (2002).
[45]Z. Liu, Y. Zheng, L. Jia, J. Jiao, and Q. Zhang, "Stereoscopic PIV studies on the swirling flow structure in a gas cyclone," Chem. Eng. Sci. **61**, 4252–4261 (2006).
[46]G. E. Elsinga, F. Scarano, B. Wieneke, and B. W. van Oudheusden, "Tomographic particle image velocimetry," Exp. Fluids **41**, 933–947 (2006).
[47]D. Schanz, S. Gesemann, and A. Schröder, "Shake-The-Box: Lagrangian particle tracking at high particle image densities," Exp. Fluids **57**, 70 (2016).
[48]M. P. Rockwood and M. A. Green, "Real-time identification of vortex shedding in the wake of a circular cylinder," AIAA J. **57**, 223–238 (2019).
[49]A. Roshko, "Perspectives on bluff body aerodynamics," J. Wind Eng. Ind. Aerodyn. **49**, 79–100 (1993).
[50]O. Cadot, A. Desai, S. Mittal, S. Saxena, and B. Chandra, "Statistics and dynamics of the boundary layer reattachments during the drag crisis transitions of a circular cylinder," Phys. Fluids **27**, 014101 (2015).
[51]A. Desai, S. Mittal, and S. Mittal, "Experimental investigation of vortex shedding past a circular cylinder in the high subcritical regime," Phys. Fluids **32**, 014105 (2020).
[52]T. Lee and R. Budwig, "A study of the effect of aspect ratio on vortex shedding behind circular cylinders," Phys. Fluids A **3**, 309–315 (1991).
[53]S. Szepessy and P. W. Bearman, "Aspect ratio and end plate effects on vortex shedding from a circular cylinder," J. Fluid Mech. **234**, 191–217 (1992).
[54]C. Norberg, "An experimental investigation of the flow around a circular cylinder: Influence of aspect ratio," J. Fluid Mech. **258**, 287–316 (1994).
[55]W. Ma, B. Huang, D. Zheng, M. Lu, and H. Li, "Effect of the presence of end plates and aspect ratio on the aerodynamic forces on circular cylinders in various flow regimes," Fluid Dyn. Res. **51**, 055503 (2019).
[56]A. E. Perry, M. S. Chong, and T. T. Lim, "The vortex-shedding process behind two-dimensional bluff bodies," J. Fluid Mech. **116**, 77–90 (1982).
[57]M. Coutanceau and R. Bouard, "Experimental determination of the main features of the viscous flow in the wake of a circular cylinder in uniform translation. Part 1. Steady flow," J. Fluid Mech. **79**, 231–256 (1977).
[58]A. Goharzadeh and A. Molki, "Measurement of fluid velocity development behind a circular cylinder using particle image velocimetry (PIV)," Eur. J. Phys. **36**, 015001 (2015).
[59]B. Gibeau and S. Ghaemi, "The mode B structure of streamwise vortices in the wake of a two-dimensional blunt trailing edge," J. Fluid Mech. **884**, A12 (2020).
[60]H. Schlichting and K. Gersten, *Boundary-Layer Theory* (Springer, 2016).
[61]T. Karasudani and M. Funakoshi, "Evolution of a vortex street in the far wake of a cylinder," Fluid Dyn. Res. **14**, 331 (1994).
[62]P. Vorobieff, D. Georgiev, and M. S. Ingber, "Onset of the second wake: Dependence on the Reynolds number," Phys. Fluids **14**, L53–L56 (2002).
[63]C. Lin and S.-C. Hsieh, "Convection velocity of vortex structures in the near wake of a circular cylinder," J. Eng. Mech. **129**, 1108–1118 (2003).
[64]T. Leweke and C. H. K. Williamson, "Three-dimensional instabilities in wake transition," Eur. J. Mech. B Fluids **17**, 571–586 (1998).
[65]B. Gibeau, C. R. Koch, and S. Ghaemi, "Secondary instabilities in the wake of an elongated two-dimensional body with a blunt trailing edge," J. Fluid Mech. **846**, 578–604 (2018).

[66]M. Brede, H. Eckelmann, and D. Rockwell, "On secondary vortices in the cylinder wake," Phys. Fluids **8**, 2117–2124 (1996).
[67]J. H. Gerrard, "The wakes of cylindrical bluff bodies at low Reynolds number," Philos. Trans. R. Soc. London, Ser. A **288**, 351–382 (1978).
[68]H. Q. Zhang, U. Fey, B. R. Noack, M. König, and H. Eckelmann, "On the transition of the cylinder wake," Phys. Fluids **7**, 779–794 (1995).
[69]C. H. K. Williamson, "The natural and forced formation of spot-like 'vortex dislocations' in the transition of a wake," J. Fluid Mech. **243**, 393–441 (1992).
[70]J. Wu, J. Sheridan, K. Hourigan, and J. Soria, "Shear layer vortices and longitudinal vortices in the near wake of a circular cylinder," Exp. Therm. Fluid Sci. **12**, 169–174 (1996).
[71]T. Wei and C. R. Smith, "Secondary vortices in the wake of circular cylinders," J. Fluid Mech. **169**, 513–533 (1986).
[72]C. H. K. Williamson, J. Wu, and J. Sheridan, "Scaling of streamwise vortices in wakes," Phys. Fluids **7**, 2307–2309 (1995).
[73]J. Soria, "An investigation of the near wake of a circular cylinder using a video-based digital cross-correlation particle image velocimetry technique," Exp. Therm. Fluid Sci. **12**, 221–233 (1996).
[74]J. Wu, J. Sheridan, M. C. Welsh, and K. Hourigan, "Three-dimensional vortex structures in a cylinder wake," J. Fluid Mech. **312**, 201–222 (1996).
[75]A. Prasad and C. H. Williamson, "Three-dimensional effects in turbulent bluff body wakes," Exp. Therm. Fluid Sci. **14**, 9–16 (1997).
[76]M. König, H. Eisenlohr, and H. Eckelmann, "The fine structure in the Strouhal–Reynolds number relationship of the laminar wake of a circular cylinder," Phys. Fluids A **2**, 1607–1614 (1990).
[77]D. R. Williams, H. Mansy, and A. Abouel-Fotouh, "Three-dimensional subharmonic waves during transition in the near-wake region of a cylinder," Phys. Fluids **8**, 1476–1485 (1996).
[78]C. H. K. Williamson, *Three-Dimensional Wake Transition* (Springer, Dordrecht, 1996).
[79]A. Roshko, *On the Drag and Shedding Frequency of Two-Dimensional Bluff Bodies* (NACA, 1954).
[80]D. Barkley and R. D. Henderson, "Three-dimensional Floquet stability analysis of the wake of a circular cylinder," J. Fluid Mech. **322**, 215–241 (1996).
[81]H. M. Blackburn and J. M. Lopez, "On three-dimensional quasiperiodic Floquet instabilities of two-dimensional bluff body wakes," Phys. Fluids **15**, L57–L60 (2003).
[82]H. M. Blackburn, F. Marques, and J. M. Lopez, "Symmetry breaking of two-dimensional time-periodic wakes," J. Fluid Mech. **522**, 395–411 (2005).
[83]J. Sung and J. Y. Yoo, "Near-wake vortex motions behind a circular cylinder at low Reynolds number," J. Fluids Struct. **17**, 261–274 (2003).
[84]F. Scarano and C. Poelma, "Three-dimensional vorticity patterns of cylinder wakes," Exp. Fluids **47**, 69 (2009).
[85]S. Rajagopalan and R. A. Antonia, "Flow around a circular cylinder—Structure of the near wake shear layer," Exp. Fluids **38**, 393–402 (2005).
[86]D. Gkiolas, P. Kapiris, and D. Mathioulakis, "Experimental study of the near wake of a circular cylinder and its detached shear layers," Exp. Therm. Fluid Sci. **113**, 110040 (2020).
[87]M. F. Unal and D. Rockwell, "The role of shear layer stability in vortex shedding from cylinders," Phys. Fluids **27**, 2598–2599 (1984).
[88]M. F. Unal and D. Rockwell, "On vortex formation from a cylinder. Part 1. The initial instability," J. Fluid Mech. **190**, 491–512 (1988).
[89]C. Chyu and D. Rockwell, "Evolution of patterns of streamwise vorticity in the turbulent near wake of a circular cylinder," J. Fluid Mech. **320**, 117–137 (1996).
[90]J. C. Lin, P. Vorobieff, and D. Rockwell, "Three-dimensional patterns of streamwise vorticity in the turbulent near-wake of a cylinder," J. Fluids Struct. **9**, 231–234 (1995).
[91]J. C. Lin, P. Vorobieff, and D. Rockwell, "Space–time imaging of a turbulent near-wake by high-image-density particle image cinematography," Phys. Fluids **8**, 555–564 (1996).
[92]M. P. Rockwood, K. Taira, and M. A. Green, "Detecting vortex formation and shedding in cylinder wakes using Lagrangian coherent structures," AIAA J. **55**, 15–23 (2017).
[93]M. Khor, J. Sheridan, M. C. Thompson, and K. Hourigan, "Global frequency selection in the observed time-mean wakes of circular cylinders," J. Fluid Mech. **601**, 425–441 (2008).
[94]I. Khabbouchi, H. Fellouah, M. Ferchichi, and M. S. Guellouz, "Effects of free-stream turbulence and Reynolds number on the separated shear layer from a circular cylinder," J. Wind Eng. Ind. Aerodyn. **135**, 46–56 (2014).
[95]H. M. Blackburn and W. H. Melbourne, "The effect of free-stream turbulence on sectional lift forces on a circular cylinder," J. Fluid Mech. **306**, 267–292 (1996).
[96]H. Nishimura and Y. Taniike, "Aerodynamic characteristics of fluctuating forces on a circular cylinder," J. Wind Eng. Ind. Aerodyn. **89**, 713–723 (2001).
[97]R. Maryami, S. A. S. Ali, M. Azarpeyvand, and A. Afshari, "Turbulent flow interaction with a circular cylinder," Phys. Fluids **32**, 015105 (2020).
[98]M. Brede, "Measurement of turbulence production in the cylinder separated shear-layer using event-triggered laser-Doppler anemometry," Exp. Fluids **36**, 860–866 (2004).
[99]H. Djeridi, M. Braza, R. Perrin, G. Harran, E. Cid, and S. Cazin, "Near-wake turbulence properties around a circular cylinder at high Reynolds number," Flow Turbul. Combust. **71**, 19–34 (2003).
[100]C. Norberg, "LDV-measurements in the near wake of a circular cylinder," ASME Paper No. FEDSM98-521, 1998.
[101]M. Braza, R. Perrin, and Y. Hoarau, "Turbulence properties in the cylinder wake at high Reynolds numbers," J. Fluids Struct. **22**, 757–771 (2006).
[102]T. Zhou, S. F. M. Razali, Y. Zhou, L. P. Chua, and L. Cheng, "Dependence of the wake on inclination of a stationary cylinder," Exp. Fluids **46**, 1125–1138 (2009).
[103]A. Kozakiewicz, J. Fredsee, and B. M. Sumer, *Forces on Pipelines in Oblique Attack: Steady Current and Waves* (International Society of Offshore and Polar Engineers, 1995).
[104]L. Najafi, E. Firat, and H. Akilli, "Time-averaged near-wake of a yawed cylinder," Ocean Eng. **113**, 335–349 (2016).
[105]G. Schewe, "On the force fluctuations acting on a circular cylinder in crossflow from subcritical up to transcritical Reynolds numbers," J. Fluid Mech. **133**, 265–285 (1983).
[106]G. Chopra and S. Mittal, "The intermittent nature of the laminar separation bubble on a cylinder in uniform flow," Comput. Fluids **142**, 118–127 (2017).
[107]J. J. Miau, C. H. Fang, M. C. Chen, C. T. Wang, and Y. H. Lai, "Discrete transition of flow over a circular cylinder at precritical Reynolds numbers," AIAA J. **52**, 2576–2586 (2014).
[108]Y. Qiu, Y. Sun, Y. Wu, and Y. Tamura, "Analyzing the fluctuating pressures acting on a circular cylinder using stochastic decomposition," J. Fluids Struct. **50**, 512–527 (2014).
[109]M. Miozzi, A. Capone, F. D. Felice, C. Klein, and T. Liu, "Global and local skin friction diagnostics from TSP surface patterns on an underwater cylinder in crossflow," Phys. Fluids **28**, 124101 (2016).
[110]A. Capone, C. Klein, F. D. Felice, and M. Miozzi, "Phenomenology of a flow around a circular cylinder at sub-critical and critical Reynolds numbers," Phys. Fluids **28**, 074101 (2016).
[111]Y.-J. Lin, J.-J. Miau, J.-K. Tu, and H.-W. Tsai, "Nonstationary, three-dimensional aspects of flow around circular cylinder at critical Reynolds numbers," AIAA J. **49**, 1857–1870 (2011).
[112]D. A. Lyn, S. Einav, W. Rodi, and J.-H. Park, "A laser-Doppler velocimetry study of ensemble-averaged characteristics of the turbulent near wake of a square cylinder," J. Fluid Mech. **304**, 285–319 (1995).
[113]D. F. G. Durão, M. V. Heitor, and J. C. F. Pereira, "Measurements of turbulent and periodic flows around a square cross-section cylinder," Exp. Fluids **6**, 298–304 (1988).
[114]S. C. Luo, Y. T. Chew, and Y. T. Ng, "Characteristics of square cylinder wake transition flows," Phys. Fluids **15**, 2549–2559 (2003).
[115]A. Dobre and H. Hangan, "Investigation of the three-dimensional intermediate wake topology for a square cylinder at high Reynolds number," Exp. Fluids **37**, 518–530 (2004).
[116]J. Yu, L.-L. Shi, W.-Z. Wang, and Y.-Z. Liu, "Conditional averaging of TR-PIV measurements of wake behind square cylinder using an improved cross-correlation approach," J. Hydrodyn. **22**, 29–34 (2010).
[117]M. Minguez, C. Brun, R. Pasquetti, and E. Serre, "Experimental and high-order LES analysis of the flow in near-wall region of a square cylinder," Int. J. Heat Fluid Flow **32**, 558–566 (2011).

[118]C. H. K. Williamson, "Three-dimensional wake transition," J. Fluid Mech. **328**, 345–407 (1996).
[119]J. Robichaux, S. Balachandar, and S. P. Vanka, "Three-dimensional Floquet instability of the wake of square cylinder," Phys. Fluids **11**, 560–578 (1999).
[120]G. J. Sheard, M. J. Fitzgerald, and K. Ryan, "Cylinders with square cross-section: Wake instabilities with incidence angle variation," J. Fluid Mech. **630**, 43–69 (2009).
[121]D.-H. Yoon, K.-S. Yang, and C.-B. Choi, "Flow past a square cylinder with an angle of incidence," Phys. Fluids **22**, 043603 (2010).
[122]X. H. Tong, S. C. Luo, and B. C. Khoo, "Transition phenomena in the wake of an inclined square cylinder," J. Fluids Struct. **24**, 994–1005 (2008).
[123]A. Saha, K. Muralidhar, and G. Biswas, "Experimental study of flow past a square cylinder at high Reynolds numbers," Exp. Fluids **29**, 553–563 (2000).
[124]G. Wang, *Large Eddy Simulations of Bluff-Body Wakes on Parallel Computers* (University of Illinois at Urbana-Champaign, 1996).
[125]D. Kurtulus, F. Scarano, and L. David, "Unsteady aerodynamic forces estimation on a square cylinder by TR-PIV," Exp. Fluids **42**, 185–196 (2007).
[126]M. S. Bloor, "The transition to turbulence in the wake of a circular cylinder," J. Fluid Mech. **19**, 290–304 (1964).
[127]A. Prasad and C. H. Williamson, "The instability of the shear layer separating from a bluff body," J. Fluid Mech. **333**, 375–402 (1997).
[128]D. C. Lander, D. M. Moore, C. W. Letchford, and M. Amitay, "Scaling of square-prism shear layers," J. Fluid Mech. **849**, 1096–1119 (2018).
[129]C. Zhao, H. Wang, L. Zeng, M. M. Alam, and X. Zhao, "Effects of oncoming flow turbulence on the near wake and forces of a 3D square cylinder," J. Wind Eng. Ind. Aerodyn. **214**, 104674 (2021).
[130]S. Dutta, P. K. Panigrahi, and K. Muralidhar, "Experimental investigation of flow past a square cylinder at an angle of incidence," J. Eng. Mech. **134**, 788–803 (2008).
[131]B. W. van Oudheusden, F. Scarano, N. P. van Hinsberg, and E. W. M. Roosenboom, "Quantitative visualization of the flow around a square-section cylinder at incidence," J. Wind Eng. Ind. Aerodyn. **96**, 913–922 (2008).
[132]R. F. Huang, B. H. Lin, and S. C. Yen, "Time-averaged topological flow patterns and their influence on vortex shedding of a square cylinder in crossflow at incidence," J. Fluids Struct. **26**, 406–429 (2010).
[133]S. Dutta, K. Muralidhar, and P. Panigrahi, "Influence of the orientation of a square cylinder on the wake properties," Exp. Fluids **34**, 16–23 (2003).
[134]B. W. v Oudheusden, F. Scarano, N. P. v Hinsberg, and D. W. Watt, "Phase-resolved characterization of vortex shedding in the near wake of a square-section cylinder at incidence," Exp. Fluids **39**, 86–98 (2005).
[135]S. C. Yen and C. W. Yang, "Flow patterns and vortex shedding behavior behind a square cylinder," J. Wind Eng. Ind. Aerodyn. **99**, 868–878 (2011).
[136]X. Lou, T. Zhou, Y. Zhou, H. Wang, and L. Cheng, "Experimental investigation on wake characteristics behind a yawed square cylinder," J. Fluids Struct. **61**, 274–294 (2016).
[137]L. Carassale, A. Freda, and M. Marrè-Brunenghi, "Experimental investigation on the aerodynamic behavior of square cylinders with rounded corners," J. Fluids Struct. **44**, 195–204 (2014).
[138]N. P. van Hinsberg, G. Schewe, and M. Jacobs, "Experiments on the aerodynamic behaviour of square cylinders with rounded corners at Reynolds numbers up to 12 million," J. Fluids Struct. **74**, 214–233 (2017).
[139]N. P. van Hinsberg, G. Schewe, and M. Jacobs, "Experimental investigation on the combined effects of surface roughness and corner radius for square cylinders at high Reynolds numbers up to 10^7," J. Wind Eng. Ind. Aerodyn. **173**, 14–27 (2018).
[140]J. C. Hu and Y. Zhou, "Aerodynamic characteristics of asymmetric bluff bodies," J. Fluids Eng. **131**, 011206 (2008).
[141]Z. J. Taylor, G. A. Kopp, and R. Gurka, "Distribution of spanwise enstrophy in the near wake of three symmetric elongated bluff bodies at high Reynolds number," Phys. Fluids **25**, 055103 (2013).
[142]S. Nakagawa, K. Nitta, and M. Senda, "An experimental study on unsteady turbulent near wake of a rectangular cylinder in channel flow," Exp. Fluids **27**, 284–294 (1999).
[143]E. Deri, M. Braza, E. Cid, S. Cazin, D. Michaelis, and C. Degouet, "Investigation of the three-dimensional turbulent near-wake structure past a flat plate by tomographic PIV at high Reynolds number," J. Fluids Struct. **47**, 21–30 (2014).
[144]D. M. Moore, C. W. Letchford, and M. Amitay, "Energetic scales in a bluff body shear layer," J. Fluid Mech. **875**, 543–575 (2019).
[145]M. Gu, X. Wang, and Y. Quan, "Wind tunnel test study on effects of chamfered corners on the aerodynamic characteristics of 2D rectangular prisms," J. Wind Eng. Ind. Aerodyn. **204**, 104305 (2020).
[146]Y.-Z. Xu, L.-H. Feng, and J.-J. Wang, "Experimental investigation on the flow over normal flat plates with various corner shapes," J. Turbul. **16**, 607–616 (2015).
[147]Z. J. Taylor, E. Palombi, R. Gurka, and G. A. Kopp, "Features of the turbulent flow around symmetric elongated bluff bodies," J. Fluids Struct. **27**, 250–265 (2011).
[148]A. Naghib-Lahouti, P. Lavoie, and H. Hangan, "Wake instabilities of a blunt trailing edge profiled body at intermediate Reynolds numbers," Exp. Fluids **55**, 1779 (2014).
[149]K. Ryan, M. C. Thompson, and K. Hourigan, "Three-dimensional transition in the wake of bluff elongated cylinders," J. Fluid Mech. **538**, 1–29 (2005).
[150]Z. R. Shu and Q. S. Li, "An experimental investigation of surface pressures in separated and reattaching flows: Effects of freestream turbulence and leading edge geometry," J. Wind Eng. Ind. Aerodyn. **165**, 58–66 (2017).
[151]A. Naghib-Lahouti, L. S. Doddipatla, and H. Hangan, "Secondary wake instabilities of a blunt trailing edge profiled body as a basis for flow control," Exp. Fluids **52**, 1547–1566 (2012).
[152]S. J. Wu, J. J. Miau, C. C. Hu, and J. H. Chou, "On low-frequency modulations and three-dimensionality in vortex shedding behind a normal plate," J. Fluid Mech. **526**, 117–146 (2005).
[153]N. Agrwal, S. Dutta, and B. K. Gandhi, "Experimental investigation of flow field behind triangular prisms at intermediate Reynolds number with different apex angles," Exp. Therm. Fluid Sci. **72**, 97–111 (2016).
[154]Z. Y. Ng, T. Vo, and G. J. Sheard, "Stability of the wakes of cylinders with triangular cross-sections," J. Fluid Mech. **844**, 721–745 (2018).
[155]L. Sun, Y. Huang, X. Wang, X. Feng, and W. Xiao, "High frequency characteristics of the near wake and vortex past a triangular cylinder," J. Fluids Eng. **143**, 031204 (2020).
[156]Q. Wang, L. Gan, S. Xu, and Y. Zhou, "Vortex evolution in the near wake behind polygonal cylinders," Exp. Therm. Fluid Sci. **110**, 109940 (2020).
[157]S. J. Xu, W. G. Zhang, L. Gan, M. G. Li, and Y. Zhou, "Experimental study of flow around polygonal cylinders," J. Fluid Mech. **812**, 251–278 (2017).
[158]Q.-Y. Wang, S.-J. Xu, L. Gan, W.-G. Zhang, and Y. Zhou, "Scaling of the time-mean characteristics in the polygonal cylinder near-wake," Exp. Fluids **60**, 181 (2019).
[159]I. P. Castro and L. Watson, "Vortex shedding from tapered, triangular plates: Taper and aspect ratio effects," Exp. Fluids **37**, 159–167 (2004).
[160]J. Visscher, B. Pettersen, and H. I. Andersson, "Experimental study on the wake behind tapered circular cylinders," J. Fluids Struct. **27**, 1228–1237 (2011).
[161]W. Zhang, Daichin, and S. J. Lee, "PIV measurements of the near-wake behind a sinusoidal cylinder," Exp. Fluids **38**, 824–832 (2005).
[162]A. Ahmed and B. Bays-Muchmore, "Transverse flow over a wavy cylinder," Phys. Fluids A **4**, 1959–1967 (1992).
[163]A. Ahmed, M. J. Khan, and B. Bays-Muchmore, "Experimental investigation of a three-dimensional bluff-body wake," AIAA J. **31**, 559–563 (1993).
[164]F. H. Wang, G. D. Jiang, and K. Lam, "Flow patterns of cross-flow around a varicose cylinder," J. Visualization **8**, 49–56 (2005).
[165]K. Lam, F. H. Wang, and R. M. C. So, "Three-dimensional nature of vortices in the near wake of a wavy cylinder," J. Fluids Struct. **19**, 815–833 (2004).
[166]K. Lam and Y. F. Lin, "Effects of wavelength and amplitude of a wavy cylinder in cross-flow at low Reynolds numbers," J. Fluid Mech. **620**, 195–220 (2009).
[167]F. H. Wang, G. D. Jiang, and K. Lam, "A study of velocity fields in the near wake of a wavy (varicose) cylinder by LDA," Flow Meas. Instrum. **15**, 105–110 (2004).
[168]S.-J. Lee and A.-T. Nguyen, "Experimental investigation on wake behind a wavy cylinder having sinusoidal cross-sectional area variation," Fluid Dyn. Res. **39**, 292–304 (2007).
[169]T. New, S. Shi, and Y. Liu, "Cylinder-wall interference effects on finite-length wavy cylinders at subcritical Reynolds number flows," Exp. Fluids **54**, 1601 (2013).

[170]T. H. New, S. Shi, and Y. Liu, "On the flow behaviour of confined finite-length wavy cylinders," J. Fluids Struct. **54**, 281–296 (2015).
[171]L. S. Doddipatla, H. Hangan, V. Durgesh, and J. Naughton, "Wake dynamics resulting from trailing-edge spanwise sinusoidal perturbation," AIAA J. **55**, 1833–1851 (2017).
[172]H. Bai, B. Zang, and T. New, "The near wake of a sinusoidal wavy cylinder with a large spanwise wavelength using time-resolved particle image velocimetry," Exp. Fluids **60**, 15 (2019).
[173]S. Chu, X. Chao, H. Wang, Y. Fan, and Y. Zhigang, "Three-dimensional spectral proper orthogonal decomposition analyses of the turbulent flow around a seal-vibrissa-shaped cylinder," Phys. Fluids **33**, 025106 (2021).
[174]W. Hanke, M. Witte, L. Miersch, M. Brede, J. Oeffner, M. Michael, F. Hanke, A. Leder, and G. Dehnhardt, "Harbor seal vibrissa morphology suppresses vortex-induced vibrations," J. Exp. Biol. **213**, 2665–2672 (2010).
[175]S. Wang and Y. Liu, "Wake dynamics behind a seal-vibrissa-shaped cylinder: A comparative study by time-resolved particle velocimetry measurements," Exp. Fluids **57**, 32 (2016).
[176]W.-L. Chen, X.-W. Min, D.-L. Gao, A.-X. Guo, and H. Li, "Experimental investigation of aerodynamic forces and flow structures of bionic cylinders based on harbor seal vibrissa," Exp. Therm. Fluid Sci. **99**, 169–180 (2018).
[177]S. Sayeed-Bin-Asad, T. S. Lundström, and A. G. Andersson, "Study the flow behind a semi-circular step cylinder (laser doppler velocimetry (LDV) and computational fluid dynamics (CFD))," Energies **10**, 332 (2017).
[178]C. Morton, "Three-dimensional wake development and structural loading on dual step cylinders in cross-flow," Ph.D. dissertation (University of Waterloo, 2014).
[179]W. Dunn and S. Tavoularis, "Experimental studies of vortices shed from cylinders with a step-change in diameter," J. Fluid Mech. **555**, 409 (2006).
[180]N. W. M. Ko and A. S. K. Chan, "In the intermixing region behind circular cylinders with stepwise change of the diameter," Exp. Fluids **9**, 213–221 (1990).
[181]C. G. Lewis and M. Gharib, "An exploration of the wake three dimensionalities caused by a local discontinuity in cylinder diameter," Phys. Fluids A **4**, 104–117 (1992).
[182]C. Morton and S. Yarusevych, "Vortex dynamics in the turbulent wake of a single step cylinder," J. Fluids Eng. **136**, 031204 (2014).
[183]C. Morton and S. Yarusevych, "Vortex shedding in the wake of a step cylinder," Phys. Fluids **22**, 083602 (2010).
[184]C. Morton and S. Yarusevych, "An experimental investigation of flow past a dual step cylinder," Exp. Fluids **52**, 69–83 (2012).
[185]C. Morton and S. Yarusevych, "On vortex shedding from low aspect ratio dual step cylinders," J. Fluids Struct. **44**, 251–269 (2014).
[186]C. Morton, S. Yarusevych, and F. Scarano, "A tomographic particle image velocimetry investigation of the flow development over dual step cylinders," Phys. Fluids **28**, 025104 (2016).
[187]C. Morton and S. Yarusevych, "Vortex shedding from cylinders with two step discontinuities in diameter," J. Fluid Mech. **902**, A29 (2020).
[188]M. C. Wolochuk, M. W. Plesniak, and J. E. Braun, "The effects of turbulence and unsteadiness on vortex shedding from sharp-edged bluff bodies," J. Fluids Eng. **118**, 18–25 (1996).
[189]D. Telionis, M. Gundappa, and T. Diller, "On the organization of flow and heat transfer in the near wake of a circular cylinder in steady and pulsed flow," J. Fluids Eng. **114**, 348–355 (1992).
[190]C. Barbi, D. P. Favier, C. A. Maresca, and D. P. Telionis, "Vortex shedding and lock-on of a circular cylinder in oscillatory flow," J. Fluid Mech. **170**, 527–544 (1986).
[191]K. Al-Asmi and I. P. Castro, "Vortex shedding in oscillatory flow: Geometrical effects," Flow Meas. Instrum. **3**, 187–202 (1992).
[192]B. J. Armstrong, F. H. Barnes, and I. Grant, "The effect of a perturbation on the flow over a bluff cylinder," Phys. Fluids **29**, 2095–2102 (1986).
[193]C. C. Hu, J. J. Miau, and J. H. Chou, "Instantaneous vortex-shedding behaviour in periodically varying flow," Proc. R. Soc. Ser. A **458**, 911–932 (2002).
[194]E. Konstantinidis, S. Balabani, and M. Yianneskis, "The effect of flow perturbations on the near wake characteristics of a circular cylinder," J. Fluids Struct. **18**, 367–386 (2003).
[195]E. Konstantinidis, S. Balabani, and M. Yianneskis, "The timing of vortex shedding in a cylinder wake imposed by periodic inflow perturbations," J. Fluid Mech. **543**, 45–55 (2005).
[196]E. Konstantinidis and S. Balabani, "Symmetric vortex shedding in the near wake of a circular cylinder due to streamwise perturbations," J. Fluids Struct. **23**, 1047–1063 (2007).
[197]E. Konstantinidis, S. Balabani, and M. Yianneskis, "Bimodal vortex shedding in a perturbed cylinder wake," Phys. Fluids **19**, 011701 (2007).
[198]E. Konstantinidis and S. Balabani, "Flow structure in the locked-on wake of a circular cylinder in pulsating flow: Effect of forcing amplitude," Int. J. Heat Fluid Flow **29**, 1567–1576 (2008).
[199]A. Jarża and M. Podolski, "Turbulence structure in the vortex formation region behind a circular cylinder in lock-on conditions," Eur. J. Mech. B **23**, 535–550 (2004).
[200]W. Kim, J. Sung, J. Y. Yoo, and M. H. Lee, "High-definition PIV analysis on vortex shedding in the cylinder wake," J. Visualization **7**, 17–24 (2004).
[201]N. I. Mikheev, V. M. Molochnikov, A. N. Mikheev, and O. A. Dushina, "Hydrodynamics and heat transfer of pulsating flow around a cylinder," Int. J. Heat Mass Transfer **109**, 254–265 (2017).
[202]M. Li, Q. Li, and H. Shi, "Aerodynamic pressures on a 5:1 rectangular cylinder in sinusoidal streamwise oscillatory flows with non-zero mean velocities," J. Wind Eng. Ind. Aerodyn. **208**, 104440 (2021).
[203]B. Wu, S. Li, L. Zhang, and K. Li, "Experimental determination of the two-dimensional aerodynamic admittances of a 5:1 rectangular cylinder in streamwise sinusoidal flows," J. Wind Eng. Ind. Aerodyn. **210**, 104525 (2021).
[204]S. Taneda and H. Honji, "Unsteady flow past a flat plate normal to the direction of motion," J. Phys. Soc. Jpn. **30**, 262–272 (1971).
[205]T. Sarpkaya and C. J. Ihrig, "Impulsively started steady flow about rectangular prisms: Experiments and discrete vortex analysis," J. Fluids Eng. **108**, 47–54 (1986).
[206]F. T. Lombardo, "Engineering analysis of a full-scale high-resolution tornado wind speed record," J. Struct. Eng. **144**, 04017212 (2018).
[207]T. Lee and R. Budwig, "The onset and development of circular-cylinder vortex wakes in uniformly accelerating flows," J. Fluid Mech. **232**, 611–627 (1991).
[208]T. Sarpkaya, "Nonimpulsively started steady flow about a circular cylinder," AIAA J. **29**, 1283–1289 (1991).
[209]R. Bouard and M. Coutanceau, "The early stage of development of the wake behind an impulsively started cylinder for $40 < \mathrm{Re} < 10{,}000$," J. Fluid Mech. **101**, 583–607 (1980).
[210]C. C. Chu and Y. Y. Liao, "A quantitative study of the flow around an impulsively started circular cylinder," Exp. Fluids **13**, 137–146 (1992).
[211]C. Lin, S.-C. Hsieh, W.-J. Lin, and R. V. Raikar, "Characteristics of recirculation zone structure behind an impulsively started circular cylinder," J. Eng. Mech. **138**, 184–198 (2012).
[212]F. Finaish, "On vortex structures and processes over bluff bodies in impulsive flow," Exp. Fluids **11**, 262–267 (1991).
[213]N. Tonui and D. Sumner, "Flow around impulsively started square prisms," J. Fluids Struct. **27**, 62–75 (2011).
[214]M. Tatsuno and S. Taneda, "Visualization of the unsteady flow past cylinders and plates decelerated from steady speed," J. Phys. Soc. Jpn. **31**, 1266–1274 (1971).
[215]Y. Lee, J. Rho, K. H. Kim, and D.-H. Lee, "Fundamental studies on free stream acceleration effect on drag force in bluff bodies," J. Mech. Sci. Technol. **25**, 695–701 (2011).
[216]T. Yang and M. S. Mason, "Aerodynamic characteristics of rectangular cylinders in steady and accelerating wind flow," J. Fluids Struct. **90**, 246–262 (2019).
[217]C. L. Ford and P. M. Winroth, "On the scaling and topology of confined bluff-body flows," J. Fluid Mech. **876**, 1018–1040 (2019).
[218]B. F. Feshalami, M. H. Djavareshkian, M. Yousefi, A. H. Zaree, and A. A. Mehraban, "Experimental investigation of flapping mechanism of the black-headed gull in forward flight," Proc. Inst. Mech. Eng. Part G **233**, 4333–4349 (2019).
[219]M. Bishop and S. Yarusevych, "Mitigating blockage effects on flow over a circular cylinder in an adaptive-wall wind tunnel," J. Fluids Eng. **133**, 081101 (2011).
[220]I. Ross and A. Altman, "Wind tunnel blockage corrections: Review and application to Savonius vertical-axis wind turbines," J. Wind Eng. Ind. Aerodyn. **99**, 523–538 (2011).
[221]F. Rehimi and F. Aloui, "Synchronized analysis of an unsteady laminar flow downstream of a circular cylinder centred between two parallel walls using PIV and mass transfer probes," Exp. Fluids **51**, 1–22 (2011).

[222]I. Guillén, C. Treviño, and L. Martínez-Suástegui, "Unsteady laminar mixed convection heat transfer from a horizontal isothermal cylinder in contra-flow: Buoyancy and wall proximity effects on the flow response and wake structure," Exp. Therm. Fluid Sci. **52**, 30–46 (2014).
[223]B. F. Feshalami and S. He, "Suppression of vortex shedding behind a square cylinder confined in a diverging channel," Ocean Eng. **235**, 109400 (2021).
[224]M. Reyes, A. Velazquez, E. Martin, and J. R. Arias, "Experimental study on the confined 3D laminar flow past a square prism with a high blockage ratio," Int. J. Heat Fluid Flow **44**, 444–457 (2013).
[225]F. Rehimi, F. Aloui, S. B. Nasrallah, L. Doubliez, and J. Legrand, "Experimental investigation of a confined flow downstream of a circular cylinder centred between two parallel walls," J. Fluids Struct. **24**, 855–882 (2008).
[226]S. Madhavan, Y. Y. Al-Jahmany, P. D. Minev, and K. Nandakumar, "On the transition to 3D modes for channel flow past a square cylinder," Can. J. Chem. Eng. **92**, 2122–2137 (2014).
[227]X. Wang, J. Chen, B. Zhou, Y. Li, and Q. Xiang, "Experimental investigation of flow past a confined bluff body: Effects of body shape, blockage ratio and Reynolds number," Ocean Eng. **220**, 108412 (2021).
[228]A. Venugopal, A. Agrawal, and S. V. Prabhu, "Vortex dynamics of a trapezoidal bluff body placed inside a circular pipe," J. Turbul. **19**, 1–24 (2018).
[229]V. Arumuru, A. Agrawal, and S. V. Prabhu, "Experimental investigations on flow over a circular cylinder placed in a circular pipe," Phys. Fluids **32**, 095122 (2020).
[230]C. Lei, L. Cheng, and K. Kavanagh, "Re-examination of the effect of a plane boundary on force and vortex shedding of a circular cylinder," J. Wind Eng. Ind. Aerodyn. **80**, 263–286 (1999).
[231]M. J. Ezadi Yazdi and A. Bak Khoshnevis, "Wake-boundary layer interaction behind an elliptic cylinder at different Reynolds numbers," J. Turbul. **19**, 529–552 (2018).
[232]S. J. Price, D. Sumner, J. G. Smith, K. Leong, and M. P. PaÏDoussis, "Flow visualization around a circular cylinder neat to a plane wall," J. Fluids Struct. **16**, 175–191 (2002).
[233]A. A. Oner, M. Salih Kirkgoz, and M. Sami Akoz, "Interaction of a current with a circular cylinder near a rigid bed," Ocean Eng. **35**, 1492–1504 (2008).
[234]I. Khabbouchi, M. S. Guellouz, and S. Ben Nasrallah, "A study of the effect of the jet-like flow on the near wake behind a circular cylinder close to a plane wall," Exp. Therm. Fluid Sci. **44**, 285–300 (2013).
[235]W.-J. Lin, C. Lin, S.-C. Hsieh, and S. Dey, "Flow characteristics around a circular cylinder placed horizontally above a plane boundary," J. Eng. Mech. **135**, 697–716 (2009).
[236]F. Yang, H. An, and L. Cheng, "Drag crisis of a circular cylinder near a plane boundary," Ocean Eng. **154**, 133–142 (2018).
[237]P. Ouro, V. Muhawenimana, and C. A. Wilson, "Asymmetric wake of a horizontal cylinder in close proximity to a solid boundary for Reynolds numbers in the subcritical turbulence regime," Phys. Rev. Fluids **4**, 104604 (2019).
[238]J. Zhou, X. Qiu, J. Li, and Y. Liu, "The gap ratio effects on vortex evolution behind a circular cylinder placed near a wall," Phys. Fluids **33**, 037112 (2021).
[239]R. J. Martinuzzi, S. C. C. Bailey, and G. A. Kopp, "Influence of wall proximity on vortex shedding from a square cylinder," Exp. Fluids **34**, 585–596 (2003).
[240]L. L. Shi, Y. Z. Liu, and H. J. Sung, "On the wake with and without vortex shedding suppression behind a two-dimensional square cylinder in proximity to a plane wall," J. Wind Eng. Ind. Aerodyn. **98**, 492–503 (2010).
[241]C. He, Y. Liu, D. Peng, and S. Yavuzkurt, "Measurement of flow structures and heat transfer behind a wall-proximity square rib using TSP, PIV and split-fiber film," Exp. Fluids **57**, 165 (2016).
[242]S. Malavasi and G. Blois, "Wall effects on the flow structure around a rectangular cylinder," Meccanica **47**, 805–815 (2012).
[243]P. K. Panigrahi, "PIV investigation of flow behind surface mounted detached square cylinder," J. Fluids Eng. **131**, 011202 (2008).
[244]F. Yang, Z. Zhou, G. Tang, and L. Lu, "Steady flow around a square cylinder near a plane boundary," Ocean Eng. **222**, 108599 (2021).
[245]A. Cigada, S. Malavasi, and M. Vanali, "Effects of an asymmetrical confined flow on a rectangular cylinder," J. Fluids Struct. **22**, 213–227 (2006).
[246]S. Malavasi and E. Zappa, "Fluid-dynamic forces and wake frequencies on a tilted rectangular cylinder near a solid wall," Meccanica **44**, 91–101 (2009).
[247]J. H. Choi and S. J. Lee, "Flow characteristics around an inclined elliptic cylinder in a turbulent boundary layer," J. Fluids Struct. **15**, 1123–1135 (2001).
[248]E. Esmaeilifar, M. Hassan Djavareshkian, B. F. Feshalami, and A. Esmaeili, "Hydrodynamic simulation of an oscillating hydrofoil near free surface in critical unsteady parameter," Ocean Eng. **141**, 227–236 (2017).
[249]D. Mouazé and M. Bélorgey, "Flow visualisation around a horizontal cylinder near a plane wall and subject to waves," Appl. Ocean Res. **25**, 195–211 (2003).
[250]P. Reichl, K. Hourigan, and M. C. Thompson, "Flow past a cylinder close to a free surface," J. Fluid Mech. **533**, 269–296 (2005).
[251]V. Venugopal, K. S. Varyani, and P. C. Westlake, "Drag and inertia coefficients for horizontally submerged rectangular cylinders in waves and currents," Proc. Inst. Mech. Eng. Part M **223**, 121–136 (2009).
[252]J. Bai, N. Ma, and X. Gu, "Study of interaction between wave-current and the horizontal cylinder located near the free surface," Appl. Ocean Res. **67**, 44–58 (2017).
[253]J. Sheridan, J. C. Lin, and D. Rockwell, "Flow past a cylinder close to a free surface," J. Fluid Mech. **330**, 1–30 (1997).
[254]H. Ren, Y. Xu, M. Zhang, S. Deng, S. Li, S. Fu, and H. Sun, "Hydrodynamic forces on a partially submerged cylinder at high Reynolds number in a steady flow," Appl. Ocean Res. **88**, 160–169 (2019).
[255]S. J. Lee, "Near-wake flow structure of elliptic cylinders close to a free surface: Effect of cylinder aspect ratio," Exp. Fluids **36**, 748–758 (2004).
[256]S. J. Lee and Daichin, "Flow past a circular cylinder over a free surface: Interaction between the near wake and the free surface deformation," J. Fluids Struct. **19**, 1049–1059 (2004).
[257]S. Malavasi and A. Guadagnini, "Interactions between a rectangular cylinder and a free-surface flow," J. Fluids Struct. **23**, 1137–1148 (2007).
[258]E.-R. Qi, G.-Y. Li, W. Li, J. Wu, and X. Zhang, "Study of vortex characteristics of the flow around a horizontal circular cylinder at various gap-ratios in the cross-flow," J. Hydrodyn. Ser B **18**, 334–340 (2006).
[259]M. Negri, F. Cozzi, and S. Malavasi, "Self-synchronized phase averaging of PIV measurements in the base region of a rectangular cylinder," Meccanica **46**, 423–435 (2011).
[260]N. F. Tumen Ozdil and H. Akilli, "Investigation of flow structure around a horizontal cylinder at different elevations in shallow water," Ocean Eng. **96**, 56–67 (2015).
[261]B. Qin, P. F. Salipante, S. D. Hudson, and P. E. Arratia, "Upstream vortex and elastic wave in the viscoelastic flow around a confined cylinder," J. Fluid Mech. **864**, R2 (2019).
[262]P. M. Coelho and F. T. Pinho, "Vortex shedding in cylinder flow of shear-thinning fluids: I. Identification and demarcation of flow regimes," J. Non-Newtonian Fluid Mech. **110**, 143–176 (2003).
[263]D. F. James, T. Shiau, and P. M. Aldridge, "Flow of a Boger fluid around an isolated cylinder," J. Rheol. **60**, 1137–1149 (2016).
[264]V. M. Ribeiro, P. M. Coelho, F. T. Pinho, and M. A. Alves, "Viscoelastic fluid flow past a confined cylinder: Three-dimensional effects and stability," Chem. Eng. Sci. **111**, 364–380 (2014).
[265]C. Bergins, M. Nowak, and M. Urban, "The flow of a dilute cationic surfactant solution past a circular cylinder," Exp. Fluids **30**, 410–417 (2001).
[266]O. Cadot, "Partial roll-up of a viscoelastic Kármán street," Eur. J. Mech. B **20**, 145–153 (2001).
[267]J. R. Cressman, Q. Bailey, and W. I. Goldburg, "Modification of a vortex street by a polymer additive," Phys. Fluids **13**, 867–871 (2001).
[268]P. M. Coelho and F. T. Pinho, "Vortex shedding in cylinder flow of shear-thinning fluids: II. Flow characteristics," J. Non-Newtonian Fluid Mech. **110**, 177–193 (2003).
[269]P. M. Coelho and F. T. Pinho, "Vortex shedding in cylinder flow of shear-thinning fluids. III: Pressure measurements," J. Non-Newtonian Fluid Mech. **121**, 55–68 (2004).
[270]C. J. Pipe and P. A. Monkewtiz, "Vortex shedding in flows of dilute polymer solutions," J. Non-Newtonian Fluid Mech. **139**, 54–67 (2006).